

A UNIFIED INTERPRETATION OF
NONLINEAR ELASTICITY IN
GRANULAR SOLIDS

by
Xun Li

© Copyright by Xun Li, 2018

All Rights Reserved

A thesis submitted to the Faculty and the Board of Trustees of the Colorado School of Mines in partial fulfillment of the requirements for the degree of Master of Science (Geophysics).

Golden, Colorado

Date _____

Signed: _____

Xun Li

Signed: _____

Dr. Roel Snieder
Thesis Advisor

Golden, Colorado

Date _____

Signed: _____

Dr. John Bradford
Professor and Head
Department of Geophysics

ABSTRACT

Granular solids such as natural rocks and concrete show nonlinear elasticity in response to dynamic deformation with a large strain amplitude. Resonance experiments can measure the nonlinear elasticity using resonance curves which show response amplitudes as a function of driving (oscillation) frequencies. To analyze the nonlinear elasticity observed in resonance experiments, I first simulate a nonlinear oscillation system (i.e., Duffing equation) that involves a cubic term in the equation of state. The simulation illustrates three critical factors, i.e., driving frequency, driving amplitude, and the initial condition of the deformation; these factors control the stable solution that is the sustained amplitude of the Duffing oscillation.

I propose a thermodynamics-based model to reproduce the nonlinear resonance features observed in laboratory experiments of rocks and concrete including (a) the log-time recovery of the resonant frequency after the deformation ends (slow dynamics), (b) asymmetric resonance curves in the direction of the driving frequency, (c) the difference between resonance curves when the driving frequency is swept upward and downward, and (d) the presence of a “cliff” segment to the left of the resonant peak under the condition that the nonlinearity in the oscillation system is strong. This model provides a unified interpretation of nonlinear elasticity. The asymmetry of the resonance curve is caused by softening, which is documented by a reduction of the resonant frequency during the deformation; the cliff segment of the resonance curve is linked to a bifurcation that involves a steep change in the response amplitude when the driving frequency is changed.

The simulated Duffing oscillation system shows similar behavior as the resonance simulations. The bifurcation originates from the strong nonlinearity in the oscillation system and is present in both simulations. Extensions of the thermodynamics-based model could include temperature, moisture (pore pressure), and confining pressure. This thesis could contribute to geophysical applications such as monitoring of fracture healing after hydraulic fracturing

in unconventional oil and gas reservoirs as well as in enhanced geothermal systems.

TABLE OF CONTENTS

ABSTRACT	iii
LIST OF FIGURES	vii
LIST OF TABLES	x
LIST OF ABBREVIATIONS	xi
ACKNOWLEDGMENTS	xii
DEDICATION	xiv
CHAPTER 1 INTRODUCTION	1
1.1 Laboratory measurements	3
1.2 Nonlinear features	6
1.3 Field observations	13
CHAPTER 2 NONLINEAR OSCILLATORS	17
2.1 Numerical solution	21
CHAPTER 3 NONLINEAR ELASTICITY IN RESONANCE EXPERIMENTS	31
3.1 Introduction	32
3.2 Model	33
3.2.1 Feedback cycle	34
3.2.2 Thermodynamics-based parametrization	35
3.3 Resonance simulation	40
3.4 Numerical simulations	40
3.4.1 Recovery of resonant frequency	40

3.4.2	Asymmetric resonance curves	42
3.4.3	Up-down difference and slow dynamics	46
3.4.4	Cliff in resonance curves	46
3.5	Discussion	52
3.6	Conclusion	53
3.7	Acknowledgments	54
CHAPTER 4	OUTLOOK	55
4.1	Limitations	55
4.2	Future work in geophysics	58
REFERENCES CITED	62
APPENDIX A	MEASUREMENT PROTOCOL	77
APPENDIX B	STEADY STATE SOLUTION	79
APPENDIX C	PERMISSION OF COPYRIGHT	81
C.1	Permission of accepted paper	81
C.2	Permission from coauthor	81
C.3	Permission of reused graphs	81

LIST OF FIGURES

Figure 1.1	Experimental setup of DAET (adapted from Renaud et al.).	5
Figure 1.2	Variation of the resonant frequency with multiple relaxations and excitations (conditioning). The graph is adapted from TenCate.	8
Figure 1.3	Slow dynamics with the log-time recovery of the resonant frequencies for four geomaterials. The graph is adapted from TenCate.	9
Figure 1.4	(a) One cycle of the variable stress field with amplitudes $A_2 > A_1$. (b) Stress-strain curves for two different amplitudes of the stress field. These stress-strain curves form loops with average modulus K_1 and K_1 ; the shaded area denotes the energy dissipated during the loading (A_1). The graph is adapted from Meo et al.	11
Figure 1.5	Variation of the elastic modulus of the Berea sandstone during a cycle of the stress field. The graph is adapted from Renaud et al.	11
Figure 1.6	Eight-year variation of the seismic velocity in northern Chile in response to multiple ground shaking events. (a) Variation of the seismic velocity and the correlation coefficients denoted by the color bar. (b) Absolute ground acceleration recorded at a station. The graph is adapted from Gassenmeier et al., and one can find more details therein.	14
Figure 2.1	Numerical solution of the Duffing equation for the temporal variation of the strain x in response to the driving field $F_d(t)$. (a) The appearance of the curve as a thick line results from the high-frequency fluctuation that is not resolved in the graph. (b) A zoom-in of the high-frequency oscillation.	22
Figure 2.2	Duffing resonance curve obtained from the solutions of the Duffing equation. The graph shows the solutions of stable amplitudes for different driving frequencies. The driving amplitude is $A_r = 13.2/s^2$ and the anharmonic coefficient is $\delta = -9 \times 10^{17}$	23
Figure 2.3	Duffing resonance curve with the driving amplitude $A_r = 35.2/s^2$	24
Figure 2.4	Duffing resonance curve with the anharmonic coefficient $\delta = -15 \times 10^{17}$	25

Figure 2.5	Numerical solutions of the Duffing equation for the temporal variations of the strain x with different initial conditions: (a) initial strain $x(0) = 0$ and (b) $x(0) = 4 \times 10^{-6}$. The driving frequency is $f_d = 3850$ Hz and the driving amplitude is $A_r = 35.2/s^2$	26
Figure 2.6	Duffing resonance curves with two initial conditions, i.e., (a) initial strain $x(0) = 0$ and (b) $x(0) = 4 \times 10^{-6}$. The driving amplitude is $A_r = 35.2/s^2$	27
Figure 2.7	Duffing resonance curves with two initial conditions, i.e., (a) initial strain $x(0) = 0$ and (b) $x(0) = 4 \times 10^{-6}$. The driving amplitude is $A_r = 13.2/s^2$	28
Figure 2.8	Schematic graph of the bifurcation.	29
Figure 3.1	Feedback cycle for nonlinear material properties.	34
Figure 3.2	bistable energy model for a fracture. For a barrier energy E_b , τ_c and τ_o indicate the transition times to open and close the fracture, respectively. .	35
Figure 3.3	Energy levels of open and closed fractures as a function of the dynamic normal strain. Positive strain corresponds to extension, and negative strain corresponds to compression.	37
Figure 3.4	Recovery of the resonant frequency after dynamic deformations with different strain amplitudes, where $t_0 = 5 \mu s$ is time step in the numerical model. The vertical dashed line denotes τ_{max}	41
Figure 3.5	Recovery of the resonant frequency for a single barrier energy.	42
Figure 3.6	Resonance curves for the upward (solid lines) and downward (dashed lines) sweeps with different driving amplitudes $A_r = 8.8, 13.2, 17.6/s^2$. . .	44
Figure 3.7	Resonance curves as in Figure 3.6, but for a single barrier energy.	45
Figure 3.8	Sweep-rate dependence of the up-down difference of the resonance curves at the left side of the resonant peak. Solid lines denote the upward sweep, while dashed lines denote the downward sweep. The sweep time interval between sampled driving frequencies is (a) 5 ms ($0.01\tau_{max}$), (b) 500 ms (τ_{max}), and (c) 5 s ($10\tau_{max}$).	47

Figure 3.9	Sweep rate dependence of the up-down difference. The fracture modulus is $C_0 = 3.088$ GPa, with stronger nonlinearity than that in Figure 3.8. The sweep-time interval between sampled driving frequencies is (a) 5 ms ($0.01\tau_{max}$), (b) 500 ms (τ_{max}), and (c) 5 s ($10\tau_{max}$), following Figure 3.8.	48
Figure 3.10	Steady-state solution of our model with (a) $A_r = 0.6/s^2$ and (b) $A_r = 1.0/s^2$. The color scale indicates for each frequency and original value N_{oi} the equilibrium fraction N_o to which the solution converges. . .	50
Figure 3.11	Solution of the thermodynamics-based oscillation model with (a) $C_0 = 1.853$ GPa and (b) $C_0 = 3.088$ GPa. The color scale indicates for each frequency and original value N_{oi} the equilibrium fraction N_o to which the true solution converges.	51
Figure 4.1	Resonance curves for upward and downward sweeps for partially saturated chalk. The inset shows a low-drive resonance curve where unusual instability does not exist. The graph is adapted from Johnson et al.	59
Figure A.1	Time line of the measurement protocol.	78
Figure C.1	Copyright permission of reusing my accepted paper into the thesis (https://journals.aps.org/copyrightFAQ.html).	81
Figure C.2	Copyright permission from the coauthor of Chapter 3.	82
Figure C.3	Copyright permission of reusing graphs in Renaud et al.	83
Figure C.4	Copyright permission of reusing graphs in Gassenmeier et al.	84
Figure C.5	Copyright permission of reusing graphs in TenCate.	85
Figure C.6	Copyright permission of reusing graphs in Meo et al.	86
Figure C.7	Copyright permission of reusing graphs in Johnson et al.	87

LIST OF TABLES

Table 2.1	Numerical values of the parameters used in equation 2.11.	22
Table 3.1	Numerical values of the parameters used.	39

LIST OF ABBREVIATIONS

equation of state	EOS
nonlinear mesoscopic elasticity	NME
nonlinear resonant ultrasound spectroscopy	NRUS
dynamic acoustoelastic testing	DAET
Preisach-Mayergoyz	PM

ACKNOWLEDGMENTS

I would like to thank Dr. Roel Snieder particularly. He is a great advisor as well as a mentor who takes care of his students in every aspect. He teaches students professional skills with incredible patience and enthusiasm. His passion for education and research passes on to me, and I am motivated to be a researcher in the future. Also, he is never blind to students' personal life. He is a fearless leader in my research and our weekly running group. The most valuable skill I learned from him is the way to inspire myself in both life and research. These research and life skills I learned from him are invaluable for my future life and career.

As far as I am aware, “research life” is an integrated concept including research and life. I came to the graduate study without knowing anything about the graduate life, which turned out to be quite different from my undergraduate. I had to find a balance between the research and coursework, and I learned to balance my personal and research life. Regarding my thesis research, nonlinear rock physics, I thank Dr. Christoph Sens-Schönfelder at GFZ German research center for Geosciences, Potsdam. He inspired me in implementing novel simulations and working on the theory of nonlinear elasticity, and the work finally forms this thesis. I thank my thesis committee members, Dr. Hossein Kazemi, Dr. Ali Tura, and Dr. Ilya Tsvankin who discussed the research with me. Without these people, this thesis would not be possible.

I perfectly understand that research life will never be easy. I was inspired to be a researcher when I did my undergraduate research projects with Dr. Ian Main and Dr. Andrew Curtis at the University of Edinburgh. The challenges in the research motivated me to take an adventure into graduate study. I appreciate my experience in working with them as an undergraduate researcher since this work opened the door for me into graduate school.

Finally, I thank Diane Witters who helped me with professional writing. I thank Dawn Umpleby, Michelle Szobody, and Joana Perez who helped me at the Center for Wave Phe-

nomena (CWP) and the Department of Geophysics. Many thanks to my CWP colleagues, Ivan Lim Chen Ning, Tong Bai, Qifan Liu, Aaron Prunty, Alex Jia, Thomas Rapstine, Alicia Arias, Iga Pawelec, and Colton Kohnke who accompanied me for two years in the research and life. I thank the sponsors of the Center for Wave Phenomena, whose support made my research at Colorado School of Mines possible.

To my Mom and Dad

CHAPTER 1

INTRODUCTION

Hooke's law involves a linear relationship between strain and loading stress when the strain is below the linear elastic threshold [6]. Continuum mechanics regards Hooke's law as a first-order linear approximation of the stress as a function of the strain [7]; the corresponding first-order coefficient, expressed as the ratio of the stress to the strain, is referred to as the elastic modulus, which represents the rigidity or incompressibility of a material. Dynamic deformation propagates in solids and forms elastic waves traveling with a wavespeed that depends on the elastic moduli. When the deformation follows the Hooke's law as the equation of state (EOS) or constitutive equation, linear elastic waves can describe the propagation of mechanical energy in solids; this linearity requires that the amplitude of the dynamic deformation does not exceed the linear elastic threshold [8]. Both exploration and global seismology typically use the linear EOS to account for wave propagation in the Earth [9], but some work [e.g., 10] also involves nonlinear phenomena in wave propagation.

Linear elastic materials have a frequency response that is independent of the deformation amplitude. In other words, two waves can linearly superimpose without distorting each other when the waves come together. Studies [e.g., 11, 12] of wave theory often apply the linear EOS in the equation of motion that physically describes elastic wave propagation in linear elastic materials.

Granular solids display nonlinear elasticity with a deformation strain as low as 10^{-7} [13]. I refer to granular solids as a general term including natural rocks, concrete, and damaged solid materials. Together with Newton's law, a nonlinear EOS governs the equation for "nonlinear wave propagation" that refers to mechanical waves propagating in nonlinear elastic media with a large wave amplitude [14]. Since the EOS involves a nonlinear relationship between stress and strain, wave propagation shows a variety of nonlinear features such as stress-strain

curves with a hysteretic area caused by both attenuation and nonlinearity [6, 15], resonance curves with a shift in resonant frequency [5, 16, 17], nonlinear dissipation [18], and nonlinear attenuation [19].

Nonlinear elasticity can be categorized based on the physical origins of nonlinearity. Solid materials have the classical atomic nonlinear elasticity that originates from atomic and molecular lattice anharmonicity (Landau's theory); as a result, stress is a function of strain with higher order terms in addition to the first order coefficient [20]. The classical nonlinear elasticity applies to solid materials when the strain is large; this type of nonlinear elasticity is commonly weak due to strong intermolecular forces among molecules that compose a solid. When the strain exceeds the elastic threshold, materials are broken with irreversible permanent deformation [6].

Granular solids such as rocks intrinsically have another type of nonlinear elasticity that originates from defects [14]. Natural rocks contain defects such as contacts between soft composites and a hard matrix [21]; for example in sandstones, quartz acts as the hard crystal element, and intergranular clay acts as the soft matrix element. Other defects in rocks include lattice imperfections, bonds, and intergranular contacts. This thesis uses the word "fractures" as a general term for all of these types of defects in granular solids including natural rocks and concrete. Since the size of these defects is commonly at the nanoscale, one refers to this elasticity as nonlinear mesoscopic elasticity (NME) [22]. Although the size of natural fractures ranges from the nanoscale to millimeters, and even larger in the field scale, a fracture at the macroscale (e.g., millimeters) could be regarded as a combination of a massive number of mesoscopic elements such as nanoscale intergranular contacts and bonds. The NME can be strong when a large mesoscopic fracture density exists in a solid. These mesoscopic fractures including granular contacts and bonds are of much smaller sizes compared to the macroscopically observable fracture sets [23]. Since fractures dominate the NME, one can apply nonlinear elasticity to the damage assessment of building materials (e.g., concrete) [24–27]. The construction industry assesses the quality of cemented concrete

using nondestructive testing that measures the nonlinear elasticity of concrete [28].

This thesis provides insights into the nonlinear elasticity observed in granular solids. I first introduce measurement techniques that quantitatively assess the nonlinear elasticity (section 1.1). Section 1.2 introduces various observed nonlinear features in laboratory measurements and the existing theoretical models, which aim to explain these features. Section 1.3 shows the field-observed nonlinear features during strong ground shaking. Among the various features observed in the laboratory and field, my thesis focuses on the simulation of resonance experiments and reproduces the observed nonlinear features in resonance curves. Chapter 2 introduces several nonlinear oscillators that are mathematical descriptions of resonance experiments. Section 2.1 illustrates three important factors that control the nonlinear oscillation system. Chapter 3 contains a thermodynamics-based model that qualitatively simulates the observed nonlinear features in resonance curves; the simulation provides a unified interpretation of the nonlinear elasticity observed in resonance experiments. The thesis concludes with the limitations of the thermodynamics-based model and an outlook related to laboratory and field measurements (Chapter 4).

1.1 Laboratory measurements

A variety of laboratory techniques have been carried out to measure the nonlinear elasticity of granular solids such as rocks and concrete. Typical laboratory experiments involve resonating a cylindrical solid sample (e.g., rocks) with a large deformation amplitude; strong deformation further induces the nonlinearity of the dynamically deformed sample. Different measurement techniques apply different methods to monitoring the variation of the elastic modulus (seismic velocity) of the sample.

Nonlinear resonant ultrasound spectroscopy (NRUS) involves the measurement of the resonant frequency with a periodic stress field loaded along the central axis of a cylindrical sample. A vibrator loads one end of the sample and emits low-frequency, high-amplitude pump waves that condition the sample into a new elastic state [5, 29, 30]. Pump waves give a strong dynamic stress field that continuously shakes the sample, and “condition”

refers to changing the elastic state (modulus) of a sample using dynamic deformation with a large strain amplitude [31]. In response to the pump waves, the sample oscillates and gradually reaches a steady state with a sustained oscillation amplitude. NRUS measures stable oscillation amplitudes against different driving frequencies used in the stress field; the driving frequency can be either continuously swept from a lower to a higher value (upward) or from a higher to a lower value (downward). When the driving frequency approaches the resonant frequency of the sample, response amplitude increases significantly and reaches a peak that is called the resonant peak and indicates the resonant frequency. The change of resonant frequency with dynamic deformation indicates the change of seismic velocity; the resonant frequency often shifts towards a lower value in response to dynamic deformation, and hence the sample softens, and the wave velocity is reduced. Thus, the resonant frequency shift reveals the nonlinear elasticity of the sample. Torsional shear stress field can also excite pump waves, which change the shear rigidity of a sample [32, 33]. Chapter 3 gives more details of NRUS.

Dynamic acoustoelastic testing (DAET) is used to measure the variation of the seismic velocity when a sample is conditioned by pump waves. Apart from low-frequency pump waves, the experiment includes high-frequency probe waves orthogonal to the low-frequency pump waves, as shown in Figure 1.1. The probe waves travel between the two ultrasound transducers with a small wave amplitude, which avoids inducing nonlinearity in the sample. Since probe waves are too weak to generate nonlinearity in the sample, the change of the probe-wave traveltimes determines the variation of the seismic velocity; such a variation reflects the nonlinearity induced by the pump waves. The probe waves have much higher frequency than the pump waves; hence, probe waves can be launched successively with a short time interval. A series of probe signals can cross-correlate with the reference signal that is recorded when pump waves are not present; the crosscorrelations give the shifts of the transmitted P phase (first arrival) and further give the relative velocity deviations $\Delta c/c_0$ from a static unstrained sample with seismic velocity c_0 [30, 34–37]. In other words, one

can monitor the variation of the seismic velocity during dynamic deformation. Apart from concrete [25, 38] and rocks [39], DEAT also applies to assessing the damage in artificially kinked nonlinear materials [40].

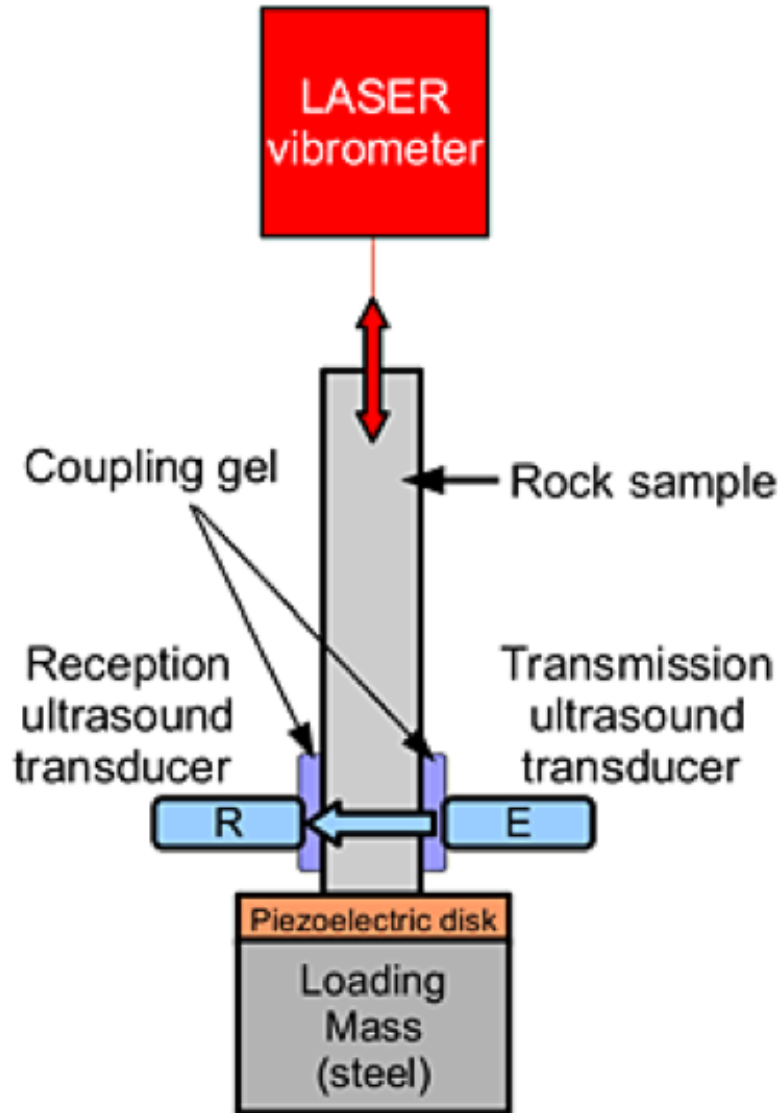


Figure 1.1: Experimental setup of DAET (adapted from Renaud et al. [1]).

Other techniques exist with a similar experimental setup to DAET. Gallot et al. [41] measure the change of the P-wave arrival time due to S pump waves. Diffuse acoustic wave spectroscopy [42] incorporates coda wave interferometry [43–47] to measure the shift of the coda of probe signals; this calculation enhances the measurement accuracy of velocity vari-

ations during dynamic deformation. Diffuse acoustic wave spectroscopy works best when a sample is strongly inhomogeneous, and the wave propagation inside the sample has strong multiple scattering [48]. In addition, the coda mainly contains S-wave energy that is more sensitive to fractures in the sample than P waves (e.g., first arrival) [49, 50]. Laser interferometry performs a role in nondestructive testing without using contacting sensors [51]; the probe signals can be recorded by a laser sensor pointed at the surface of the sample. Lobkis and Weaver [52] use a resonance technique (i.e., Larsen effect) that applies an ultrasonic feedback circuit ring to monitoring the curing process of a cement paste sample after a wooden ball drops onto the sample and causes a transient impact.

1.2 Nonlinear features

Dynamic deformation driven by pump waves show more nonlinear elastic features in granular solids than static stress loading experiments [6]. Granular solids soften in response to tension and harden in response to compression; this asymmetric response originates from the Hertzian law that gives the EOS of intergranular contacts [20, 21]. The elasticity of these contacts follows a nonlinear stress-strain (σ - ϵ) relationship, $\sigma \propto \epsilon^{3/2}$ in compression; tension detaches the contacts and results in zero contact stress.

NRUS can be used to measure the resonant frequency shift in response to dynamic deformation; the shift is commonly negative, indicating softening of a sample during the dynamic deformation. The measured resonant frequency shift is proportional to the change of Young's modulus when the shift is small compared to the static resonant frequency [5]. The measured resonant frequency shifts against deformation amplitudes can be indicative of the parameters in a nonlinear EOS [29] that includes higher order anharmonicities and a hysteretic term (i.e., Hertzian factor) regarding the asymmetric response to tension and compression (see Chapter 2 for more details). Johnson et al. [53] measure a nonlinear parameter that is the third order coefficient of a nonlinear EOS using resonant frequency shifts against deformation amplitudes. In addition, the scaling subtraction method can measure other anharmonic coefficients as well as the Hertzian factor [54]. The nonlinear elasticity of

a granular sample becomes significant when the amplitude of the pump waves is beyond a strain threshold ϵ_M ; this threshold divides the deformation into two regimes [55, 56]. When the deformation amplitude is below ϵ_M , the resonant frequency shift (nonlinearity) is small and can be adequately described by the classical atomic nonlinear elasticity (i.e., Landau’s theory) [20]. When the amplitude is beyond ϵ_M , the resonant frequency shifts significantly to a lower value with an increase in amplitude; nonclassical nonlinear elasticity explains this correlation between the deformation amplitude and resonant frequency shift [13, 57].

NRUS reveals the correlation between the microdamage density and nonlinear elasticity (softening) in a sample; a higher degree of damage in the sample causes a larger shift of the resonant frequency, indicating stronger softening [58]. Thus, the damage assessments using NRUS have been applied to concrete for building construction [24, 27, 31] and to human bones for medical diagnostics [26] where nonlinear acoustic imaging can be competitive to CT scan imaging.

NRUS produces resonance curves where nonlinear elasticity leads to (a) steepening of the curves at the left of the resonant peak and flattening at the right of the peak and (b) the difference of the curves when sweeping the driving frequency upward and downward. Chapter 3 gives more details of these features.

Granular solids show anelasticity, i.e., a type of nonlinear elasticity that evolves with time. During dynamic deformation, a sample commonly softens (with some exception described in ref. [59]); after the deformation ends, the sample gradually recovers to the original elastic state (modulus), as shown in Figure 1.2 where the decrease in the resonant frequency indicates the softening, and the increase indicates the recovery. The recovery curve is linear with the logarithm of time [2, 42, 52, 60–62], as shown in Figure 1.3. One refers to this log-time recovery as *slow dynamics*. NRUS can be used to measure slow dynamics; the experiment requires a weak driving stress field to avoid inducing nonlinearity in a cylindrical sample during recovery; the weak stress field acts as the probe waves propagating along the central axis of the bar (sample). These probe waves involve a fast frequency sweep for the

instantaneous resonant frequency of the sample. Hence, one can record the time-varying resonant frequency in the recovery process [63]. In addition, DAET can be used to measure slow dynamics; the experiment maintains probe waves after pump waves stop. DAET can also be used to measure fast dynamics that refers to the reduction of seismic velocity when conditioning a sample using the dynamic deformation that is driven by the pump waves. Also, coda wave interferometry can be used to measure the variation of the seismic velocity during and after dynamic deformation [42, 43].

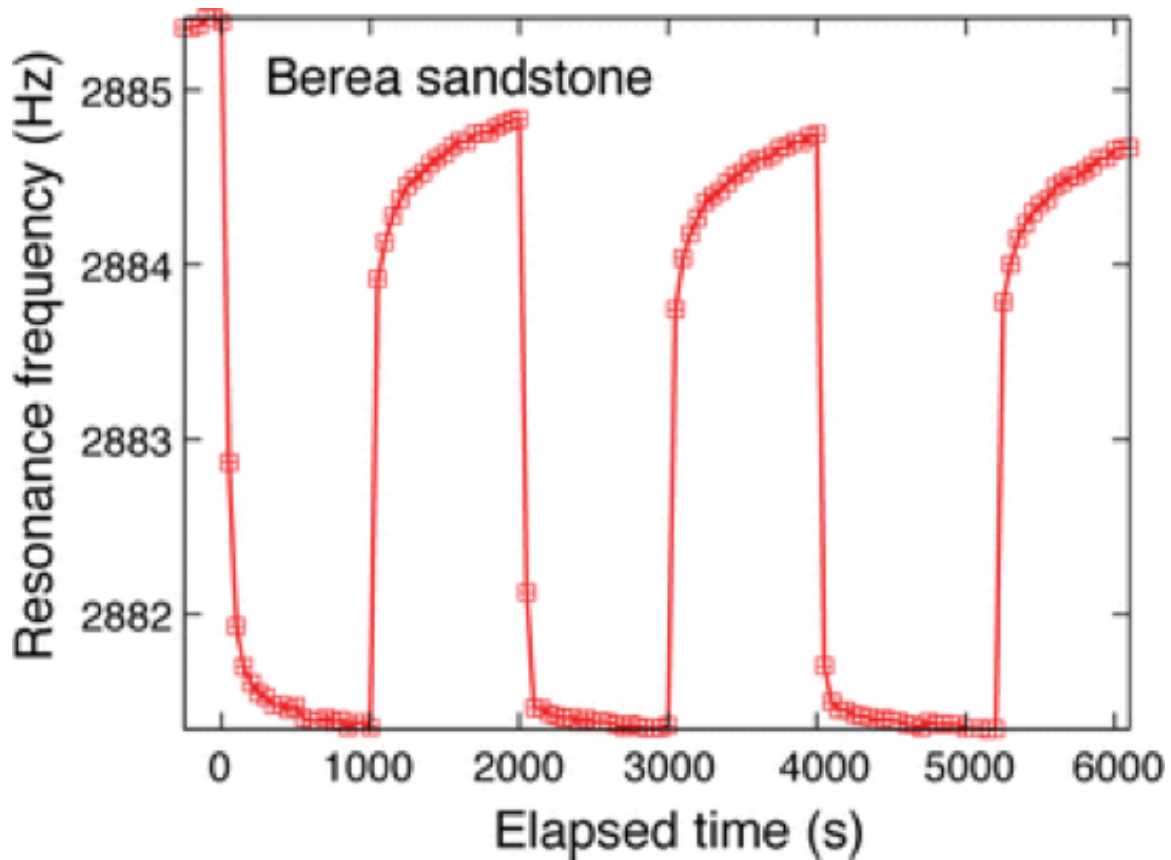


Figure 1.2: Variation of the resonant frequency with multiple relaxations and excitations (conditioning). The graph is adapted from TenCate [2].

Anelasticity causes hysteresis that reflects the signature of the memory of the past deformation. One can dynamically load a sample with a stress field and measure the instantaneous response amplitude. The stress-strain curve features a hysteresis loop that involves different curves (paths) depending on whether the strain is increasing or decreasing [3, 64]. Different

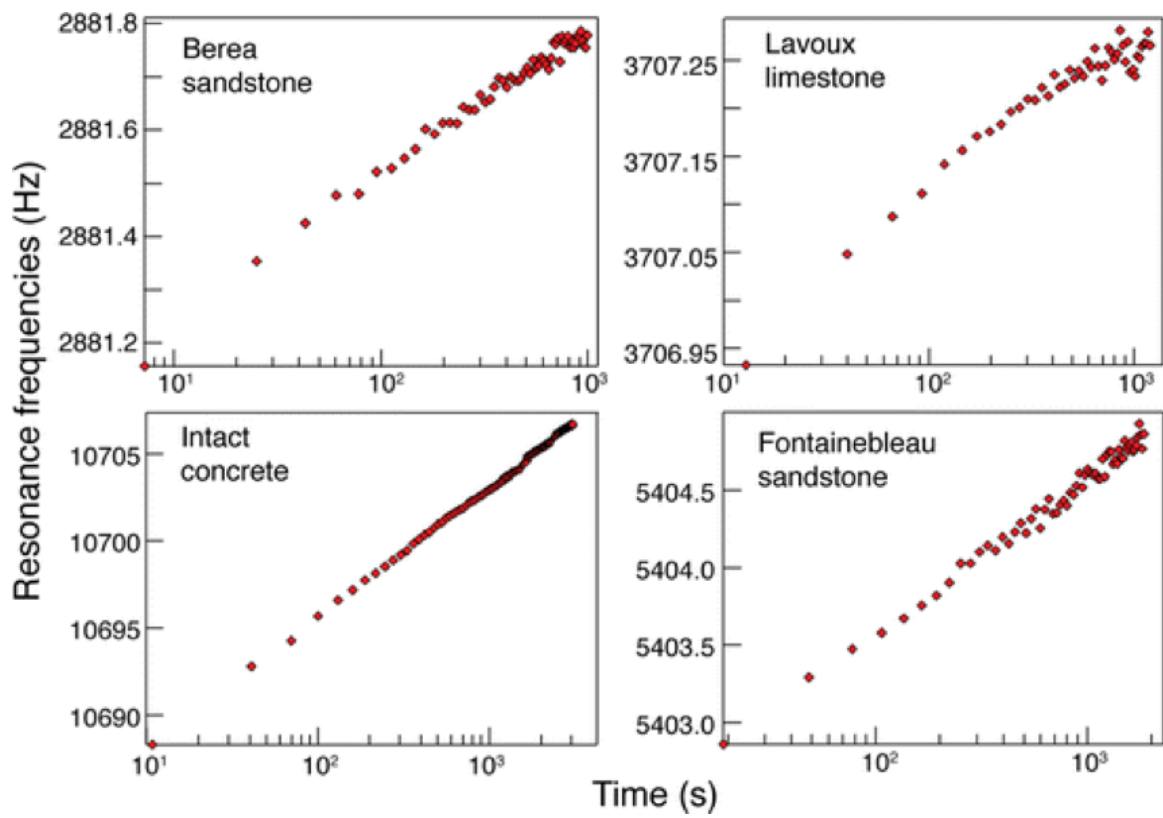


Figure 1.3: Slow dynamics with the log-time recovery of the resonant frequencies for four geomaterials. The graph is adapted from TenCate [2].

paths exist for the stress-strain curve when the loading moves from tension to compression and from compression to tension [32]. In this case, the sign of the strain rate $\dot{\epsilon}$ affects the instantaneous elasticity [40]. A linear visco-elastic material shows hysteresis that is caused by damping and attenuation [65, 66], as shown in Figure 1.4. Also, nonlinear elastic materials such as granular solids show hysteresis that is caused by both the attenuation and nonlinearity regarding a nonlinear relationship between the stress and strain [13, 15, 21, 59]. The hysteresis in granular solids shows complicated behavior such as various shapes of hysteresis loops [e.g., 67, 68]. DAET is used to measure hysteresis in granular solids including rocks and concrete; the experiment gives a hysteresis loop where the change of the elastic modulus is recorded against the oscillating deformation strain, as shown in Figure 1.5. The elasticity-strain curve shows complicated behavior [1, 30]; for example, the loop in the bottom-left of Figure 1.5 displays a shape of “triple butterfly”. Rivière et al. [69] show that these hysteresis loops could vanish when the stress field varies slowly. Also, Holcomb [6] points out that at slow stress sweep rates, the hysteretic area of stress-strain curves decreases to zero. This disappearance of hysteresis with slow-varying stress is reminiscent of slow dynamics, where the effect of the past deformation on the present elastic state dissipates with time (memory effect). Rivière et al. [30] classify rock types based on the observed nonlinear features in NRUS and DAET.

For wave propagation in nonlinear elastic materials, wave modulation experiments show that two collinear single-frequency continuous waves (one of higher frequency f_1 and one of lower frequency f_2) generate side-band frequency components (i.e., combination frequency $f_1 \pm f_2$) in addition to harmonics [14, 70]. This generation of combination frequency is well-known as the Luxemburgh-Gorky effect observed in granular solids or a granular packing [71]. The amplitude of the generated combination frequency is indicative of the degree of damage in a sample [72]. Nonlinear elastic wave spectroscopy, a technique to assess the damage in nonlinear elastic materials, involves emitting two single-frequency waves that interfere in a damaged sample and recording the amplitude of the received side-band frequency compo-

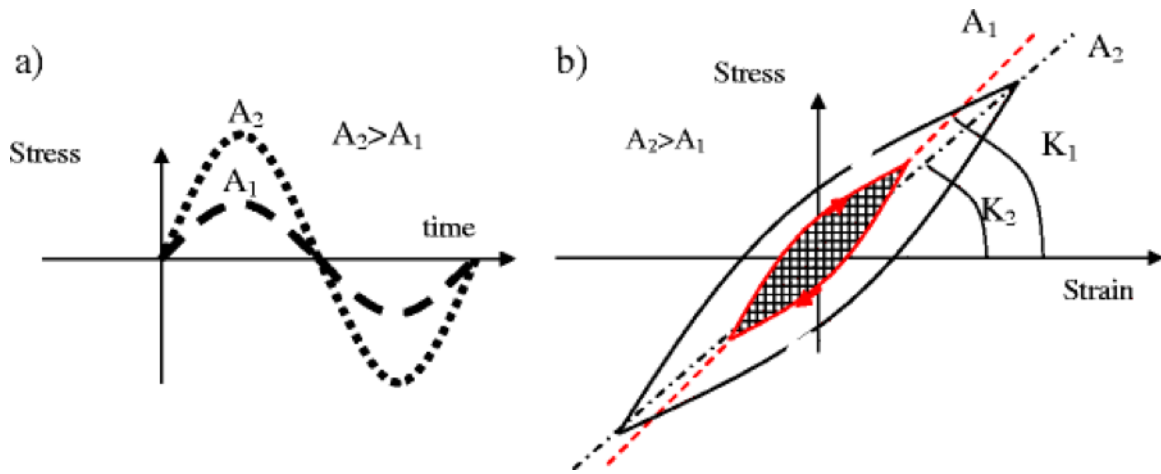


Figure 1.4: (a) One cycle of the variable stress field with amplitudes $A_2 > A_1$. (b) Stress-strain curves for two different amplitudes of the stress field. These stress-strain curves form loops with average modulus K_1 and K_1 ; the shaded area denotes the energy dissipated during the loading (A_1). The graph is adapted from Meo et al. [3].

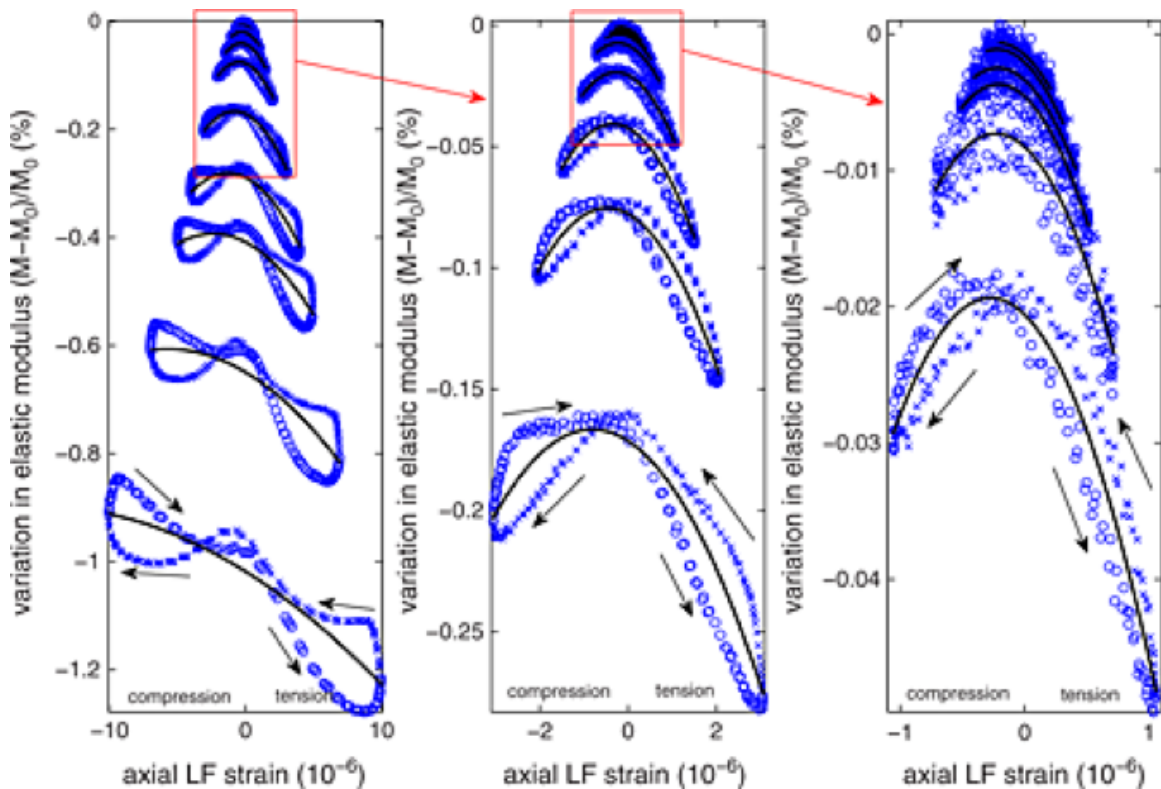


Figure 1.5: Variation of the elastic modulus of the Berea sandstone during a cycle of the stress field. The graph is adapted from Renaud et al. [1].

nents [41, 73]. Nonlinear elastic wave spectroscopy, used in nondestructive testing, has been widely applied to aircraft foam sandwich [74], concrete cover [25], composite plates [75], and a glass bead package [76] for crack detection.

Elastic waves with a wide frequency bandwidth experience nonlinear dissipation and attenuation [19, 21, 77–79]. The generation of side-band frequency components increases the high-frequency components of the waves; high-frequency energy attenuates faster than low-frequency energy. Hence, the Luxemburgh-Gorky effect intensifies attenuation of elastic waves in a nonlinear elastic material [14, 80, 81].

Theoretical models can explain the above-mentioned nonlinear mesoscopic elasticity and the observed features in laboratory measurements. These nonlinear features originate from bond ruptures and reconstructions in mesoscopic fractures [82, 83]; these physical/chemical processes occur at the nanoscale [84]. Barsoum et al. [85] show the interaction between fractures such as crystal dislocations and granular microcontacts in solids and ultrasound waves; their experiment shows the effect of temperature on dislocation-based incipient kink bonds. The higher temperature causes stronger nonlinearity with a larger resonant frequency shift observed in resonance experiments.

For slow and fast dynamics, existing models incorporate thermodynamics, which involves both activation and relaxation processes of the fractures to open and to be closed. Snieder et al. [86] explain the log-time recovery using a multiscale relaxation scheme, which simulates the process of fracture closure in a sample [87]. Vakhnenko et al. [88] simulate slow dynamics with the connection and breaking of interlaminar cohesive bonds; a two-level energy system is proposed for fractures with a bistable transition process that allows for cohesive and repulsive forces among microcontacts at mesoscopic scales [21, 89]. With a thermodynamics-based model, Zaitsev et al. [84] show the memory and aging effects that are closely related to slow dynamics. Li et al. [90] verify the contribution of bond breaking and linking to slow dynamics by observing the reconstruction of the broken chemical bonds; the reconstruction process is varying linearly with the logarithm of time.

Preisach-Mayergoyz theory (PM model) [91, 92] can explain the hysteresis observed in granular solids using “hysteretic mesoscopic units” that vary with scales. The PM model incorporates a multiscale superposition of the hysteretic mesoscopic units to simulate softening and recovery of granular solids in response to dynamic deformation. In addition, a nonlinear oscillator built based on the PM model can simulate resonance experiments [93, 94]. However, Claytor et al. [95] propose a limitation of the PM model; the model fails to reproduce several stress-strain measurements at slow stress varying rates on various sedimentary rocks. In other words, the PM model is not effective in simulating the hysteresis of some rocks.

A nonlinear EOS with higher order coefficients can simulate nonlinear wave modulation with generated side-band frequency components [96, 97]. Abeele et al. [72] simulate nonlinear wave modulation using both classical and nonclassical nonlinearity. Also, Blanloeuil et al. [98] consider both the contact law and contact dynamics occurring at microcracks to simulate nonlinear wave modulation.

None of the above-mentioned models are purely physical; these models are either phenomenological or semi-phenomenological with some assumptions such as a nonlinear EOS, which could be empirically summarized from these observed nonlinear features (e.g., hysteresis loop) in granular solids.

1.3 Field observations

Apart from rocks and concrete in laboratory experiments, unconsolidated soils in the shallow Earth could also show nonlinear elasticity, i.e., a decrease of regional seismic velocity after the passage of seismic waves originating from remote earthquakes with large magnitudes; this near-surface velocity drop is observed during and after strong ground shaking [99]. Figure 1.6 gives an example of variations in the near-surface seismic velocity in Northern Chile [4]; abrupt changes in the velocity coincide with earthquakes as marked by the vertical bars in the lower panel. Renaud et al. [100] and Johnson et al. [101] conduct DAET-like field experiments on near-surface soils using active sources, i.e., vibrator truck; these experiments verify that near-surface soils soften in response to ground shaking.

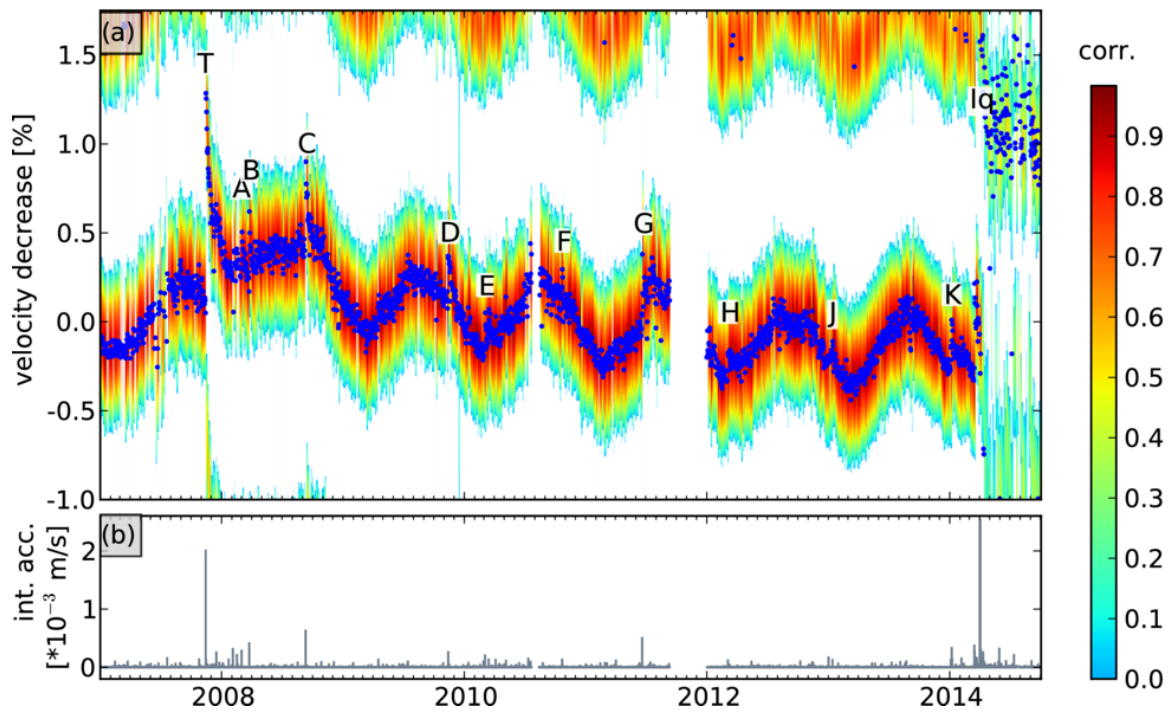


Figure 1.6: Eight-year variation of the seismic velocity in northern Chile in response to multiple ground shaking events. (a) Variation of the seismic velocity and the correlation coefficients denoted by the color bar. (b) Absolute ground acceleration recorded at a station. The graph is adapted from Gassenmeier et al. [4], and one can find more details therein.

Two main methods can be used to measure regional seismic velocity in the shallow Earth. First, one can use the seismic signals generated from repeated remote microearthquakes with close hypocenters in seismically active areas (e.g., volcanoes). The repeated microearthquakes could come from aftershocks of a large seismic event. One can also use a repeatable active source to generate the seismic signals [e.g., 101, 102]. Second, one can also use the noise data recorded in a region of interest.

The phases of the recorded signals from repeated microearthquakes could show time delays during strong ground shaking. S-wave traveltimes indicate the velocity variation in the shallow Earth. Rubinstein and Beroza [103] show fast excitation (velocity drop) and slow log-time recovery (velocity increase) of a fault zone using the variation of S-wave delay times (Loma Prieta Earthquake). Peng and Ben-Zion [104] show the seismic velocity drop due to the strong ground shaking at the Karadere-Düzce Branch of the North Anatolian Fault. Wu et al. [105] show the log-time recovery of the regional seismic velocity after the ground shaking (i.e., Karadere-Düzce main shock) using a series of signals obtained from microearthquakes. In addition, signals from repeated microearthquakes help monitor the variation of the seismic velocity across the fault zone in the San Andreas fault [106, 107]. One can use deconvolution interferometry [108, 109] to compute the near-surface softening during strong ground shaking with the data collected in a vertical array. Signals that are deconvolved from the data recorded at the top and bottom of the array give the variation of the seismic velocity in the shallow Earth. Nakata and Snieder [99] use deconvolution interferometry to analyze the data collected from Japanese KiK-net stations during the 2011 Tohoku-Oki earthquake; the analysis shows the reduction of the near-surface seismic velocity during the strong ground shaking and the recovery afterward. Other studies using the data from KiK-net stations involve the 2000 Tottori earthquake [110] and the 1995 Kobe earthquake [111].

Passive noise interferometry can be used to measure the average seismic velocity in the nearby region of a seismological site; seismic velocity at shallow depths can be monitored

using surface Rayleigh waves recorded as noise data. Hobiger et al. [112] measure the variation of the seismic velocity during and after the Iwate-Miyagi earthquake. Wegler et al. [113] show an abrupt decrease in the seismic velocity after the 2005 mid-Niigata earthquake. Gassenmeier et al. [4] show the temporal variation of the seismic velocity during and after multiple earthquakes in Chile for about eight years (see Figure 1.6). Ugalde et al. [114] apply noise interferometry to monitoring the seismic velocity at Colorado Paradox valley regarding the effect of temperature and the change of underground water level. Lieou et al. [115] and Gassenmeier et al. [116] attempt to simulate the variation of near-surface seismic velocity due to multiple events of ground shaking and match the simulated variation with the measured velocity variation. Chaves and Schwartz [117] identify pressurized fluids in subduction zones using the transient change of the seismic velocity at a depth below 5 km in response to the passage of seismic waves with a large wave amplitude.

Rubinstein and Beroza [118] show that pre-existing damage increases susceptibility to further damage (velocity drop) during strong ground shaking. In summary, nonlinear elasticity (softening) depends on the degree of damage in a solid sample in laboratory measurements and the damage of near-surface layers in field measurements.

CHAPTER 2

NONLINEAR OSCILLATORS

Resonance experiments can measure the nonlinear elasticity of granular solids including rocks and concrete [2, 60, 87]. The experiments typically involve a normal or torsional stress field that is applied to a cylindrical sample [30, 62]. The stress field drives a forced oscillation where different driving (stress) frequencies give different response amplitudes. Such an oscillation features a stable (strain) amplitude when the oscillation is sustained for a long time. Resonance experiments produce resonance curves where the response amplitudes are plotted against a range of driving frequencies, which commonly cover the resonant frequency of the sample. When the driving frequency is equal to the resonant frequency, the response amplitude reaches a maximum that is referred to as the resonant peak of the resonance curve.

Resonance experiments measure resonant frequency, which reveals the elastic property of a sample. The experiments have a mathematical equivalence, i.e., damped elastic oscillation. In this chapter, I introduce several mathematical nonlinear oscillators and their imprints on physical resonance experiments.

A damped nonlinear elastic oscillator can describe the dynamic deformation of a solid sample that is conditioned by a stress field. The following differential equation describes such an oscillator:

$$\frac{\partial^2 x}{\partial t^2} + \phi \frac{\partial x}{\partial t} + \sigma(x) = F_d(t), \quad (2.1)$$

where x is the dimensionless strain amplitude, ϕ is the damping factor (unit s^{-1}) of the sample, $\sigma(x)$ is a nonlinear EOS as a function of the strain x , and $F_d(t)$ is a driving field with unit s^{-2} . The driving field consists of sinusoidal input pump waves $F_d(t) = A_r \sin(\omega t)$ where A_r is the driving amplitude, and ω is the driving angular frequency; the driving amplitude is related to the driving force F_r using $A_r = F_r/ML_0$ where M is the mass and L_0 is the length of the bar (i.e., sample). Such sinusoidal pump waves have been used

in laboratory measurements [33]. The amplitude of pump waves is the main factor that determines the intensity of the dynamic deformation [14, 15, 30, 31, 63]. When the stress is a linear function of the strain, namely $\sigma(x) = kx$ where k is the linear elastic coefficient (unit s^{-2}), equation 2.1 becomes a linear oscillator that follows a linear EOS (Hooke's law); this linear EOS applies to elastic materials such as springs and plastics. For granular solids including natural rocks and concrete, the stress $\sigma(x)$ is a nonlinear function of the strain x , especially when the strain x is large, and a strong deformation exists.

A nonlinear EOS can phenomenologically include linear elasticity, classical atomic nonlinear elasticity, and nonlinear mesoscopic elasticity; hence, several schemes of the nonlinear EOS as a function of the strain x have been formulated. Pasqualini et al. [13] apply a nonlinear EOS that is effective for a small strain amplitude with the weak nonlinearity; the EOS follows

$$\sigma(x) = kx + \delta x^3, \quad (2.2)$$

where δ is the cubic anharmonic coefficient, and k is the linear elastic coefficient. Merging equations 2.2 and 2.1 gives the Duffing equation [119, 120], which includes the atomic anharmonicity in a low strain regime [57]. In addition, one can describe the anharmonicities with higher order terms for a one-dimensional lumped element (spring-mass) system using

$$\sigma(x) = K(x + \beta x^2 + \delta x^3 + \dots), \quad (2.3)$$

where K is an elastic factor, and both β and δ are classical nonlinear coefficients that describe anharmonicities in the classical nonlinear elasticity [20, 121–123]. Gallot et al. [41] and Lott et al. [33] extend equation 2.3 into a three-dimensional case where a stiffness tensor describes the nonlinear elasticity in different directions of the deformation.

Ostrovsky and Johnson [14] further consider the hysteresis observed in stress-strain curves and include the strain rate $\dot{x} = \partial x / \partial t$ in a nonlinear EOS:

$$\sigma(x, \dot{x}) = K(x + \beta x^2 + \delta x^3 + \dots) + S(x, \dot{x}), \quad (2.4)$$

where S is a function that phenomenologically describes the hysteresis loop with the non-linear mesoscopic elasticity and attenuation (creep). The overdot denotes a time derivative. The expression of $S(x, \dot{x})$ takes the topology of hysteresis loops into account. The topology of the loop could be a butterfly, starting from the zero point on the σ - ϵ plane, and could involve periodic motions surrounding the zero point [for more detail, see refs. 14, 124]. A general form of the function S originates from the PM space approximation [53]; this function describes the shape of the hysteretic stress-strain loop [67]. For a one-dimensional EOS, S could be in the form

$$S(x, \dot{x}) = \alpha(\Delta x + x \times \text{sign}(\dot{x}) + \dots), \quad (2.5)$$

where Δx is the strain amplitude calculated from the previous period of strain oscillation, $\Delta x = (x_{max} - x_{min})/2$, and α is a hysteretic nonlinear parameter [121, 122, 125, 126]. Hauptert et al. [29] further incorporate a cross term $x \times \Delta x$ and a second-order term $\text{sign}(\dot{x})[(\Delta x)^2 - x^2]$ into the function S . Apart from the sign of the strain rate, Pecorari [39] further considers a term containing the value of the strain rate \dot{x} for material creep (attenuation). Brunet et al. [55] interpret the nonlinear features observed in a glass bead pack using the concept of Hertzian microcontacts and simplify the function S into

$$S = \eta \dot{x}, \quad (2.6)$$

where η is a loss term for internal dissipation in the sample. Lyakhovskiy et al. [127] follow both the linear continuum damage model [128] and Kelvin-Voigt rheology model incorporated with the material creep and attenuation to build a one-dimensional bilinear nonlinear EOS:

$$\sigma(x) = E_0[(1 - \frac{\chi}{2})x - \frac{\chi}{2}|x| + \eta \dot{x}], \quad (2.7)$$

where E_0 is the elastic modulus of an damaged (unstrained) sample, χ is a damage state variable ($0 \leq \chi \leq 1$), and η is a loss term (i.e., viscosity). The damage state χ increases with the number of oscillation cycles, and the increase rate can be constrained by the laboratory measurements where the sample is dynamically loaded under different conditions (e.g., stress varying rate) [129, 130]. When one extends the sample with a positive strain, i.e., $x > 0$,

equation 2.7 becomes

$$\sigma(x) = E_0[(1 - \chi)x + \eta\dot{x}], \quad (2.8)$$

where the term $(1 - \chi)x$ describes the softening of the damaged sample in response to extension. When one compresses the sample, i.e., $x < 0$, equation 2.7 becomes

$$\sigma(x) = E_0[x + \eta\dot{x}], \quad (2.9)$$

where the damage variable χ vanishes. In other words, compression does not affect the elastic modulus while extension softens the sample. Equation 2.7 is reminiscent of fracture contact models such as Hertzian microcontacts [20, 21] where the deformation is not symmetric for compression and extension. The detachment of fracture contacts softens the sample while the attachment does not change the elastic modulus.

The above-mentioned EOSs are explicit functions where stress σ can be expressed as a function of strain ϵ using one equation. An implicit EOS can also build a nonlinear oscillator that incorporates a strain-dependent time-evolved elastic modulus.

Delsanto and Scalerandi [93] apply a PM-based model that accounts for the concept of hysteretic mesoscopic units in a granular solid (sample); each unit has two states and allows for thermally induced transitions between states [22]. A driving stress field can change these bistable states, and the change of states feeds back into the elasticity of the sample. A granular solid contains both hard elements such as mineral grains and soft elements that can be represented by the hysteretic mesoscopic units. Averaging elastic moduli of the hard and soft elements gives the elasticity of the sample [21]. Gliozzi et al. [94] further apply the concept of linear and damaged elements (i.e., hysteretic mesoscopic units) for the hard and soft parts in rocks.

Vakhnenko et al. [88] consider broken intergrain and interlaminar cohesive bonds as the soft elements in rocks; the equilibrium concentration of the soft elements (e.g., open fractures) in a sample depends on the stress in a thermodynamics scheme:

$$c_\sigma = c_0 \exp^{v\sigma/k_B T}, \quad (2.10)$$

where c_σ is the fracture concentration, c_0 is the fracture concentration of an unstrained bar (sample), k_B is the Boltzmann constant, T is the temperature of the sample, and v is a constant. The fracture concentration in the sample changes the elastic modulus; Vakhnenko et al. [83] assume a linear decrease of Young's modulus with the concentration of fractures.

Guyer et al. [131] show an oscillation equation that incorporates cubic and quartic anharmonicities as well as hysteresis that accounts for different elastic moduli in compression and extension. Also, the oscillation equation incorporates time-evolved elastic modulus that can change over time during and after dynamic deformation. However, such a theoretical model does not account for slow dynamics with the *log-time* recovery.

On top of these implicit nonlinear oscillators, Chapter 3 contains a simple thermodynamics-based model to simulate resonance experiments for all the observed experimental features. The model follows Vakhnenko et al. [88], which includes (a) a linear decrease of Young's modulus with fracture density and (b) a thermodynamics-based theory for the time-evolved elastic modulus.

2.1 Numerical solution

I show a simple example of the nonlinear oscillation using equation 2.2 where the cubic anharmonicity is used to produce the Duffing equation. The solution of the Duffing equation can be indicative of the nonlinear features observed in resonance experiments.

Merging equations 2.1 and 2.2 gives the Duffing equation with the following form

$$\frac{\partial^2 x}{\partial t^2} + \phi \frac{\partial x}{\partial t} + kx + \delta x^3 = A_r \sin(\omega t). \quad (2.11)$$

Although the harmonic balance method can solve the above equation using perturbation theory [13, 132, 133], I solve the equation using the finite difference method, which could display the strain oscillation at the beginning of the dynamic deformation.

I use the values of the Duffing parameters, as shown in Table 2.1 for the following simulations unless indicated otherwise. These parameter values involve a static resonant frequency 3900 Hz of an unstrained sample and significant softening of the sample when $|x|$ is of the

order 10^{-6} . This behavior of softening in both compression and extension is different from the case where granular solids such as rocks soften in compression and harden in extension.

Table 2.1: Numerical values of the parameters used in equation 2.11.

	Definition	value
ϕ	Damping factor	180 s^{-1}
k	Linear elastic coefficient	$4\pi^2 \times 3900^2 \text{ s}^{-2}$
δ	Cubic aharmonic coefficient	$-9 \times 10^{17} \text{ s}^{-2}$
t_s	Numerical time step	10^{-5} s

I solve the Duffing equation using the driving amplitude $A_r = 13.2/\text{s}^2$, the initial condition of the strain $x(0) = 0$ and the strain rate $\dot{x}(0) = 0$, and the driving frequency $f_d = 3880 \text{ Hz}$. Figure 2.1 shows the numerical solution of the time-evolved strain in response to the driving stress. The forced oscillation includes an early transient state during which the deformation amplitude varies with time. After a time duration of about 0.05 s, the oscillation stabilizes; such the sustained oscillation amplitude is the measured quantity in resonance experiments.

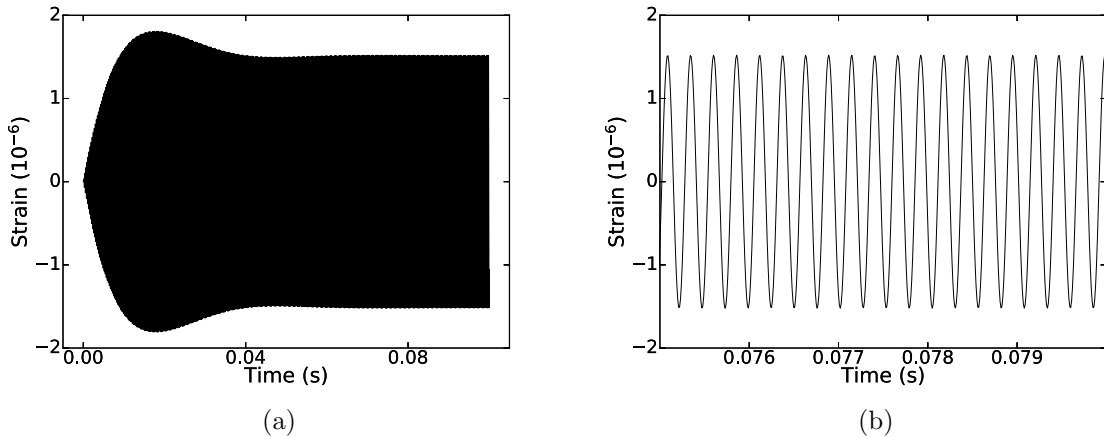


Figure 2.1: Numerical solution of the Duffing equation for the temporal variation of the strain x in response to the driving field $F_d(t)$. (a) The appearance of the curve as a thick line results from the high-frequency fluctuation that is not resolved in the graph. (b) A zoom-in of the high-frequency oscillation.

For different driving frequencies, one can get different response amplitudes that are obtained at the end of the oscillations with a steady state. Figure 2.2 shows the “Duffing resonance curve” obtained from the solution of the Duffing equation. A resonant frequency shift occurs when the resonant peak deviates from the static resonant frequency 3900 Hz to the left along the frequency axis.

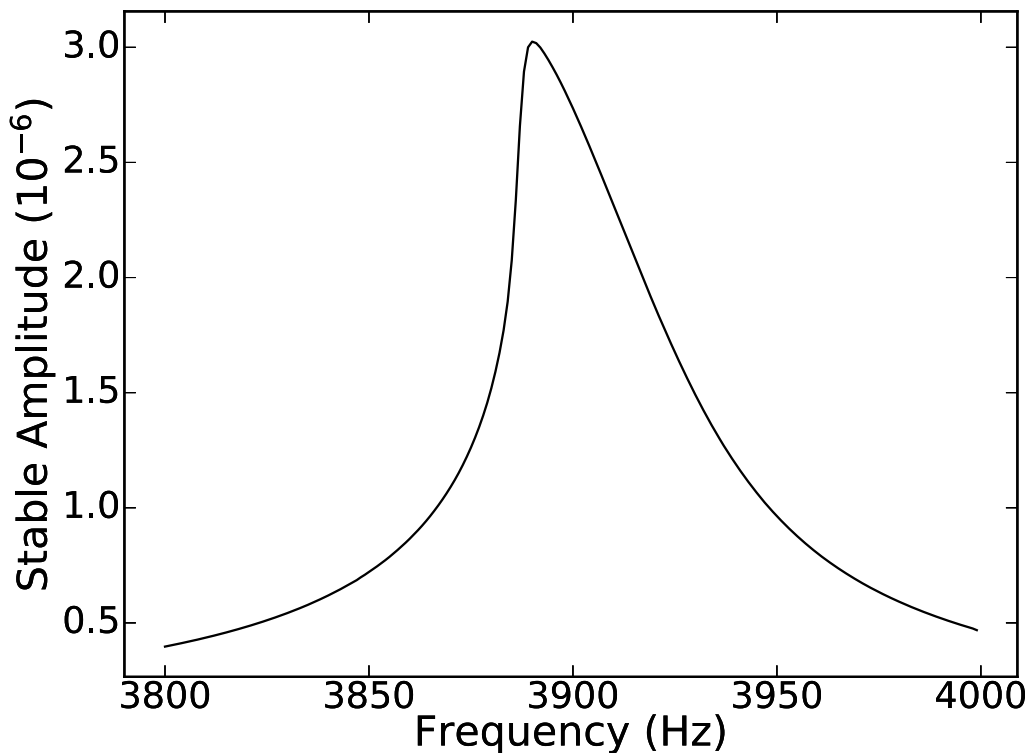


Figure 2.2: Duffing resonance curve obtained from the solutions of the Duffing equation. The graph shows the solutions of stable amplitudes for different driving frequencies. The driving amplitude is $A_r = 13.2/s^2$ and the anharmonic coefficient is $\delta = -9 \times 10^{17}$.

Three important factors determine the solution of the Duffing equation: the driving amplitude, the driving frequency, and the initial condition of the strain $x(0)$. These factors affect the shape of the resonance curves produced by the solution of the Duffing equation. I apply the same initial condition of the strain rate $\dot{x}(0) = 0$ to all the following simulations.

The increase in nonlinearity changes the shape of the resonance curve. Two ways exist to increase the nonlinearity of the oscillation system. One can increase the driving amplitude A_r or increase the absolute value of the anharmonic coefficient δ . The former is equal to increasing the intensity of the driving stress field in resonance experiments, and the latter involves the intrinsic nonlinear elasticity that is related to the degree of damage (i.e., fracture concentration) in granular solids including rocks and concrete. I increase the driving amplitude A_r from $13.2/s^2$ (used in Figure 2.2) to $35.2/s^2$. Consequently, Figure 2.3 shows a resonance curve with a “cliff” that indicates an abrupt change of the response amplitude when the driving frequency is changed. Also, Figure 2.4 shows the resonance curve with the cliff when the driving amplitude is still $A_r = 13.2/s^2$ but the value of $|\delta|$ increases to $\delta = -15 \times 10^{17}$.

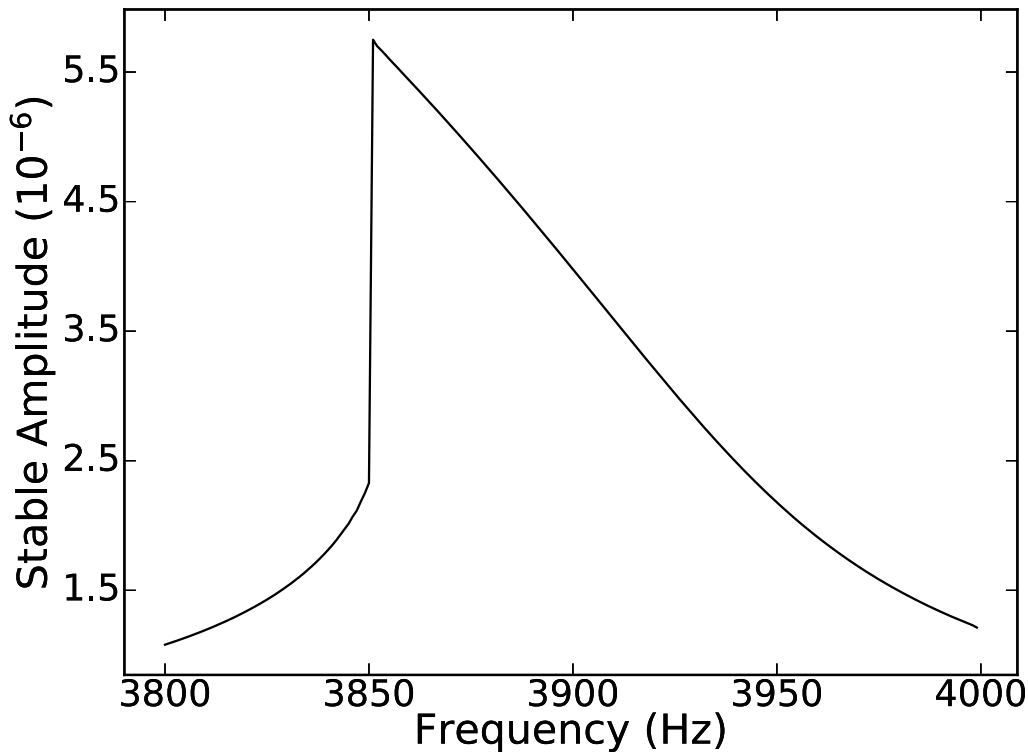


Figure 2.3: Duffing resonance curve with the driving amplitude $A_r = 35.2/s^2$.

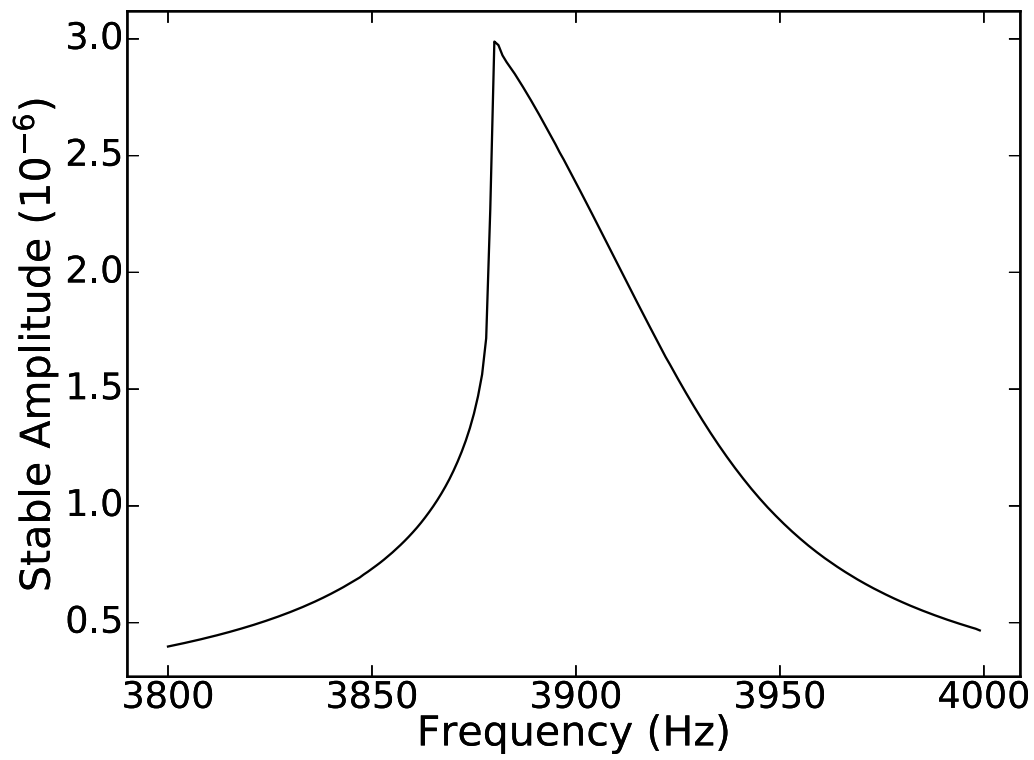


Figure 2.4: Duffing resonance curve with the anharmonic coefficient $\delta = -15 \times 10^{17}$.

Figure 2.3 and Figure 2.4 both display a cliff in the resonance curves. With the increase in nonlinearity, the Duffing resonance curve features the presence of the cliff which is indicative of the level of nonlinearity in the oscillation system.

When the cliff is present in Duffing resonance curves, the initial condition of the strain $x(0)$ influences the shape of the curves. In this case, the initial condition $x(0)$ could affect the solution of the Duffing equation, i.e., stable amplitude. Figure 2.5 shows the time-evolved deformation with low ($x(0) = 0$) and high ($x(0) = 4 \times 10^{-6}$) initial strains. The black areas indicate the high-frequency oscillations and denote envelopes that reflect the temporal variations of the deformation amplitudes. Two different initial conditions of the strain result in two different stable response amplitudes.

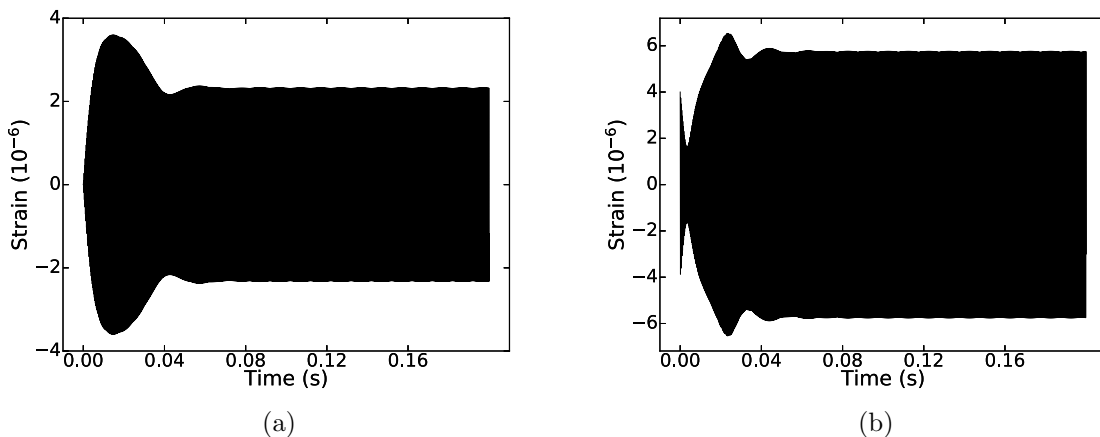


Figure 2.5: Numerical solutions of the Duffing equation for the temporal variations of the strain x with different initial conditions: (a) initial strain $x(0) = 0$ and (b) $x(0) = 4 \times 10^{-6}$. The driving frequency is $f_d = 3850$ Hz and the driving amplitude is $A_r = 35.2/s^2$.

I further produce the Duffing resonance curves using (a) the two initial conditions of strain $x(0) = 0$ and $x(0) = 4 \times 10^{-6}$ for all the driving frequencies and (b) the driving amplitude $A_r = 35.2/s^2$, as shown in Figure 2.6. A difference between the two Duffing resonance curves exists at the left of the resonant peak (on the green line); such a difference highlights the effect of the initial condition in the solution of the Duffing equation. However, when the nonlinearity is weak, the difference between the Duffing resonance curves vanish,

as shown in Figure 2.7 where the driving amplitude is $A_r = 13.2/s^2$. Thus, I conclude that such a curve difference can only exist when the nonlinearity is strong with a cliff present in resonance curves.

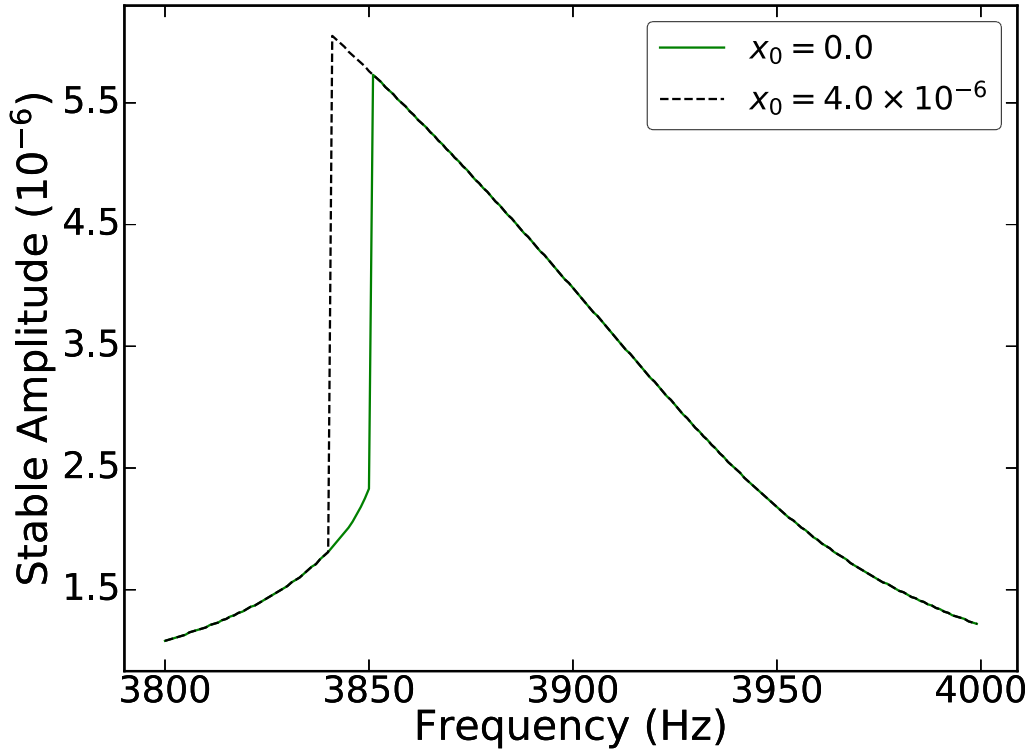


Figure 2.6: Duffing resonance curves with two initial conditions, i.e., (a) initial strain $x(0) = 0$ and (b) $x(0) = 4 \times 10^{-6}$. The driving amplitude is $A_r = 35.2/s^2$.

The curve difference, resulted from the strong nonlinearity, refers to a bifurcation [120], as shown in Figure 2.8. When one reduces the driving frequency at point d , the solution of the Duffing equation jumps abruptly to point a ; when one increases the driving frequency at point b , the solution jumps to point c . The increase in nonlinearity causes these jumps that represent the bifurcation and are a distinctive feature described by catastrophe theory [134, 135]. The bifurcation occurring in the oscillation system indicates that two stable amplitudes may exist for an oscillation with a driving frequency; the choice of the oscillation

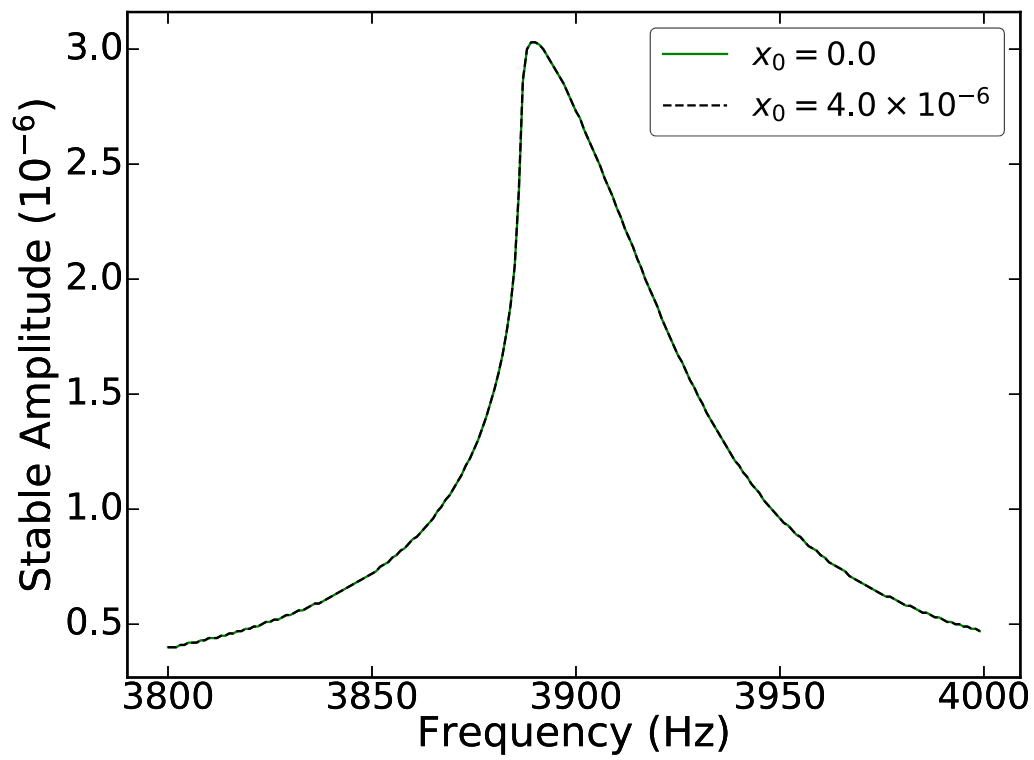


Figure 2.7: Duffing resonance curves with two initial conditions, i.e., (a) initial strain $x(0) = 0$ and (b) $x(0) = 4 \times 10^{-6}$. The driving amplitude is $A_r = 13.2/s^2$.

amplitude (solution) depends on the initial condition of the strain, either a low initial value for the unstrained sample or a high value for the conditioned sample. The presence of the bifurcation requires (1) strong nonlinearity induced by a large driving amplitude or deformation amplitude, and/or (2) relevant driving frequencies corresponding to the difference area (see Figure 2.6).

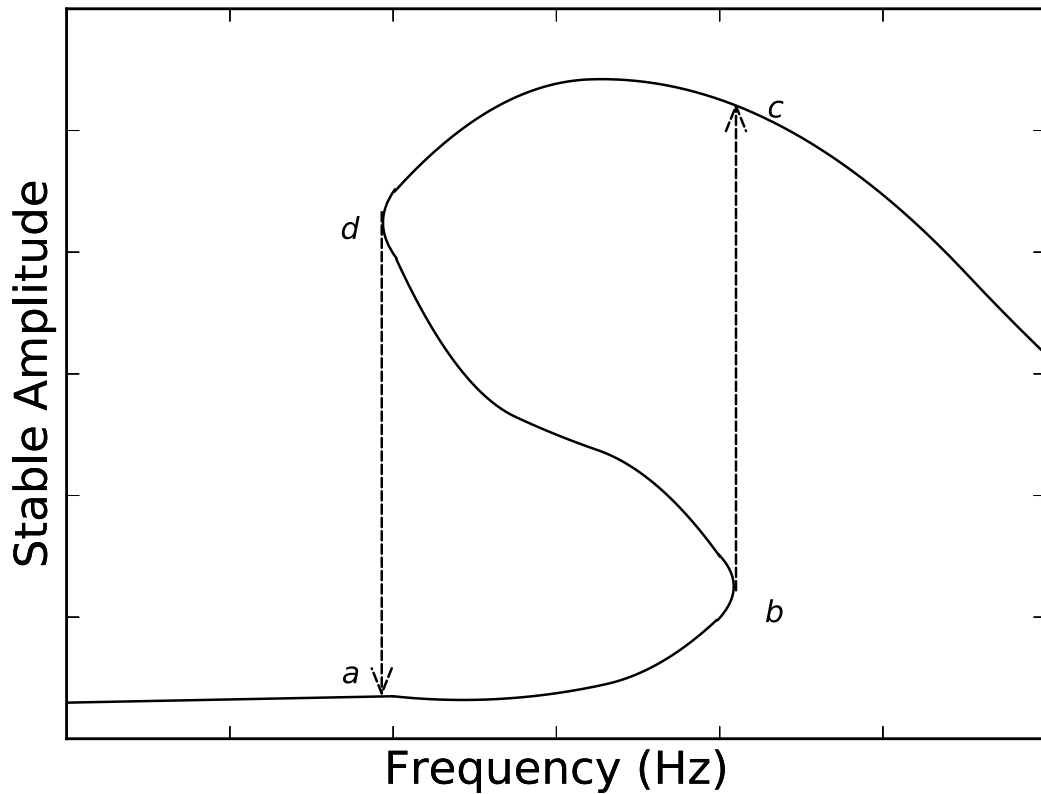


Figure 2.8: Schematic graph of the bifurcation.

In summary, three factors count in the solution of the Duffing equation. The extrinsic driving amplitude and intrinsic anharmonic coefficient control the degree of nonlinearity in an oscillation system. When the nonlinearity is strong, a bifurcation is present with a cliff in the resonance curve, and a difference exists between the resonance curves produced with two different initial conditions of the strain. The presence of the cliff in resonance curves is indicative of the bifurcation and hence the degree of the nonlinearity.

One should be aware of the difference between mathematical nonlinear oscillators such as the Duffing equation and physical laboratory resonance experiments. Nonlinear oscillators such as the Duffing oscillator usually do not account for slow dynamics, and thus do not depend on the time-scales inherent in the relaxation and activation processes. Thus, these nonlinear oscillators cannot simulate slow dynamics. The simulations based on these explicit nonlinear EOSs cannot reproduce the recovery process after dynamic deformation ends. Such a limitation indicates that these nonlinear oscillators cannot directly simulate the resonance experiments where samples are granular solids with mesoscopic nonlinear elasticity. Several studies apply an implicit nonlinear EOS incorporated with a time-evolved variable that allows the elastic modulus to be conditioned and to recover [e.g., 131]. Also, the above-mentioned nonlinear oscillation systems do not include the measurement protocol used in resonance experiments [5, 30]. In laboratory experiments, the driving frequency changes by some value after a certain time duration, which enables the oscillation to stably stay with an amplitude. When solving the Duffing equation, one computes response amplitudes for driving frequencies using the same initial condition. However, in laboratory measurements, the initial condition of each oscillation with a driving frequency depends on the elastic state at the end of the oscillation with the last driving frequency.

The simulations and solutions of the Duffing equation are indicative of the observed nonlinear features in laboratory experiments. Chapter 3 contains the simulation of resonance experiments using a simple thermodynamics-based model that accounts for slow dynamics in an implicit nonlinear oscillator; the simulation also includes the laboratory measurement protocol (see Appendix A). Hence, the solutions of the Duffing equation help build a unified interpretation of the nonlinear elasticity observed in resonance experiments.

CHAPTER 3

NONLINEAR ELASTICITY IN RESONANCE EXPERIMENTS

A paper accepted at *Physical Review B*

Xun Li^{1,2}, Christoph Sens-Schönfelder³, Roel Snieder²

Resonant bar experiments have revealed that dynamic deformation induces nonlinearity in rocks. These experiments produce resonance curves that represent the response amplitude as a function of the driving frequency. We propose a model to reproduce the resonance curves with observed features that include (a) the log-time recovery of the resonant frequency after the deformation ends (slow dynamics), (b) the asymmetry in the direction of the driving frequency, (c) the difference between resonance curves with the driving frequency that is swept upward and downward, and (d) the presence of a “cliff” segment to the left of the resonant peak under the condition of strong nonlinearity. The model is based on a feedback cycle where the effect of softening (nonlinearity) feeds back to the deformation. This model provides a unified interpretation of both the nonlinearity and slow dynamics in resonance experiments. We further show that the asymmetry of the resonance curve is caused by the softening, which is documented by the decrease of the resonant frequency during the deformation; the cliff segment of the resonance curve is linked to a bifurcation that involves a steep change of the response amplitude when the driving frequency is changed. With weak nonlinearity, the difference between the upward- and downward-sweeping curves depends on slow dynamics; a sufficiently slow frequency sweep eliminates this up-down difference. With strong nonlinearity, the up-down difference results from both the slow dynamics and bifurcation; however, the presence of the bifurcation maintains the respective part of the up-down difference, regardless of the sweep rate.

¹Primary author and editor

Corresponding author

²Center for Wave Phenomena, Colorado School of Mines, Golden, Colorado 80401, USA

³GFZ German Research Centre for Geosciences, Potsdam, Germany

3.1 Introduction

Resonant bar experiments can be used to measure the nonlinear elasticity of natural rocks or concrete and further monitor small changes of elasticity (velocity) with high accuracy [2, 60, 87]. In resonance experiments, a dynamic normal force imposes cyclic compressions and extensions on a cylindrical rod with a driving frequency that can be changed, continuously sweeping towards higher or lower values [30, 62, 136]. For each driving frequency, the dynamic deformation of the rod gradually reaches a state where the oscillation has a stable amplitude; such an amplitude defines the measured response for the corresponding driving frequency [5, 30, 137]. The dependence of the response amplitude on the driving frequency generates a resonance curve that can be used to characterize the elastic property of rocks [60].

Laboratory measurements produce resonance curves with the following features [2, 5, 30, 60, 87, 137]. The resonant peak shifts towards lower frequency for an increasing driving force and shifts back towards higher frequency in the recovery process [21]. The resonant frequency recovers with the logarithm of time after the deformation ends (slow dynamics) [87]. Resonance curves are asymmetric along the frequency axis around their peak frequency as soon as the driving force is strong enough to induce softening [2]. With an increase in the driving force, the resonance curve steepens to the left of the resonant peak and flattens to the right of the peak. Ten Cate and Shankland [60] show that a difference exists between the upward and downward resonance curves, produced by sweeping the driving frequency upward and downward, respectively. This up-down difference is most pronounced to the left of the resonance. TenCate [2] finds that a slow sweep of the driving frequency can eliminate the up-down difference and produce the same resonance curves, regardless of the sweep direction. Johnson et al. [5] show that strong nonlinearity in rocks induces a vertical segment of the resonance curve to the left of the resonant peak. This vertical segment, which we refer to as the “cliff,” involves a large abrupt change of the response amplitude when the driving frequency is increased/decreased. The response amplitude changes upward/downward along the cliff as the driving frequency passes the resonant peak. We present a theory for the above-

mentioned experimental features of resonance curves using a simple thermodynamics-based model.

In this paper, section 3.2 starts from a feedback cycle as the framework of our thermodynamics-based model; we then propose the relationship between dynamic deformation and thermal activations/relaxations of fractures. Taking the feedback of the fracture behavior on Young’s modulus into account, we conduct the simulation of resonance experiments following the protocol used in the laboratory (Section 3.3). Section 3.4 shows that our model can reproduce resonance curves with the observed features, including (a) the slow dynamics with log-time recovery, (b) the asymmetry of resonance curves, (c) the disappearance of the up-down difference at a slow sweep rate of the driving frequency, and (d) the presence of the cliff in the resonance curve when the nonlinearity is strong. Additionally, our model predicts that the steep cliff with strong nonlinearity is related to a permanent up-down difference that does not vanish for a slow sweep rate. This has not been observed experimentally, yet. Finally, in section 3.5, we propose a unified interpretation of all these observed features; this interpretation enhances the understanding of both the nonlinear elasticity and slow dynamics in resonance experiments.

3.2 Model

Different micromodels can simulate resonance experiments where dynamic deformation leads to a reduction of resonant frequency (Young’s modulus); this reduction reflects the softening of rocks [5, 13, 57, 131, 138]. We propose a simple thermodynamics-based model, following ref. [83, 84, 92, 127] that is based on (a) bond rupture/healing and (b) an oscillation equation, to simulate both slow dynamics and resonance curves. Our model can include the concept of “effective” granular temperature for the vibration energy [55, 139, 140]. However, our model does not involve a detailed upscaling generalization from microscale to macroscale and does not rely on a complicated description of physics mechanisms as in earlier work [21, 89, 90].

3.2.1 Feedback cycle

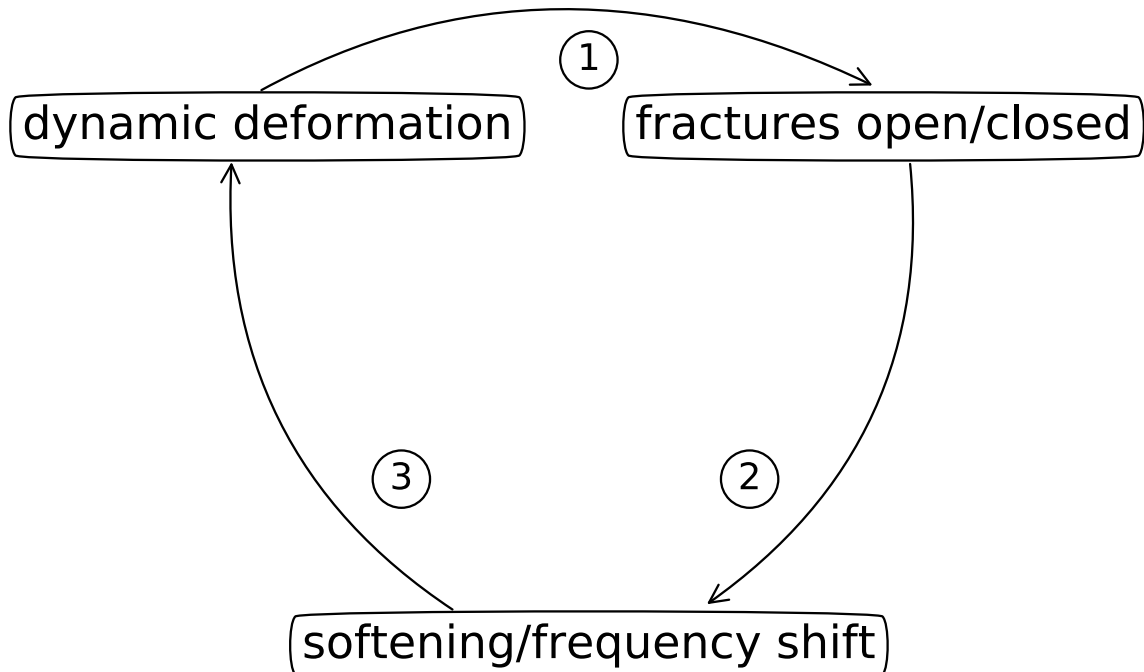


Figure 3.1: Feedback cycle for nonlinear material properties.

We use a feedback cycle for the material response shown in Figure 3.1 that is akin to a theory for liquefaction [141]. The feedback cycle is the base of the thermodynamics-based parametrization in our model. Link 1 in the cycle accounts for the change of fracture system due to dynamic deformation, while link 2 describes the change in the elasticity (softening) due to the opening of fractures. The change of the elasticity feeds back to the deformation amplitude (link 3). We use “fractures” as a general term for cracks, contacts, bonds, and microcontacts. A solid sample contains fractures with scales ranging from microscopic dislocation defects in crystals to mesoscopic granular contacts and to macroscopically visible cracks [22].

3.2.2 Thermodynamics-based parametrization

We consider a bistable model where a fracture can be in one of two configurations: open or closed, with associated energy levels E_o and E_c , respectively, as shown in Figure 3.2. We assume that an energy barrier E_b needs to be overcome for the fracture to change the configuration. This bistable model follows earlier energy models for the fracture contact [21, 84, 89, 142].

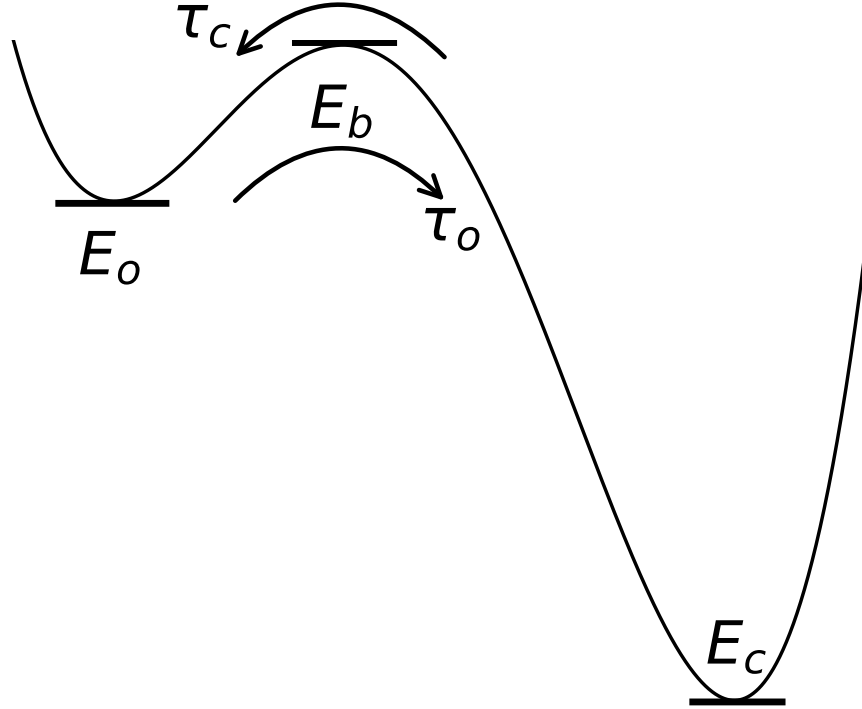


Figure 3.2: bistable energy model for a fracture. For a barrier energy E_b , τ_c and τ_o indicate the transition times to open and close the fracture, respectively.

We further consider that due to the thermal energy $k_B T$, a fracture can spontaneously change its configuration with characteristic transition times τ_o to close a fracture and τ_c to open a fracture, following Arrhenius law [143, 144]:

$$\tau_o = A e^{(E_b - E_o)/k_B T}, \quad \tau_c = A e^{(E_b - E_c)/k_B T}. \quad (3.1)$$

E_o and E_c are the energies of open and closed fractures, respectively. E_b is the barrier energy, k_B is the Boltzmann constant, T is the temperature, and A is a time constant. The bistable dynamic equation for a group of fractures with the same barrier energy is

$$\frac{dn_o}{dt} = -\frac{n_o}{\tau_o} + \frac{1 - n_o}{\tau_c}, \quad (3.2)$$

where n_o is the fraction of open fractures for a given barrier energy, and $n_c = 1 - n_o$ is the fraction of closed fractures. In equation 3.2, the first term on the right-hand side indicates the rate at which fractures close while the second term indicates the rate at which fractures open. In equilibrium $dn_o/dt = 0$, and thus the corresponding fraction n_{eq} of open fractures is

$$n_{eq} = \frac{1}{1 + \exp((E_o - E_c)/k_B T)}, \quad (3.3)$$

and hence n_{eq} is independent of the barrier energy. For $E_o \gg E_c$, most fractures are closed while with $E_c \gg E_o$, most fractures are open.

We assume that the barrier energies that correspond to fractures with different sizes are distributed uniformly in an interval $[E_{bmin}, E_{bmax}]$. The aggregate fracture system that includes fractures with different barrier energies has an average fraction of open fractures $N_o(t) = \int_{E_{bmin}}^{E_{bmax}} n_o(E_b, t) dE_b / (E_{bmax} - E_{bmin})$.

The fracture system affects the elasticity of the material [77, 145]; the opening of fractures lowers Young's modulus. For the link 2 in Figure 3.1, we linearize the relationship between Young's modulus Y and the fracture system N_o using

$$Y = Y_0 - C_0(N_o - N_{ori}). \quad (3.4)$$

N_{ori} is the equilibrium fraction of open fractures with zero strain ($\epsilon = 0$), C_0 is the fracture modulus, and Y_0 is the static Young's modulus of the unperturbed sample. Link 3 in Figure 3.1 indicates the feedback of the softening (reduction of Young's modulus) on the deformation amplitude; the feedback is introduced as a dependence of the energies E_c and E_o on the externally applied strain.

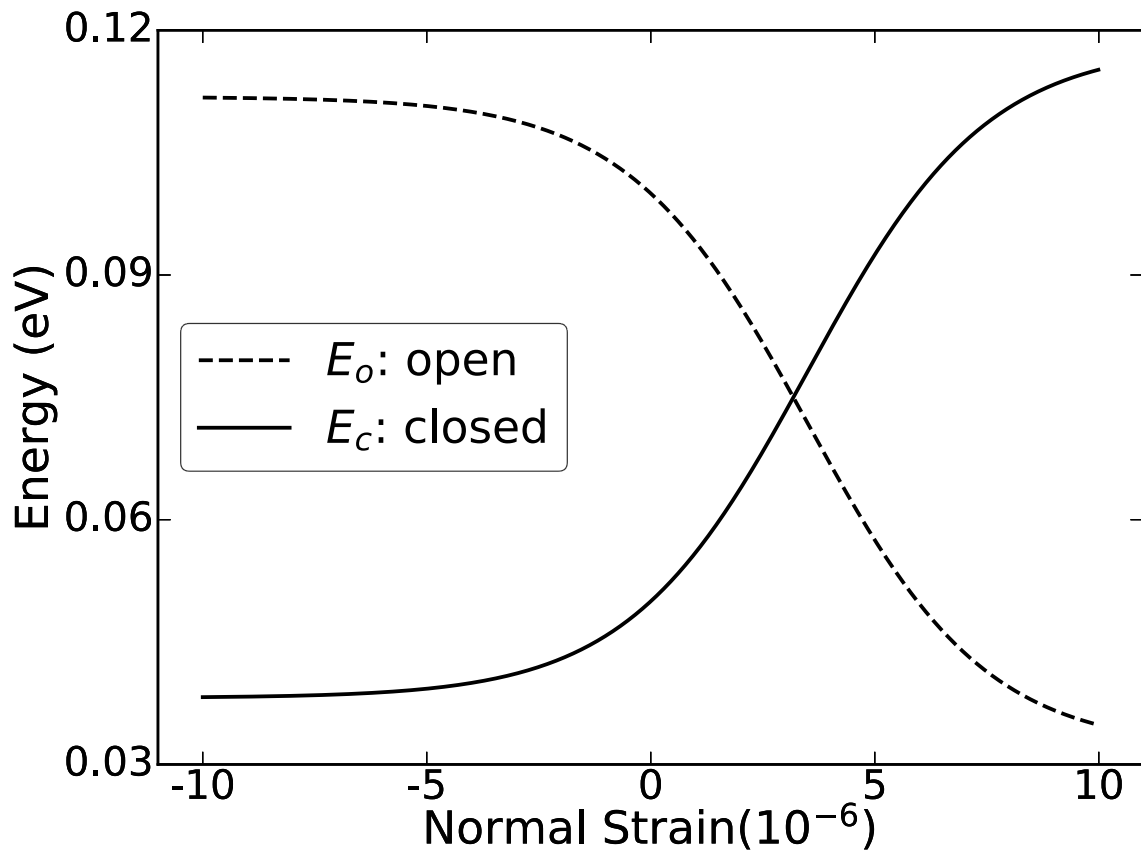


Figure 3.3: Energy levels of open and closed fractures as a function of the dynamic normal strain. Positive strain corresponds to extension, and negative strain corresponds to compression.

We propose a dependency of the energies of open and closed fractures as shown in Figure 3.3; this dependency is parameterized by the sigmoid functions:

$$E_o(\epsilon) = B_0 - \frac{A_1}{1 + \exp(-(\epsilon - \mu)/\sigma_c)} \quad (3.5)$$

and

$$E_c(\epsilon) = A_0 + \frac{A_1}{1 + \exp(-(\epsilon - \mu)/\sigma_c)}, \quad (3.6)$$

where A_0 , A_1 , B_0 , μ , and σ_c are constants, and ϵ is dynamic strain. This relationship is based on the premise that the deformation strain is the main factor affecting the nonlinear elasticity of rocks [63]. The nonlinearity of rocks becomes significant when the strain is of the order of a microstrain (10^{-6}) [13, 53, 63]. Thus, we prescribe a fracture energy that changes significantly once the strain is above 10^{-6} . For the strain range shown in Figure 3.3, the fracture energy implies (a) that extension opens fractures (softening) while compression closes fractures (hardening), and (b) that the response to deformation is not symmetric for the positive and negative strain. The asymmetry reflects that the elastic response is more sensitive to extension (positive strain) than to compression (negative strain) [6, 20]. However, the choice of the sigmoid function is quite arbitrary; it provides a smooth transition from a region that favors closed fractures to a region that favors open fractures. Figure 3.3 and the bistable model in Figure 3.2 act as the link 1 in Figure 3.1. We summarize the parameters used and their numerical values in Table 3.1.

For a temperature $T = 300$ K, the thermal energy is $k_B T = 0.026$ eV. The energy difference between open and closed fracture in Figure 3.3, together with equation 3.3, implies that for large positive strain ($\epsilon \gtrsim 7 \times 10^{-6}$) the system favors open fractures, while for compression and small positive strain ($\epsilon \lesssim 10^{-6}$) the system favors closed fractures. This description of fracture behavior is not necessarily accurate in its details and so should be seen as a plausible parametrization of fracture behavior. For some aspects of nonlinear material properties, the model may need to be extended to include the strain rate $\dot{\epsilon}$ as well as shear deformation [69, 146].

Table 3.1: Numerical values of the parameters used.

	Definition	value
A	Time constant	1.0 s
T	Temperature	300.0 K
E_{bmin}	Minimum barrier energy	0.223 eV
E_{bmax}	Maximum barrier energy	0.401 eV
A_0	Constant	0.038 eV
A_1	Constant	0.080 eV
B_0	Constant	0.112 eV
μ	Constant	3.5×10^{-6}
σ_c	Constant	2.0×10^{-6}
L_0	Length of sample	0.3 m
ρ	Density of sample	2200 kg/m ³
Y_0	Static Young's modulus	12.05 GPa
C_0	Fracture modulus	1.853 GPa
f_0	Static resonant frequency	3900 Hz
γ	Damping factor	90.0 rad/s
t_0	Numerical time step	5 μ s
τ_{max}	Maximum relaxation time	500 ms
Δt	Sweep time interval	5 ms
Δf	Sweep frequency interval	1 Hz

3.3 Resonance simulation

We describe the deformation in the resonant bar experiment by

$$\frac{\partial^2 R_A}{\partial t^2} + 2\gamma \frac{\partial R_A}{\partial t} + \Omega^2 R_A = A_r e^{-i\omega t}, \quad (3.7)$$

where R_A is the dimensionless strain amplitude (i.e., ϵ in equations 3.5 and 3.6) in response to the driving field $A_r e^{-i\omega t}$, γ is the damping factor, ω is the driving angular frequency, and Ω is the resonant angular frequency. The driving amplitude A_r is related to the driving force F_r using $A_r = F_r / ML_0$, where M is the mass and L_0 is the length of the sample. In equation 3.7, the resonant angular frequency incorporates the softening because it depends on Young's modulus: $\Omega = \pi \sqrt{Y/\rho} / L_0$, where ρ is density [5]. To first order, the resonant angular frequency shift relates to the reduction of Young's modulus by $\Delta\Omega/\Omega_0 = \Delta Y/2Y_0$, where Ω_0 corresponds to the static Young's modulus Y_0 since $\Delta\Omega$ and ΔY are small compared to Ω_0 and Y_0 . Solving equation 3.7 for a solution $R_A e^{-i\omega t}$ yields for the absolute value of the response

$$|R_A| = \frac{|A_r|}{\sqrt{(\omega^2 - \Omega^2)^2 + 4\gamma^2\omega^2}}. \quad (3.8)$$

We numerically simulate the measurement protocol (see Appendix A) used in the experiments [e.g. 5, 30]. The recorded quantity for the response is the acceleration amplitude $\omega^2 R_A L_0$.

3.4 Numerical simulations

We show in this section with our thermodynamics-based model that we can simulate important features (mentioned in section 3.1) of resonance curves produced in the laboratory [2, 5, 60, 87].

3.4.1 Recovery of resonant frequency

We simulate slow dynamics after the dynamic deformation ends. Figure 3.4 shows the recovery of the resonant frequency after long-time deformation (10^6 time steps or 5 ms) as a function of the logarithm of time. We use different amplitudes at the same driving frequency

3900 Hz. The log-time recovery produced by our model is (almost) identical to the laboratory measurements in Fig. 5 of TenCate et al. [87] that shows the observed logarithmic recovery of the resonant frequency.

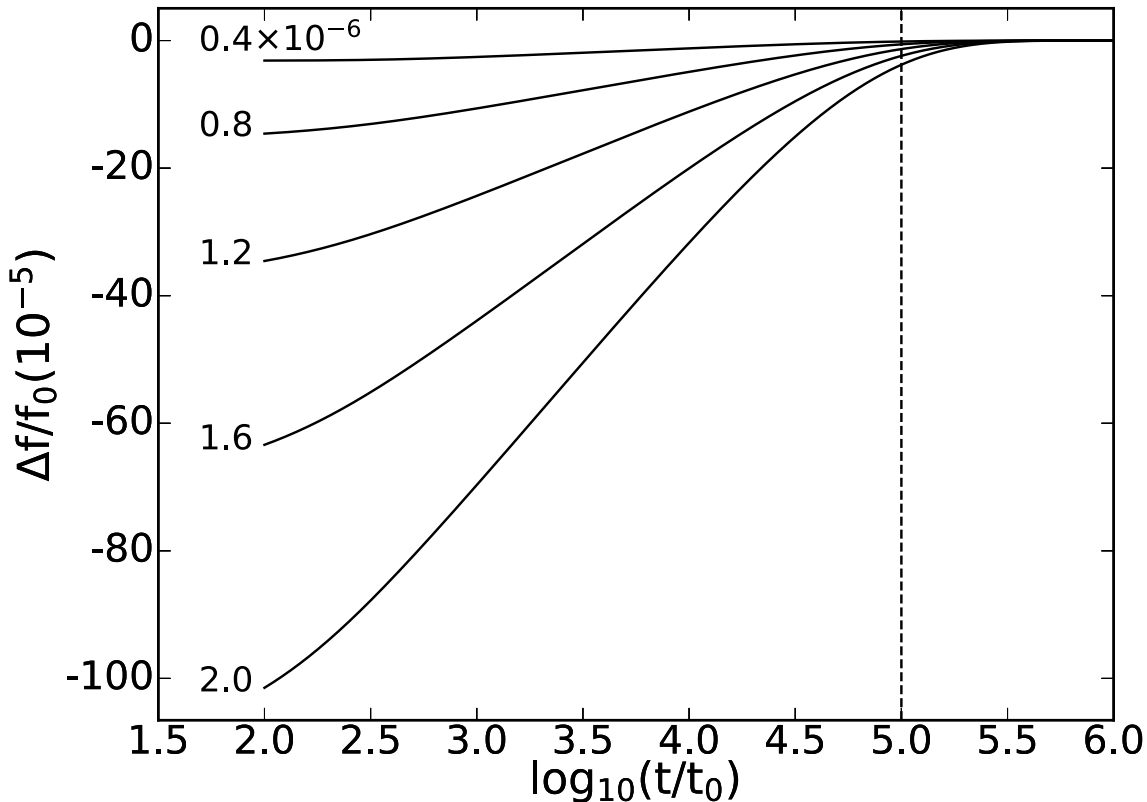


Figure 3.4: Recovery of the resonant frequency after dynamic deformations with different strain amplitudes, where $t_0 = 5 \mu\text{s}$ is time step in the numerical model. The vertical dashed line denotes τ_{max} .

To illustrate the effect of the superimposed time scales, we can also apply the model without integrating over the barrier energy and show an example for a single barrier energy, $E_b = 0.38 \text{ eV}$, in Figure 3.5. In this case, the recovery does not vary with the logarithm of time. This highlights the importance of the summation of multiscale relaxation processes for the log-time recovery. Snieder et al. [86] propose τ_{max} , a metric to characterize the maximum relaxation time among multiscale relaxation processes:

$$\frac{1}{\tau_{max}} = \left(\frac{1}{\tau_o} + \frac{1}{\tau_c} \right)_{E_b=E_{bmax}}, \quad (3.9)$$

where τ_o and τ_c are given in equation 3.1. We denote τ_{max} in Figure 3.4 with a dashed line, which agrees well with the time needed for the relaxation.

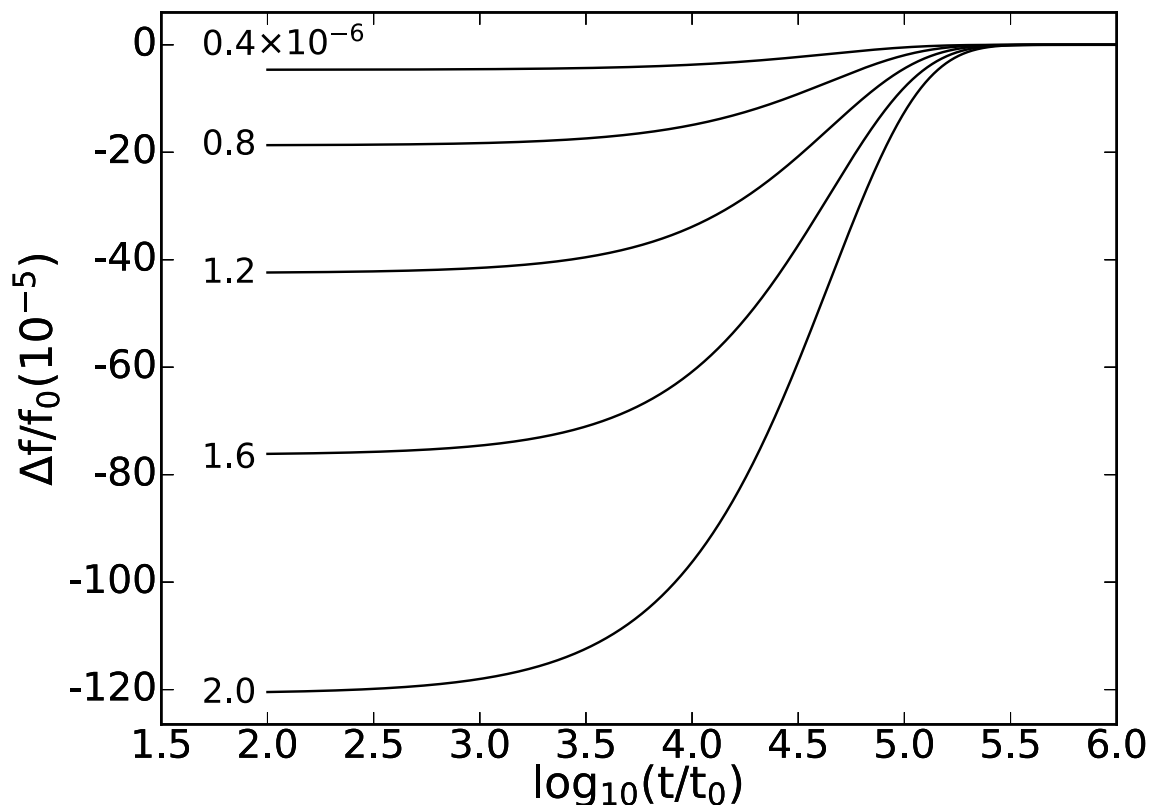


Figure 3.5: Recovery of the resonant frequency for a single barrier energy.

3.4.2 Asymmetric resonance curves

We show the response amplitude against the driving frequency in Figure 3.6 for both the upward and downward sweeps and different driving amplitudes. We record the response as the acceleration given by $\omega^2 R_A L_0$ and change the driving frequency by $\Delta f = 1$ Hz after a time interval $\Delta t = 5$ ms ($0.01\tau_{max}$); the frequency sweep covers the resonant frequency $f_0 = 3900$ Hz of the unperturbed sample. Here we define Δt as the sweep time interval, which reflects the sweep rate of the driving frequency. One can regard Δt as the time duration between two consecutive driving frequencies. The total sweep time of the driving frequency results from the multiplication of Δt and the number of sampled driving frequencies.

Figure 3.6 shows that with increasing driving amplitude A_r , the peak value of the resonance curve increases and the resonant frequency decreases. An increase in the driving amplitude A_r gives an increase in the response amplitude (see equation 3.8) and creates more open fractures than a low driving amplitude; the associated softening reduces the resonant frequency. The difference between the upward and downward resonance curves is reproduced by the model in all details and is most pronounced to the left of the resonant peak. Figure 3.6 can be qualitatively compared to the laboratory measurements in Ten Cate and Shankland [60], especially for the asymmetric resonance curves when the driving amplitude is large.

The asymmetry in the direction of the driving frequency can be explained as follows. Suppose one sweeps downward in frequency. When the frequency is higher than the resonant frequency ($\omega > \Omega$) and one approaches the resonant peak, the deformation increases and the sample softens. This reduces the resonant frequency Ω , hence the resonant peak “moves away” from the current driving frequency ω , and as a result the response curve flattens to the right of the peak. But when the driving frequency is reduced further, the driving frequency ω is less than the resonant frequency Ω . Now the deformation decreases as the driving frequency is reduced further, which makes the sample stiffer. This increases the resonant frequency Ω , which moves the response peak towards higher frequency, away from the current frequency, which further decreases the deformation. Thus, this increasing resonant frequency leads to a steepening of the resonance curve to the left of the peak. A similar reasoning applies when one increases the driving frequency ω starting at values less than the resonant frequency Ω . Approaching the resonant peak from the left, the peak of the curve comes closer when the amplitude increases; consequently it steepens on the left and it flattens on the right. The asymmetry of the resonance curve thus follows from the nonlinearity that causes the sample to soften as the deformation increases. In our model, the nonlinearity is implicit in the used parametrization of the fracture behavior and its imprint on Young’s modulus, but a nonlinear model based on anharmonicities gives the same shape of resonance curves

[131]. In other words, softening (nonlinearity) steepens the left part of the resonance curve and flattens the right part, which is equivalent to the mechanism that the feedback of the nonlinearity on deformation causes the shift of the resonant frequency.

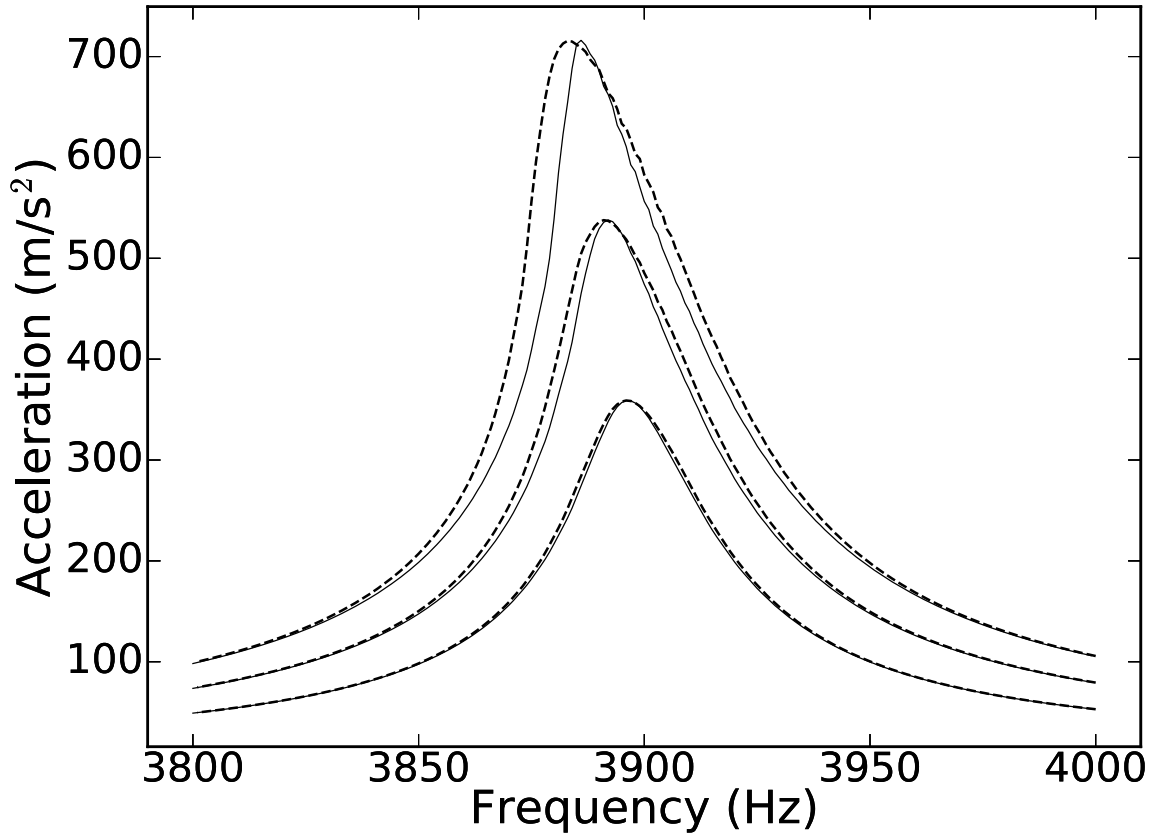


Figure 3.6: Resonance curves for the upward (solid lines) and downward (dashed lines) sweeps with different driving amplitudes $A_r = 8.8, 13.2, 17.6/s^2$.

We can apply the model without integrating over the barrier energy and show an example for a single barrier energy $E_b = 0.30$ eV. Figure 3.7 shows the resonance curves for this case. The resonance curves in Figure 3.7 have (almost) the same shapes as those in Figure 3.6. We have shown that the multiscale relaxation mechanism is essential to the log-time recovery in section 3.4.1. However, comparing Figure 3.6 and Figure 3.7, we conclude that the multiscale relaxation mechanism is not essential for the shape of resonance curves.

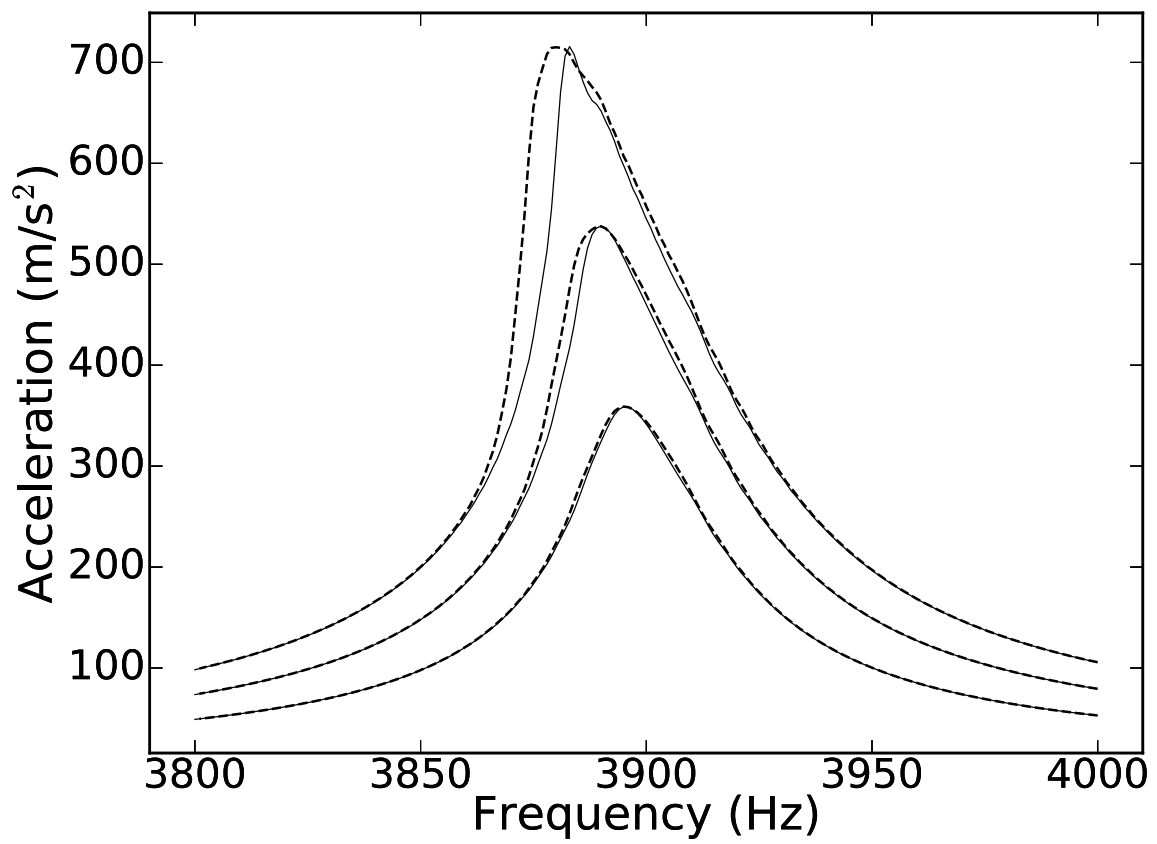


Figure 3.7: Resonance curves as in Figure 3.6, but for a single barrier energy.

3.4.3 Up-down difference and slow dynamics

Ten Cate and Shankland [60] speculate that for a slow sweep rate, i.e., large Δt of the driving frequency, the up-down difference disappears. For a slow sweep rate, the activation is effectively stationary in time, and one would expect that the sample reaches an equilibrium that is the same, regardless of whether one sweeps up or down. TenCate [2] confirms the speculation that the up-down difference can vanish at a slow sweep rate in the laboratory measurements.

Figure 3.8 shows the up-down difference at different sweep rates with a driving amplitude $A_r = 17.6/\text{s}^2$ corresponding to the uppermost pairs of the resonance curves in Figure 3.6. The simulation in this figure confirms the speculation in ref. [60] and echoes the laboratory measurements [2] in which a slow sweep rate eliminates the up-down difference [see Figure 3.8(c)]. We compare the sweep rate (sweep time interval Δt) to the maximum relaxation time τ_{max} in our model. For the used sweep frequency interval $\Delta f = 1$ Hz, we refer the fast sweep to the case $\Delta t \ll \tau_{max}$ while the slow sweep means $\Delta t \gg \tau_{max}$. We attribute the up-down difference to slow dynamics when the sweep is fast [e.g., Figure 3.8(a)]. That a driving frequency gives different response amplitudes for different sweep directions reflects that the fracture system memorizes the past deformation (slow dynamics). However, as the sweep rate decreases, this “memory effect” disappears and the driving force conditions the sample to the same response amplitude regardless of the sweep direction.

3.4.4 Cliff in resonance curves

We further increase the nonlinearity in the simulation by increasing the value of the fracture modulus C_0 . Figure 3.9 shows the dependence of the up-down difference on the sweep rate. Comparison of Figure 3.8 and Figure 3.9 indicates that nonlinearity enhances the up-down difference. Strong nonlinearity and a slow sweep rate can produce a “cliff” (vertical segment) in resonance curves [e.g., Figure 3.9(c)]. The cliff represents a large abrupt change of the response amplitude when the driving frequency is changed. The up-

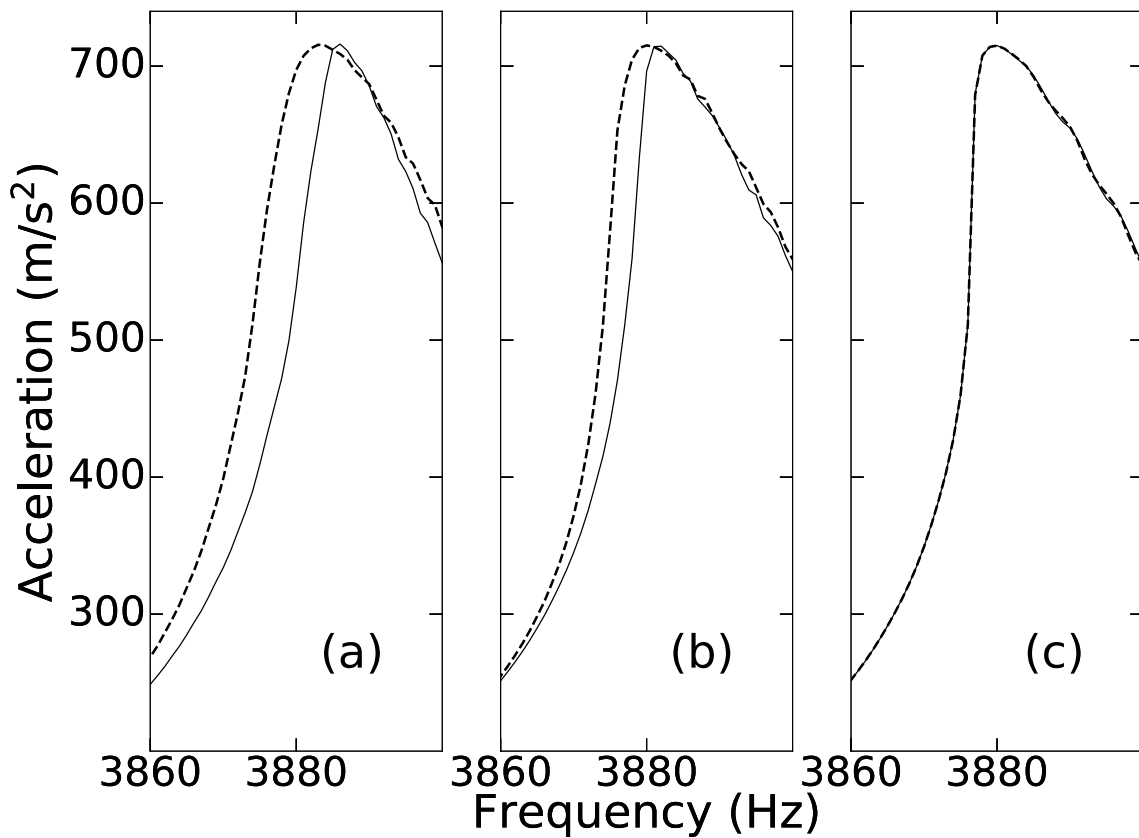


Figure 3.8: Sweep-rate dependence of the up-down difference of the resonance curves at the left side of the resonant peak. Solid lines denote the upward sweep, while dashed lines denote the downward sweep. The sweep time interval between sampled driving frequencies is (a) 5 ms ($0.01\tau_{max}$), (b) 500 ms (τ_{max}), and (c) 5 s ($10\tau_{max}$).

down difference right at the cliff does not disappear for slow sweep rates, even though it vanishes away from the cliff [Figure 3.9(c)]. This appears very similar to the measurements by Johnson et al. [5], who show resonance measurements in Lavoux sandstone that exhibit a cliff with a pronounced difference between upward and downward sweeps.

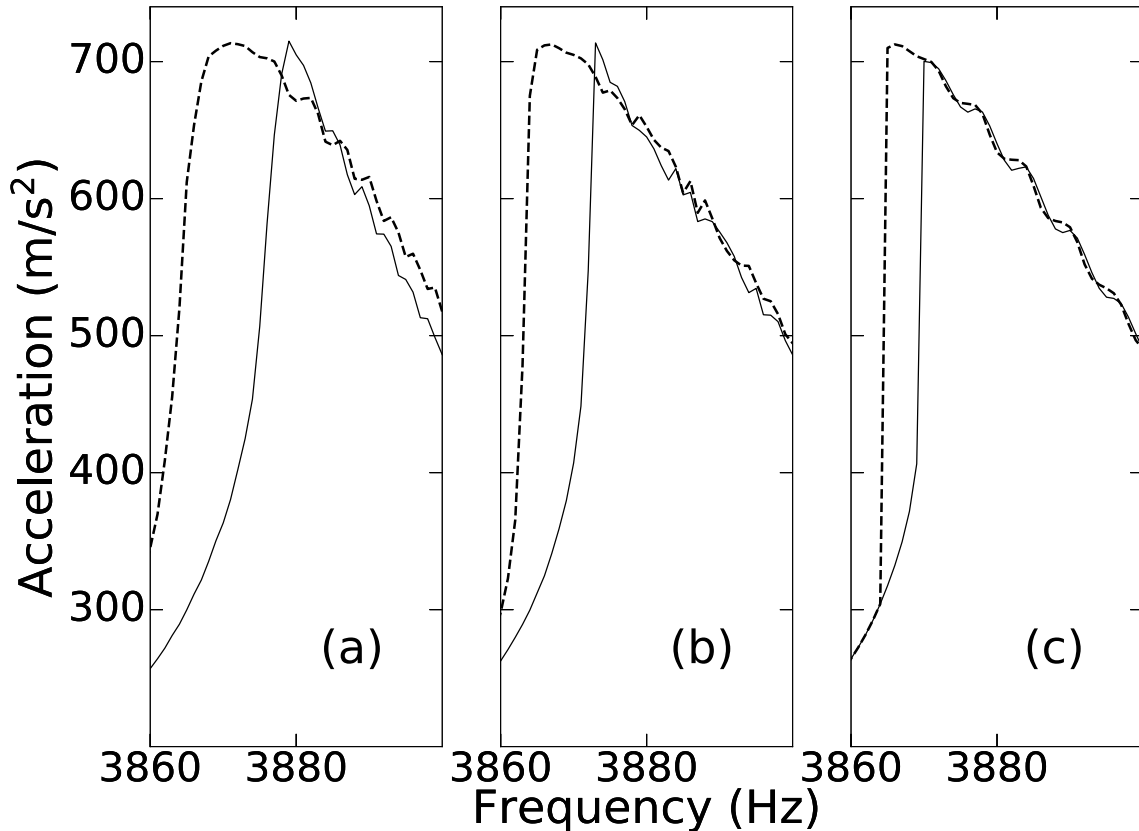


Figure 3.9: Sweep rate dependence of the up-down difference. The fracture modulus is $C_0 = 3.088$ GPa, with stronger nonlinearity than that in Figure 3.8. The sweep-time interval between sampled driving frequencies is (a) 5 ms ($0.01\tau_{max}$), (b) 500 ms (τ_{max}), and (c) 5 s ($10\tau_{max}$), following Figure 3.8.

To explain the up-down difference that is most pronounced in Figure 3.9(c) at the cliff even when the sweep rate is slow, we refer to the bifurcation that originates from the solution of the Duffing equation for nonlinear systems [119, 120, 147]. We consider the steady-state solution of our model without incorporating the temporal evolution of the fracture system, i.e., the fraction of open fractures N_o in stable equilibrium where N_o represents the damage of the sample. We then solve for the damage N_o from different initial damage N_{oi}

at each fixed frequency (for more details, see Appendix B). Figure 3.10(a) and (b) show the stable equilibrium damage state for every frequency (i.e., dashed black and solid green curves) for two different driving amplitudes; the colors indicate that for each frequency and initial value N_{oi} the final fraction of open fractures N_o to which the system converges (see Appendix B). Figure 3.10(a) shows the situation for moderate nonlinearity caused by a driving amplitude of $0.6/s^2$. In this case the stable equilibrium damage state N_o is determined only by frequency. Independently of the initial damage state, the system converges to the same stable equilibrium indicated by the overlapping lines. The situation is different for stronger nonlinearity, as shown in Figure 3.10(b), where there is a range of frequencies in which the stable equilibrium damage state to which the system converges also depends on the initial damage state. Figure 3.10(b) shows a bifurcation of the stable equilibrium solution N_o ; for a range of driving frequencies around the cliff of the resonance curve, there are two possible solutions of N_o for the same driving frequency. When one *reduces* the driving frequency ω at point d in Figure 3.10(b), the system can only jump to point a . This leads to the vertical slope of the dashed line in Figure 3.9(c). A similar reasoning applies to sweeping upward in frequency. When sweeping upward, one arrives at point b of the resonance curve. When sweeping further upward in frequency, the system jumps to point c on the resonance curve, and this jump results in a vertical segment of the resonance curve at a higher frequency.

The steady-state solution can be indicative of the simulated resonance experiment. We argued above that the nonlinear material response causes the response curve to steepen to the left of the resonant peak. The feedback of the deformation on the response can be so strong that the resonance curve folds over on itself, as shown in Figure 3.10(b); this folding happens when the nonlinearity caused by a large driving force is sufficiently strong. When the nonlinearity is further increased, a bifurcation occurs [Figure 3.10(b)]. Thus, this phenomenon of vertical jumps in the resonance curves corresponds to a bifurcation caused by the nonlinearity in the underlying equations with time evolution. A prototype of this bifurcation is described for the Duffing equation [120], which can be solved using

the harmonic balance method [119]. The stable equilibrium solution is a simplified solution corresponding to the approximation that one can omit the details of the averaged fracture system during an oscillation cycle. Note that along segment \overline{db} in Figure 3.10(b), there is an abrupt change in color. For initial values just above the segment the damage will increase and the system converges to a higher equilibrium value along segment \overline{cd} while for initial values below segment \overline{db} the system relaxes to a lower equilibrium value along segment \overline{ab} . This means that just as with the Duffing equation [120], segment \overline{db} corresponds to unstable equilibrium values.

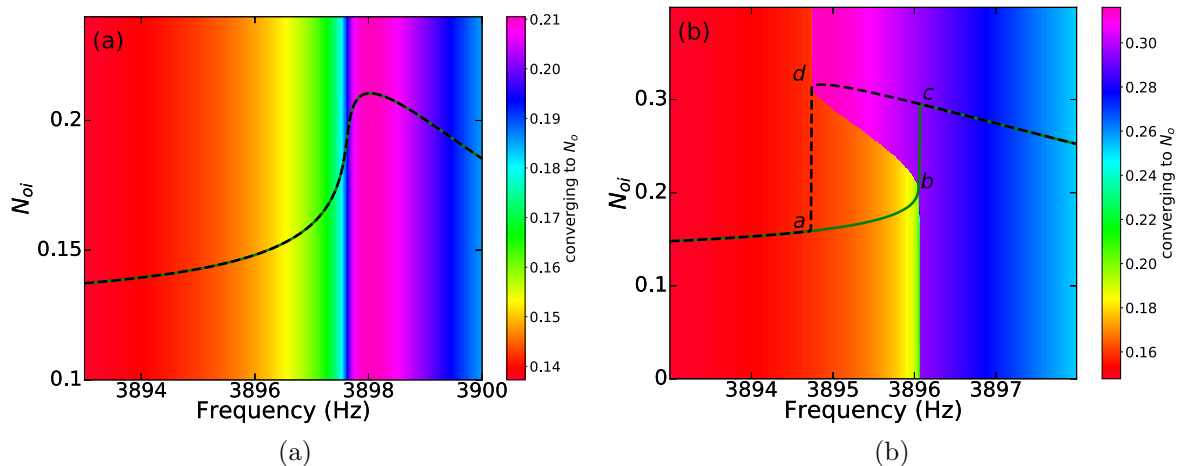


Figure 3.10: Steady-state solution of our model with (a) $A_r = 0.6/s^2$ and (b) $A_r = 1.0/s^2$. The color scale indicates for each frequency and original value N_{oi} the equilibrium fraction N_o to which the solution converges.

The stable equilibrium solution further indicates that the key factor for the system to lock in to a solution depends on the current value of N_o when the driving frequency is changed. Changing the sweep direction results in a different initial damage with which a certain frequency is approached, and in the case of strong nonlinearity, a different sweep direction might lead to different stable equilibrium to which the system converges. However, the bifurcation is only present when the nonlinearity is sufficiently strong to cause a vertical cliff. The nonlinearity (bifurcation) can originate from both (a) large driving amplitudes and (b) material properties (e.g., the opening and closing of fractures with strain, and the

influence of fractures on the modulus).

An alternative to the stable equilibrium solution that is indicative of the “true” oscillation is to directly simulate the oscillation with an initial condition N_{oi} for all the energy barriers and a fixed driving frequency. Figure 3.11 shows the stable averaged damage N_o over the last cycle of the oscillations; this graph again echoes the implementation of the stable equilibrium solution and the presence of the bifurcation when the nonlinearity in the system is strong. However, the implementation of a “true” solution is much more computationally expensive than that of the stable equilibrium solution.

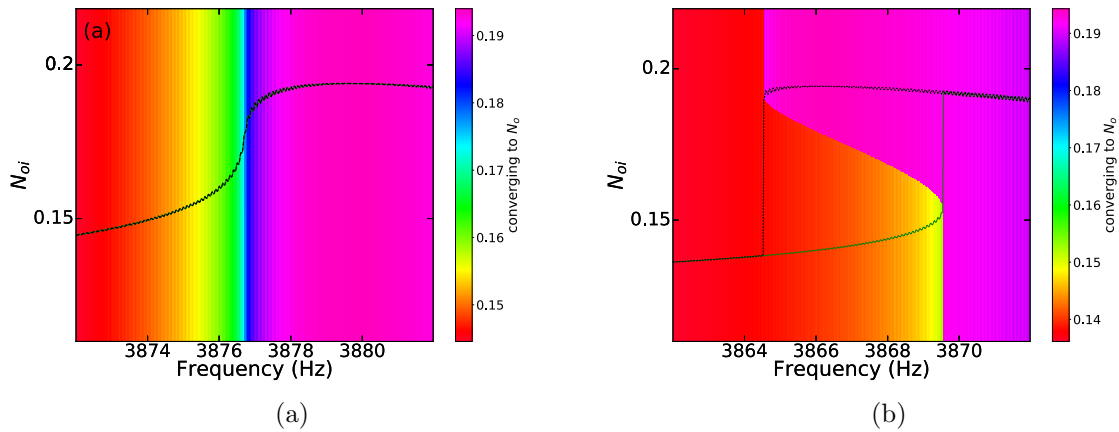


Figure 3.11: Solution of the thermodynamics-based oscillation model with (a) $C_0 = 1.853$ GPa and (b) $C_0 = 3.088$ GPa. The color scale indicates for each frequency and original value N_{oi} the equilibrium fraction N_o to which the true solution converges.

Since different nonlinear models to lowest order reduce to a cubic term (Duffing equation) in the equation of motion, this catastrophic behavior (vertical cliff with a strong response to a tiny change in frequency) is displayed by different models for nonlinear rock physics [5, 93, 131]. However, these models do not explicitly explain the cliff in the resonance curve by the bifurcation. In contrast to earlier work [83, 127], our model is significantly simpler and is based on a relation between the (micro)fracture energy and strain; this relation is another form of thermodynamics-based parametrization. Vakhnenko et al. [83] relate the up-down difference to the end-point memory (slow dynamics) but do not show this catastrophic

behavior (cliff) in resonance curves. Regarding slow dynamics, Figure 3.4 gives a better straight-line region than Fig.11 in Vakhnenko et al. [83]. Lyakhovsky et al. [127] show the cliff in the simulated resonance curve but do not relate the cliff with the bifurcation. Our theory qualitatively reproduces both the slow dynamics and bifurcation observed in laboratory experiments [5, 60].

3.5 Discussion

The resonance curves in Figure 3.6 show two conspicuous features: they are asymmetric, and they are different depending on whether one sweeps upward or downward in frequency (up-down difference). We explain the asymmetry of resonance curves by softening (nonlinearity) and the up-down difference by both the slow dynamics and bifurcation. It is the nonlinearity that produces the bifurcation. The bifurcation occurs only when the nonlinearity is sufficiently strong. The bifurcation causes a cliff in resonance curves [119]; otherwise, in the absence of a bifurcation (for weaker nonlinearity) slow dynamics dominates the up-down difference, and this difference disappears for slow sweep rates. The reports of the coincidence of the resonance curves [e.g., 2, 60] are for cases where slow dynamics dominates the up-down difference. The nonlinearity of rocks in these experiments [2, 60] is not strong enough to cause a bifurcation. Johnson et al. [5] show the experimental resonance curves with cliff segments that result from the strong nonlinearity in rocks. Our model also reproduces this cliff behavior (Figure 3.9) when the nonlinearity is significantly strong. Even stronger nonlinearity causes the system to display chaotic behavior [148] where the response amplitude jumps up and down.

In summary, up-down resonance curves can be coincident at a slow sweep rate, but only if the nonlinearity is weak. When the cliff is observed in resonance curves, our model predicts that no matter how slowly one sweeps the driving frequency, the up-down resonance curves cannot be coincident because of the presence of a bifurcation. Figure 3.9 confirms our conclusion that the up-down difference for slow sweep rates does not vanish when the system is bifurcated.

Slow dynamics is caused by the nonlinear rock properties. Such nonlinearity can be caused by (a) classical anharmonicity from Landau’s theory [20] or (b) nonclassical anharmonicity from Hertz-Mindlin contacts [21]. In addition, slow dynamics depends on a dependence of the nonlinearity on past deformation. When the sweep rate is not slow compared to the minimum relaxation time [Figure 3.9(a)], the current response depends on the past deformation. This effectively smears out the cliff in the resonance curve.

3.6 Conclusion

A simple thermodynamics-based model can explain observed resonance curves. But this model does not provide a unique description of the microscopic behavior of fractures as in studies for a physical origin of rate and state friction [149, 150]. The theory can be treated as a phenomenological parametrization of the imprint of damage on crack properties. We prescribe the fracture energy in Figure 3.3 in a heuristic fashion for compressive waves. In real rocks, shear motion occurs near fractures, even when the sample is under a compressive uniaxial load. In addition, the fracture behavior likely depends on the strain rate $\dot{\epsilon}$ as well [69, 146]. Fractures have a range of orientations with respect to the principal stress components, and the fracture behavior depends on a range of physical and chemical processes that are influenced by the presence of fluids (notably, water). Our model should be seen as a thermodynamics-based parametrization of nonlinear fracture behavior. But this simplified model can reproduce the experimental features of the observed resonance curves.

Our model offers a unified interpretation of both the nonlinearity and slow dynamics in resonance experiments. When the nonlinearity of the vibration system is weak, the up-down difference is indicative of slow dynamics. Thus, the up-down difference can be used to study the slow dynamics. When the nonlinearity is strong, the up-down difference depends on both the bifurcation and slow dynamics. In this case the up-down difference does not vanish around the cliff, no matter how slowly one sweeps the driving frequency in the resonance experiments. We suggest that one test the presence of the bifurcation in an experiment that is performed at a constant frequency within the relevant frequency range. When starting

with a fully relaxed sample, the resulting stable equilibrium will be on the lower branch of the bifurcation. When starting with a sample that has been damaged by a sustained large driving amplitude, the sample will reach a stable equilibrium at the upper branch of the bifurcation.

3.7 Acknowledgments

We thank anonymous reviewers for their positive and constructive comments. This work was supported by the Consortium Project on Seismic Inverse Methods for Complex Structures at the Colorado School of Mines.

CHAPTER 4

OUTLOOK

Chapters 2 and 3 describe different types of nonlinear elasticity. Although a difference exists between mathematical nonlinear oscillation systems (e.g., Duffing equation) and physical resonance experiments conducted in the laboratory, the analysis of the nonlinear elasticity in the Duffing equation (Chapters 2) helps interpret the simulations of laboratory resonance experiments (Chapter 3). The EOS can have a variety of expressions regarding phenomenological or semi-phenomenological models. Since these nonlinear models to their lowest order reduce to a cubic anharmonic term that accounts for the nonlinearity in the Duffing equation, these models can produce a bifurcation when the nonlinearity of oscillation systems is strong. In this case, a cliff is present in the resonance curve. The initial condition of the deformation strain (see section 2.1) is indicative of the initial damage N_{oi} (see Figure 3.10 and Figure 3.11) in the simulated resonance experiments (see section 3.4.4). Since the strain determines softening, the initial condition of the strain is equivalent to the initial elastic state of a sample. The initial damage N_{oi} correlates with the initial elastic state, mentioned in physical resonance experiments; hence, the mathematical concept, the initial strain defined in Chapter 2, can be comparable to the initial damage that is defined in a physical sense (Chapter 3). In summary, this thesis provides a unified interpretation of the observed nonlinear elasticity measured by resonance experiments.

4.1 Limitations

The thermodynamics-based model used in Chapter 3 is based on the Arrhenius law [86, 144] and acts as an implicit nonlinear EOS. I apply the measurement protocol to simulating the resonance experiments; the protocol measures the average damage that is calculated from the variable damage (N_o) over the last cycle of the oscillation. However, the simple thermodynamics-based model may not be effective in the simulation of all other nonlinear

features introduced in Chapter 1. In this thesis, I do not include the simulations of stress-strain or elasticity-strain hysteresis [124], the observed resonant frequency shift against the strain amplitude [63], and the combination frequency in nonlinear wave modulation [71] using the thermodynamics-based model used in Chapter 3.

The “triple butterfly” observed in the hysteresis loop produced by DAET [30, 34] challenges the existing hysteretic simulations such as those using the PM-based model [93]. Such the triple butterfly (see Figure 1.5) may result from both the attenuation (i.e., damped oscillator) and nonlinear mesoscopic elasticity. For this aspect of the nonlinear EOS, the thermodynamics-based model used in Chapter 3 may need to be extended to include the strain rate $\dot{\epsilon}$ for attenuation as well as shear motions for a complete description of dynamic features (e.g., open and close) in fractures [146].

The thermodynamics-based model provides a limited physical description for a simple simulation of resonance experiments. For example, my model does not provide a detailed upscaling method to connect the microscopic or mesoscopic fracture density (concentration) to macroscopic elastic constants (e.g., Young modulus). I assume a simple linear correlation between Young’s modulus and fracture density; however, a correlation between elastic moduli and fractures could further account for complicated issues such as fracture orientations, fracture surface energy, and distribution of fractures in granular solids. One should take a nonlinear stiffness tensor into account when anisotropy is also induced by fractures [151, 152]. Figure 3.5 illustrates the contribution of the multiscale relaxation scheme to slow dynamics with log-time recovery. However, the underlying reason why *log-time* recovery is a universal feature observed in rocks remains an open question; no physical explanation exists for the even distribution of barrier energy. Li et al. [90] explain the log-time recovery of frictional contacts that statically adhere to each other; the recovery involves re-establishing bonds/links between contact surfaces. The observation of this chemical-physical process provides a physical interpretation of the observed log-time recovery in granular solids including rocks and concrete. However, one still needs a physical understanding of upscaling, which

should be a universal scheme for all nonlinear elastic materials.

As far as I know, no unified physical model presently exists to explain the observed nonlinear elasticity. Some EOSs are built based on microcontact models [21, 89] but assume a contact shape/geometry, which cannot universally apply to various soft elements including pores, microcontacts, and microfractures in rocks and concrete. Also, a difficulty exists for numerical simulations when one incorporates too many physics details with a significant increase in the number of parameters [e.g., 83, 89]. For example, reproducing slow dynamics with the *log-time* recovery is difficult if one does not assume a phenomenological distribution of the energy or sizes of fractures. A parametrization with a massive amount of variables complicates the simulation and one will find it difficult to reproduce the nonlinear features observed in laboratory measurements. Numerical simulations aim to reproduce observed nonlinear features. Consequently, an increase in the complexity of the parametrization results in the “curse of dimensionality” [see ref. 153] where one needs to undergo a complicated process of choosing reasonable values for the parameters. In other words, the models mentioned in section 1.2 can only be phenomenological or semi-phenomenological to achieve a trade-off between physical descriptions in models and simulated results that explain laboratory measurements. Thus I propose a short-cut in Chapter 3 to maintain a simple thermodynamics-based model.

Most experiments measure the nonlinear elasticity of dry samples (e.g., rocks and concrete) at room temperature [e.g., 30]; dry samples commonly refer to samples with water saturation at atmospheric pressure. Zinszner et al. [16] conduct an experiment that includes the effect of pressure and water saturation on nonlinear elasticity. The interaction between the pore fluid and soft elements in granular solids complicates the observed nonlinear features [154]. Van Den Abeele et al. [155] qualitatively explain the increase and decrease in the softening effect using the intergranular moisture-induced microforces that form capillary bridges [156]. This relationship can be complicated, depending on rock types. An increase in confining pressure weakens nonlinear elasticity due to the reduction of soft elements in

granular solids. Regarding temperature, Zaitsev et al. [142] show an increase in nonlinear elasticity when increasing the temperature of a sample. Models cannot easily be built to explain these observed lithology-dependent features that are related to factors other than the amplitude of the pump waves. Quantitative models incorporated with factors such as temperature, water saturation, and pressure could be promising future work in nonlinear acoustics.

4.2 Future work in geophysics

Future laboratory experiments could confirm the bifurcation that is present in the simulated resonance curves (section 3.6). One can fix the driving frequency and measure the time-varying response amplitude with two different initial conditions; one involves a fully relaxed sample, and the other a fully excited sample, which has been conditioned using a strong driving stress field for enough time to reach an equilibrium elastic state. For the fully conditioned sample, one needs to condition the sample with a large driving amplitude and then conduct the resonance experiment using a smaller driving amplitude, which is the same amplitude used for the fully relaxed sample.

A similar experiment has been conducted in ref. [60], which shows the temporal variation of the deformation amplitude at a fixed driving frequency when the sweep of the driving frequency stops. However for a newly-designed experiment, one needs to apply a large driving amplitude to the sample to create strong nonlinearity in the resonance system. One technique that can identify the “strong nonlinearity” involves observing the presence of a bifurcation, which results in a cliff in resonance curves.

In the future experiment, one could observe two stable elastic states that correspond to oscillations with different initial damages (conditions). With an even stronger nonlinearity, the measurement could show the chaotic jump-up-and-down of the response amplitudes in resonance curves, as shown in Figure 4.1 where water-saturated chalk has unusual instability on its resonance curves.

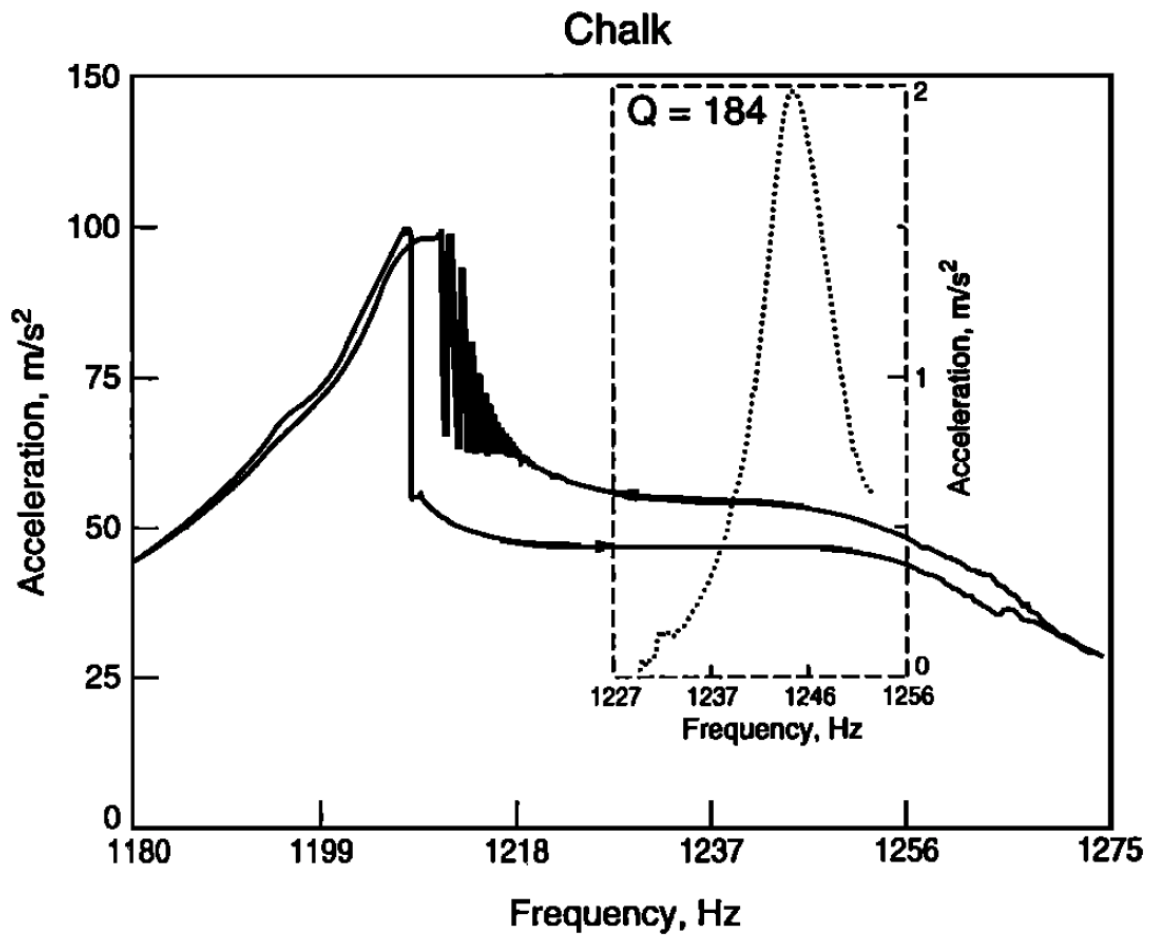


Figure 4.1: Resonance curves for upward and downward sweeps for partially saturated chalk. The inset shows a low-drive resonance curve where unusual instability does not exist. The graph is adapted from Johnson et al. [5].

Nonlinear elasticity is observable in field measurements of seismic velocity, especially in the shallow Earth that contains unconsolidated soils; this lithology is free of significant confining pressure given by the overlying strata. Regarding potential applications in geophysics, my thesis could further contribute to two aspects of exploration geophysics. Chaves and Schwartz [117] observe a transient velocity change at a depth below 5 km in a subduction zone; the velocity change is related to the presence of pressurized pore fluids, which has also been proposed for volcanoes [157]. Such an observation indicates a possible application of nonlinear acoustic imaging on oil and gas reservoirs; nonlinear elasticity has been observed in oil and gas reservoirs [158].

Multi-level cross-well active source monitoring [102, 159–161] could potentially help observe nonlinear features (e.g., combination frequency in wave modulation) in reservoirs using controlled active sources. Although rocks impose significant confining pressure that suppresses the nonlinear elasticity in a reservoir, the pore pressure induced by the presence of oil and gas in the reservoir increases the nonlinear elasticity [16]. Thus, the observed nonlinear features could act as a monitoring tool for the stress change in the reservoir due to the extraction of oil and gas.

The technique used to monitor reservoirs could apply to monitoring the stress change at fault zones [162]. The stress change induces the change of the fracture system and further correlates with the nonlinear elasticity in the reservoir. Some numerical models have explored the effect of the stress change on seismic imaging using a model based on a three-dimensional classical nonlinear EOS, i.e., stiffness tensor [163–165]. I consider nonlinear elasticity as promising attributes in reservoir surveillance, which can be applied to unconventional oil and gas explorations as well as the development of enhanced geothermal systems. The recovery of fractures/contacts in nonlinear elastic materials could be comparable to fracture healing after hydraulic fracturing. The healing of stress-induced fractures harms the productivity of unconventional oil and gas reservoirs and, hence, is of interest to the oil industry [166, 167]. The fracture theory developed for slow dynamics could also be extended to fracture healing

in reservoirs since both healing processes occur at a nanoscale [168].

REFERENCES CITED

- [1] G. Renaud, J. Rivière, P.-Y. Le Bas, and P. A. Johnson. Hysteretic nonlinear elasticity of Berea sandstone at low-vibrational strain revealed by dynamic acousto-elastic testing. *Geophysical Research Letters*, 40(4):715–719, 2013.
- [2] J. A. TenCate. Slow dynamics of earth materials: An experimental overview. *Pure and Applied Geophysics*, 168(12):2211–2219, 2011.
- [3] M. Meo, U. Polimeno, and G. Zumpano. Detecting Damage in Composite Material Using Nonlinear Elastic Wave Spectroscopy Methods. *Applied Composite Materials*, 15(3):115–126, 2008.
- [4] M. Gassenmeier, C. Sens-Schönfelder, T. Eulendorf, M. Bartsch, P. Victor, F. Tilmann, and M. Korn. Field observations of seismic velocity changes caused by shaking-induced damage and healing due to mesoscopic nonlinearity. *Geophysical Journal International*, 204(3):1490–1502, 2016.
- [5] P. A. Johnson, B. Zinszner, and P. N. J. Rasolofosaon. Resonance and elastic nonlinear phenomena in rock. *Journal of Geophysical Research: Solid Earth*, 101(B5):11553–11564, 1996.
- [6] D. J. Holcomb. Memory, relaxation, and microfracturing in dilatant rock. *Journal of Geophysical Research: Solid Earth*, 86(B7):6235–6248, 1981.
- [7] A. J. M. Spencer. *Continuum Mechanics*. Dover books on physics. Dover Publications, 2004.
- [8] J. Pujol. *Elastic Wave Propagation and Generation in Seismology*. Cambridge University Press, 2003.
- [9] K. Aki and P. G. Richards. *Quantitative Seismology*. Geology (University Science Books).: Seismology. University Science Books, 2002.
- [10] I. D. Tsvankin and E. M. Chesnokov. Plane wave propagation in nonlinear-elastic anisotropic media. *Geophysical Journal International*, 91(2):413–427, 1987.
- [11] M. A. Slawinski. *Waves and Rays in Elastic Continua*. World Scientific, 2010.
- [12] B. L. N. Kennett. *Seismic Wave Propagation in Stratified Media*. Cambridge Monographs on Mechanics. Cambridge University Press, 1985.

- [13] D. Pasqualini, K. Heitmann, J. A. TenCate, S. Habib, D. Higdon, and P. A. Johnson. Nonequilibrium and nonlinear dynamics in Berea and Fontainebleau sandstones: Low-strain regime. *Journal of Geophysical Research: Solid Earth*, 112(1):1–16, 2007.
- [14] L. Ostrovsky and P. A. Johnson. Dynamic nonlinear elasticity in geomaterials. *Nuovo Cimento Rivista Serie*, 24:1–46, 2001.
- [15] L. B. Jr Hilbert, T. K. Hwong, N. G. W. Cook, K. T. Nihei, and L. R. Myer. Effects of Strain Amplitude on the Static and Dynamic Nonlinear Deformation of Berea Sandstone. *The 1st North American Rock Mechanics Symposium*, 1994.
- [16] B. Zinszner, P. A. Johnson, and P. N. J. Rasolofosaon. Influence of change in physical state on elastic nonlinear response in rock: Significance of effective pressure and water saturation. *Journal of Geophysical Research: Solid Earth*, 102(B4):8105–8120, 1997.
- [17] P. A. Johnson and P. N. J. Rasolofosaon. Manifestation of nonlinear elasticity in rock: convincing evidence over large frequency and strain intervals from laboratory studies. *Nonlinear Processes in Geophysics*, 3(2):77–88, 1996.
- [18] K. Ishihara. *Soil Behaviour in Earthquake Geotechnics*. Oxford engineering science series. Clarendon Press, 1996.
- [19] N. H. Sleep and P. Hagin. Nonlinear attenuation and rock damage during strong seismic ground motions. *Geochemistry, Geophysics, Geosystems*, 9(10):Q10015, 2008.
- [20] L. D. Landau, E. M. Lifshitz, A. M. Kosevich, and L. P. Pitaevskii. *Theory of Elasticity*. Course of Theoretical Physics. Elsevier, New York, 1986.
- [21] R. A. Guyer and P. A. Johnson. *Nonlinear Mesoscopic Elasticity: The Complex Behaviour of Rocks, Soil, Concrete*. Wiley, New York, 2009.
- [22] S. Vanaverbeke and K. Van Den Abeele. Two-dimensional modeling of wave propagation in materials with hysteretic nonlinearity. *The Journal of the Acoustical Society of America*, 122(1):58–72, 2007.
- [23] V. Grechka and M. Kachanov. Effective elasticity of fractured rocks: A snapshot of the work in progress. *Geophysics*, 71(6):W45–W58, 2006.
- [24] X. Huang, G. W. Ma, and J. C. Li. Damage Assessment of Reinforced Concrete Structural Elements Subjected to Blast Load. *International Journal of Protective Structures*, 1(1):103–124, 2010.

- [25] Q. A. Vu, V. Garnier, J. F. Chaix, C. Payan, M. Lott, and J. N. Eiras. Concrete cover characterisation using dynamic acousto-elastic testing and Rayleigh waves. *Construction and Building Materials*, 114:87 – 97, 2016.
- [26] C. Payan, V. Garnier, J. Moysan, and P. A. Johnson. Applying nonlinear resonant ultrasound spectroscopy to improving thermal damage assessment in concrete. *The Journal of the Acoustical Society of America*, 121(4):EL125–EL130, 2007.
- [27] K. Van Den Abeele and J. De Visscher. Damage assessment in reinforced concrete using spectral and temporal nonlinear vibration techniques. *Cement and Concrete Research*, 30(9):1453 – 1464, 2000.
- [28] M. Brigante and M. A. Sumbatyan. Acoustic methods for the nondestructive testing of concrete: A review of foreign publications in the experimental field. *Russian Journal of Nondestructive Testing*, 49(2):100–111, 2013.
- [29] S. Hauptert, G. Renaud, J. Rivère, M. Talmant, P. A. Johnson, and P. Laugier. High-accuracy acoustic detection of nonclassical component of material nonlinearity. *The Journal of the Acoustical Society of America*, 130(5):2654–2661, 2011.
- [30] J. Rivière, P. Shokouhi, R. A. Guyer, and P. A. Johnson. A set of measures for the systematic classification of the nonlinear elastic behavior of disparate rocks. *Journal of Geophysical Research: Solid Earth*, 120(3):1587–1604, 2015.
- [31] M. Scalerandi, A. S. Gliozzi, C. L. E. Bruno, and P. Antonaci. Nonequilibrium phenomena in damaged media and their effects on the elastic properties. *The Journal of the Acoustical Society of America*, 131(6):4304–4315, 2012.
- [32] K. Nakagawa and K. Soga. Nonlinear Cyclic Stress-Strain Relations of Soils. *Proceedings: Third International Conference on Recent Advances in Geotechnical Earthquake Engineering and Soil Dynamics*, 1:1–5, 1995.
- [33] M. Lott, M. C. Remillieux, V. Garnier, P.-Y. Le Bas, T. J. Ulrich, and C. Payan. Nonlinear elasticity in rocks: A comprehensive three-dimensional description. *Physical Review Materials*, 1(2):023603, 2017.
- [34] G. Renaud, P.-Y. Le Bas, and P. A. Johnson. Revealing highly complex elastic nonlinear (anelastic) behavior of Earth materials applying a new probe: Dynamic acousto-elastic testing. *Journal of Geophysical Research: Solid Earth*, 117(B6):B06202, 2012.
- [35] J. Rivière, G. Renaud, R. A. Guyer, and P. A. Johnson. Pump and probe waves in dynamic acousto-elasticity: Comprehensive description and comparison with nonlinear elastic theories. *Journal of Applied Physics*, 114(5):054905, 2013.

- [36] G. Renaud, S. Callé, and M. Defontaine. Remote dynamic acoustoelastic testing: Elastic and dissipative acoustic nonlinearities measured under hydrostatic tension and compression. *Applied Physics Letters*, 94(1):011905, 2009.
- [37] G. Renaud, S. Callé, and M. Defontaine. Dynamic acoustoelastic testing of weakly pre-loaded unconsolidated water-saturated glass beads. *The Journal of the Acoustical Society of America*, 128(6):3344–3354, 2010.
- [38] J. N. Eiras, Q. A. Vu, M. Lott, J. Payá, V. Garnier, and C. Payan. Dynamic acousto-elastic test using continuous probe wave and transient vibration to investigate material nonlinearity. *Ultrasonics*, 69:29–37, 2016.
- [39] C. Pecorari. Modeling the elasto-acoustic hysteretic nonlinearity of dry Berea sandstone. *Wave Motion*, 52:66–80, 2015.
- [40] P. Finkel, A. G. Zhou, S. Basu, O. Yeheskel, and M. W. Barsoum. Direct observation of nonlinear acoustoelastic hysteresis in kinking nonlinear elastic solids. *Applied Physics Letters*, 94(24):1–4, 2009.
- [41] T. Gallot, A. Malcolm, T. L. Szabo, S. Brown, D. Burns, and M. Fehler. Characterizing the nonlinear interaction of S- and P-waves in a rock sample. *Journal of Applied Physics*, 117(3):034902, 2015.
- [42] N. Tremblay, E. LaRose, and V. Rossetto. Probing slow dynamics of consolidated granular multicomposite materials by diffuse acoustic wave spectroscopy. *The Journal of the Acoustical Society of America*, 127:1239–1243, 2010.
- [43] Y. Zhang, V. Tournat, O. Abraham, O. Durand, S. Letourneur, A. Le Duff, and B. Lascoup. Nonlinear mixing of ultrasonic coda waves with lower frequency-swept pump waves for a global detection of defects in multiple scattering media. *Journal of Applied Physics*, 113(6):064905, 2013.
- [44] G. Chen, D. Pageot, J. Legland, O. Abraham, M. Chekroun, and V. Tournat. Numerical modeling of ultrasonic coda wave interferometry in a multiple scattering medium with a localized nonlinear defect. *Wave Motion*, 72:228–243, 2017.
- [45] A. Grêt, R. Snieder, and J. Scales. Time-lapse monitoring of rock properties with coda wave interferometry. *Journal of Geophysical Research: Solid Earth*, 111(B3):B03305, 2006.
- [46] R. Snieder, A. Grêt, H. Douma, and J. Scales. Coda Wave Interferometry for Estimating Nonlinear Behavior in Seismic Velocity. *Science*, 295(5563):2253–2255, 2002.

- [47] R. Snieder. The Theory of Coda Wave Interferometry. *pure and applied geophysics*, 163(2):455–473, 2006.
- [48] B. Hilloulin, J. Legland, E. Lys, O. Abraham, A. Loukili, F. Grondin, O. Durand, and V. TOURNAT. Monitoring of autogenous crack healing in cementitious materials by the nonlinear modulation of ultrasonic coda waves, 3D microscopy and X-ray microtomography. *Construction and Building Materials*, 123:143–152, 2016.
- [49] R. Snieder. Coda wave interferometry and the equilibration of energy in elastic media. *Physical Review E*, 66:046615, 2002.
- [50] R. L. Weaver. On Diffuse Waves in Solid Media. *The Journal of the Acoustical Society of America*, 71:1608–1609, 1982.
- [51] T. Podzorny, G. Budzyń, J. Rzepka, and J. Tkaczyk. Study of a defect detection accuracy of a granite nondestructive resonance technique based on a laser interferometer. *AIP Conference Proceedings*, 1600(1):103–111, 2014.
- [52] O. I. Lobkis and R. L. Weaver. On the Larsen effect to monitor small fast changes in materials. *The Journal of the Acoustical Society of America*, 125(4):1894–1905, 2009.
- [53] P. A. Johnson, B. Zinszner, P. Rasolofosaon, F. Cohen-Tenoudji, and K. Van Den Abeele. Dynamic measurements of the nonlinear elastic parameter α in rock under varying conditions. *Journal of Geophysical Research: Solid Earth*, 109:B02202, 2004.
- [54] C. L. E. Bruno, A. S. Gliozzi, M. Scalerandi, and P. Antonaci. Analysis of elastic nonlinearity using the scaling subtraction method. *Physical Review B*, 79:064108, 2009.
- [55] T. Brunet, X. Jia, and P. A. Johnson. Transitional nonlinear elastic behaviour in dense granular media. *Geophysical Research Letters*, 35(19):L19308, 2008.
- [56] V. Y. Zaitsev, A. Dyskin, E. Pasternak, and L. Matveev. Microstructure-induced giant elastic nonlinearity of threshold origin: Mechanism and experimental demonstration. *EPL*, 86(4):44005, 2009.
- [57] J. A. TenCate, D. Pasqualini, S. Habib, K. Heitmann, D. Higdon, and P. A. Johnson. Nonlinear and nonequilibrium dynamics in geomaterials. *Physical Review Letters*, 93:065501, 2004.

- [58] K. Van Den Abeele, P. Y. Le Bas, B. Van Damme, and T. Katkowski. Quantification of material nonlinearity in relation to microdamage density using nonlinear reverberation spectroscopy: Experimental and theoretical study. *The Journal of the Acoustical Society of America*, 126(3):963–972, 2009.
- [59] E. I. Mashinskii. Non-linear stress-strain relation in sedimentary rocks and its effect on seismic wave velocity. *Geophysica*, 41(1-2):3–17, 2005.
- [60] J. A. Ten Cate and T. J. Shankland. Slow dynamics in the nonlinear elastic response of Berea sandstone. *Geophysical Research Letters*, 23(21):3019–3022, 1996.
- [61] P. Johnson and A. Sutin. Slow dynamics and anomalous nonlinear fast dynamics in diverse solids. *The Journal of the Acoustical Society of America*, 117(1):124–130, 2005.
- [62] A. I. Korobov, N. I. Odina, and D. M. Mekhedov. Effect of slow dynamics on elastic properties of materials with residual and shear strains. *Acoustical Physics*, 59(4):387–392, 2013.
- [63] K. C. E. Haller and C. M. Hedberg. Method for monitoring slow dynamics recovery. *Acoustical Physics*, 58(6):713–717, 2012.
- [64] S. Braun, D. Ewins, and S. S. Rao. *Encyclopedia of vibration: Hysteretic Damping*. Academic Press, 2002.
- [65] S. H. Crandall. The role of damping in vibration theory. *Journal of Sound and Vibration*, 11(1):3–18, 1970.
- [66] G. Genta. *Vibration Dynamics and Control*. Mechanical Engineering Series. Springer US, 2008.
- [67] C. Pecorari and D. A. Mendelsohn. Nonlinear longitudinal forced vibration of a hysteretic bar: An analytical solution. *Wave Motion*, 48(4):345 – 357, 2011.
- [68] L. A. Ostrovsky and P. A. Johnson. Nonlinear Dynamics of Rock: Hysteretic Behavior. *Radiophysics and Quantum Electronics*, 44:5–6, 2001.
- [69] J. Rivière, L. Pimienta, M. Scuderi, T. Candela, P. Shokouhi, J. Fortin, A. Schubnel, C. Marone, and P. A. Johnson. Frequency, pressure, and strain dependence of nonlinear elasticity in Berea Sandstone. *Geophysical Research Letters*, 43(7):3226–3236, 2016.
- [70] A. D. Phelps, D. G. Ramble, and T. G. Leighton. The use of a combination frequency technique to measure the surf zone bubble population. *The Journal of the Acoustical Society of America*, 101(4):1981–1989, 1997.

- [71] V. Y. Zaitsev, V. E. Nazarov, V. Tournat, V. E. Gusev, and B. Castagnède. Luxemburg-Gorky effect in a granular medium: Probing perturbations of the material state via cross-modulation of elastic waves. *Europhysics Letters (EPL)*, 70(5): 607–613, 2007.
- [72] K. E.-A. Van Den Abeele, A. Sutin, J. Carmeliet, and P. A. Johnson. Micro-damage diagnostics using nonlinear elastic wave spectroscopy (NEWS). *NDT and E International*, 34(4):239 – 248, 2001.
- [73] J. P. Kim, E. J. Kim, S. W. Yoon, and A. Sutin. Nonlinear acoustic modulation technique for nondestructive flaw detection. *The Journal of the Acoustical Society of America*, 101(5):3029–3030, 1997.
- [74] G. Zumpano and M. Meo. Damage detection in an aircraft foam sandwich panel using nonlinear elastic wave spectroscopy. *Computers and Structures*, 86(3):483 – 490, 2008. Smart Structures.
- [75] A. Frau, L. Pieczonka, M. C. Porcu, W. J. Staszewski, and F. Aymerich. Analysis of elastic nonlinearity for impact damage detection in composite laminates. *Journal of Physics: Conference Series*, 628:012103, 2015.
- [76] V. Zaitsev, V. Nazarov, V. Gusev, and B. Castagnède. Novel nonlinear-modulation acoustic technique for crack detection. *NDT and E International*, 39(3):184 – 194, 2006. Emerging Technologies in NDT - Third International Conference.
- [77] D. A. Lockner, J. B. Walsh, and J. D. Byerlee. Changes in seismic velocity and attenuation during deformation of granite. *Journal of Geophysical Research*, 82(33): 5374–5378, 1977.
- [78] K. R. McCall, P. A. Johnson, and G. D. Meegan. *Nonlinear Waves in Rocks*, pages 2105–2112. Springer US, Boston, MA, 1993.
- [79] V. Zaitsev, L. Fillinger, V. Gusev, and B. Castagnède. Self-modulation phenomena at a single crack-like defect : observation and modeling. *Forum Acusticum*, pages 1379–1384, 2005.
- [80] P. A. Johnson, T. M. Hopson, and T. J. Shankland. Frequency-domain travel time (FDTT) measurement of ultrasonic waves by use of linear and nonlinear sources. *The Journal of the Acoustical Society of America*, 92(5):2842–2850, 1992.
- [81] V. Y. Zaitsev, V. E. Nazarov, and A. B. Kolpakov. Detection of acoustic pulses in river sand: Experiment. *Acoustical Physics*, 45:235–241, 1999.

- [82] V. Aleshin and K. Van Den Abeele. Microcontact-based theory for acoustics in micro-damaged materials. *Journal of the Mechanics and Physics of Solids*, 55(2):366–390, 2007.
- [83] O. O. Vakhnenko, V. O. Vakhnenko, and T. J. Shankland. Soft-ratchet modeling of end-point memory in the nonlinear resonant response of sedimentary rocks. *Physical Review B*, 71:174103, 2005.
- [84] V. Y. Zaitsev, V. E. Gusev, V. Tournat, and P. Richard. Slow Relaxation and Aging Phenomena at the Nanoscale in Granular Materials. *Physical Review Letters*, 112:108302, 2014.
- [85] M. W. Barsoum, M. Radovic, T. Zhen, P. Finkel, and S. R. Kalidindi. Dynamic Elastic Hysteretic Solids and Dislocations. *Physical Review Letters*, 94:085501, 2005.
- [86] R. Snieder, C. Sens-Schönfelder, and R. Wu. The time dependence of rock healing as a universal relaxation process, a tutorial. *Geophysical Journal International*, 208(1):1–9, 2017.
- [87] J. A. TenCate, E. Smith, and R. A. Guyer. Universal slow dynamics in granular solids. *Physical Review Letters*, 85(5):1020–1023, 2000.
- [88] O. O. Vakhnenko, V. O. Vakhnenko, T. J. Shankland, and J. A. Ten Cate. Strain-induced kinetics of intergrain defects as the mechanism of slow dynamics in the nonlinear resonant response of humid sandstone bars. *Physical review E*, 70:015602, 2004.
- [89] A. V. Lebedev and L. A. Ostrovsky. A Unified Model of Hysteresis and Long Time Relaxation in Heterogeneous Materials. *Acoustical Physics*, 60(5):555–561, 2014.
- [90] Q. Li, T. E. Tullis, D. Goldsby, and R. W. Carpick. Frictional ageing from interfacial bonding and the origins of rate and state friction. *Nature (London)*, 480(7376):233–236, 2011.
- [91] I. D. Mayergoyz. Hysteresis models from the mathematical and control theory points of view. *Journal of Applied Physics*, 57(8):3803–3805, 1985.
- [92] V. Gusev and V. Tournat. Amplitude- and frequency-dependent nonlinearities in the presence of thermally-induced transitions in the Preisach model of acoustic hysteresis. *Physical Review B*, 72:054104, 2005.
- [93] P. P. Delsanto and M. Scalerandi. Modeling nonclassical nonlinearity, conditioning, and slow dynamics effects in mesoscopic elastic materials. *Physical Review B*, 68(6):064107, 2003.

- [94] A. Gliozzi, M. Nobili, and M. Scalerandi. Modelling localized nonlinear damage and analysis of its influence on resonance frequencies. *Journal of Physics D: Applied Physics*, 39:3895, 2006.
- [95] K. E. Claytor, J. R. Koby, and J. A. TenCate. Limitations of Preisach Theory: Elastic aftereffect, congruence, and end point memory. *Geophysical Research Letters*, 36(6): L06304, 2009.
- [96] G. Consolo, V. Puliafito, G. Finocchio, L. Lopez-Diaz, R. Zivieri, L. Giovannini, F. Nizzoli, G. Valenti, and B. Azzerboni. Combined Frequency-Amplitude Nonlinear Modulation: Theory and Applications. *IEEE Transactions on Magnetics*, 46(9):3629–3634, 2010.
- [97] A. K. Singh, B. Chen, V. B. C. Tan, T. E. Tay, and H. P. Lee. A theoretical and numerical study on the mechanics of vibro-acoustic modulation. *The Journal of the Acoustical Society of America*, 141(4):2821–2831, 2017.
- [98] P. Blanloeuil, L. R. F. Rose, C. H. Wang, and M. Veidt. Efficient Simulations of the Nonlinear Wave Modulation Induced by a Closed Crack Using Local Contact Modelling. *Procedia Engineering*, 188:201 – 208, 2017.
- [99] N. Nakata and R. Snieder. Near-surface weakening in Japan after the 2011 Tohoku-Oki earthquake. *Geophysical Research Letters*, 38(17):L17302, 2011.
- [100] G. Renaud, J. Rivière, C. Larmat, J. T. Rutledge, R. C. Lee, R. A. Guyer, K. Stokoe, and P. A. Johnson. In situ characterization of shallow elastic nonlinear parameters with Dynamic Acoustoelastic Testing. *Journal of Geophysical Research: Solid Earth*, 119(9):6907–6923, 2014.
- [101] P. A. Johnson, P. Bodin, J. Gombert, F. Pearce, Z. Lawrence, and F. Menq. Inducing in situ, nonlinear soil response applying an active source. *Journal of Geophysical Research: Solid Earth*, 114(B5):B05304, 2009.
- [102] T. M. Daley, R. D. Solbau, J. Ajo-Franklin, and S. M. Benson. Continuous active-source seismic monitoring of CO₂ injection in a brine aquifer. *Geophysics*, 72(5): A57–A61, 2007.
- [103] J. L. Rubinstein and G. C. Beroza. Evidence for Widespread Nonlinear Strong Ground Motion in the M_W 6.9 Loma Prieta Earthquake. *Bulletin of the Seismological Society of America*, 94(5):1595–1608, 2004.
- [104] Z. Peng and Y. Ben-Zion. Temporal Changes of Shallow Seismic Velocity Around the Karadere-Düzce Branch of the North Anatolian Fault and Strong Ground Motion. *pure and applied geophysics*, 163(2):567–600, 2006.

- [105] C. Wu, Z. Peng, and Y. Ben-Zion. Non-linearity and temporal changes of fault zone site response associated with strong ground motion. *Geophysical Journal International*, 176(1):265–278, 2009.
- [106] Y. Li, P. Chen, E. S. Cochran, and J. E. Vidale. Seismic velocity variations on the San Andreas fault caused by the 2004 M6 Parkfield Earthquake and their implications. *Earth, Planets and Space*, 59(1):21–31, 2007.
- [107] F. Brenguier, M. Campillo, C. Hadziioannou, N. M. Shapiro, R. M. Nadeau, and E. Larose. Postseismic Relaxation Along the San Andreas Fault at Parkfield from Continuous Seismological Observations. *Science*, 321(5895):1478–1481, 2008.
- [108] R. Snieder and E. şafak. Extracting the Building Response Using Seismic Interferometry: Theory and Application to the Millikan Library in Pasadena, California. *Bulletin of the Seismological Society of America*, 96(2):586–598, 2006.
- [109] I. Vasconcelos and R. Snieder. Interferometry by deconvolution: Part 1—Theory for acoustic waves and numerical examples. *Geophysics*, 73(3):S115–S128, 2008.
- [110] O. V. Pavlenko and K. Irikura. Nonlinear Behavior of Soils Revealed from the Records of the 2000 Tottori, Japan, Earthquake at Stations of the Digital Strong-Motion Network Kik-Net. *Bulletin of the Seismological Society of America*, 96(6):2131–2145, 2006.
- [111] O. V. Pavlenko and K. Irikura. Estimation of Nonlinear Time-dependent Soil Behavior in Strong Ground Motion Based on Vertical Array Data. *pure and applied geophysics*, 160(12):2365–2379, 2003.
- [112] M. Hobiger, U. Wegler, K. Shiomi, and H. Nakahara. Coseismic and postseismic elastic wave velocity variations caused by the 2008 Iwate-Miyagi Nairiku earthquake, Japan. *Journal of Geophysical Research: Solid Earth*, 117(B9):B09313, 2012.
- [113] U. Wegler, H. Nakahara, C. Sens-Schönfelder, M. Korn, and K. Shiomi. Sudden drop of seismic velocity after the 2004 Mw 6.6 mid-Niigata earthquake, Japan, observed with Passive Image Interferometry. *Journal of Geophysical Research: Solid Earth*, 114(B6):B06305, 2009.
- [114] A. Ugalde, B. Gaité, and A. Villaseñor. Temporal Variations of Seismic Velocity at Paradox Valley, Colorado, Using Passive Image Interferometry. *Bulletin of the Seismological Society of America*, 104(3):1088–1099, 2014.
- [115] C. K. C. Lieou, E. G. Daub, R. A. Guyer, and P. A. Johnson. Nonlinear softening of unconsolidated granular earth materials. *Journal of Geophysical Research: Solid Earth*, 122(9):6998–7008, 2017.

- [116] M. Gassenmeier, T. Richter, C. Sens-Schönfelder, M. Korn, and F. Tilmann. Modeling continuous seismic velocity changes due to ground shaking in Chile. volume 17 of *EGU General Assembly Conference Abstracts*, page 9771, 2015.
- [117] E. J. Chaves and S. Y. Schwartz. Monitoring transient changes within overpressured regions of subduction zones using ambient seismic noise. *Science Advances*, 2(1):1–6, 2016.
- [118] J. L. Rubinstein and G. C. Beroza. Nonlinear strong ground motion in the ML 5.4 Chittenden earthquake: Evidence that preexisting damage increases susceptibility to further damage. *Geophysical Research Letters*, 31(23):1–4, 2004.
- [119] M. J. Brennan, I. Kovacic, A. Carrella, and T. P. Waters. On the jump-up and jump-down frequencies of the Duffing oscillator. *Journal of Sound and Vibration*, 318(4): 1250 – 1261, 2008.
- [120] P. J. Holmes and D. A. Rand. The bifurcations of Duffing’s equation: An application of catastrophe theory. *Journal of Sound and Vibration*, 44:237–253, 1976.
- [121] K. R. McCall and R. A. Guyer. Equation of state and wave propagation in hysteretic nonlinear elastic materials. *Journal of Geophysical Research: Solid Earth*, 99(B12): 23887–23897, 1994.
- [122] R. A. Guyer, K. R. McCall, and G. N. Boitnott. Hysteresis, Discrete Memory, and Nonlinear Wave Propagation in Rock: A New Paradigm. *Physical Review Letters*, 74: 3491–3494, 1995.
- [123] K. E.-A. Van Den Abeele. Elastic pulsed wave propagation in media with second- or higher-order nonlinearity. Part I. Theoretical framework. *The Journal of the Acoustical Society of America*, 99(6):3334–3345, 1996.
- [124] N. Asano and H. Ono. Nonlinear Dispersive or Dissipative Waves in Inhomogeneous Media. *Journal of the Physical Society of Japan*, 31(6):1830–1836, 1971.
- [125] K. E.-A. Van Den Abeele, P. A. Johnson, R. A. Guyer, and K. R. McCall. On the quasi-analytic treatment of hysteretic nonlinear response in elastic wave propagation. *The Journal of the Acoustical Society of America*, 101(4):1885–1898, 1997.
- [126] V. E. Gusev, W. Lauriks, and J. Thoen. Dispersion of nonlinearity, nonlinear dispersion, and absorption of sound in micro-inhomogeneous materials. *The Journal of the Acoustical Society of America*, 103(6):3216–3226, 1998.

- [127] V. Lyakhovsky, Y. Hamiel, J.-P. Ampuero, and Y. Ben-Zion. Non-linear damage rheology and wave resonance in rocks. *Geophysical Journal International*, 178(2):910–920, 2009.
- [128] L. Kachanov. *Introduction to continuum damage mechanics*. Mechanics of Elastic Stability. Springer Netherlands, 1986.
- [129] Y. Hamiel, O. Katz, V. Lyakhovsky, Z. Reches, and Y. Fialko. Stable and unstable damage evolution in rocks with implications to fracturing of granite. *Geophysical Journal International*, 167(2):1005–1016, 2006.
- [130] Y. Hamiel, Y. Liu, V. Lyakhovsky, Y. Ben-Zion, and D. Lockner. A viscoelastic damage model with applications to stable and unstable fracturing. *Geophysical Journal International*, 159(3):1155–1165, 2004.
- [131] R. A. Guyer, K. R. McCall, and K. Van Den Abeele. Slow elastic dynamics in a resonant bar of rock. *Geophysical Research Letters*, 25(10):1585–1588, 1998.
- [132] A. H. Nayfeh. *Problems in perturbation*. A Wiley Interscience publication. Wiley, 1985.
- [133] C. M. Bender and S. A. Orszag. *Advanced Mathematical Methods for Scientists and Engineers I: Asymptotic Methods and Perturbation Theory*. Advanced Mathematical Methods for Scientists and Engineers. Springer, 1978.
- [134] V. I. Arnold, G. S. Wassermann, and R. K. Thomas. *Catastrophe Theory*. Springer Berlin Heidelberg, 2003.
- [135] V. I. Arnold. *Dynamical Systems V: Bifurcation Theory and Catastrophe Theory*. Dinamicheskie sistemy. New York, 1994.
- [136] K. F. Graff. *Wave Motion in Elastic Solids*. Dover Publications, New York, 1975.
- [137] M. Muller, A. Sutin, R. Guyer, M. Talmant, P. Laugier, and P. A. Johnson. Nonlinear resonant ultrasound spectroscopy (NRUS) applied to damage assessment in bone. *Journal of the Acoustical Society of America*, 118(6):3946–3952, 2005.
- [138] P. P. Delsanto, T. Whitcombe, H. H. Chaskelis, and R. B. Mignogna. Connection machine simulation of ultrasonic wave propagation in materials. I: the one-dimensional case. *Wave Motion*, 16(1):65–80, 1992.
- [139] L. Lemrich, P. A. Johnson, R. Guyer, X. Jia, and J. Carmeliet. Dynamic induced softening in frictional granular material investigated by dem simulation. *Physical Review E*, 96:062901, 2017.

- [140] Y. Komatsu and H. Tanaka. Roles of energy dissipation in a liquid-solid transition of out-of-equilibrium systems. *Physical Review X*, 5(3):4–6, 2015.
- [141] R. Snieder and A. Beukel. The liquefaction cycle and the role of drainage in liquefaction. *Granular Matter*, 6(1):1–9, 2004.
- [142] V. Zaitsev, V. Gusev, and B. Castagnede. Thermoelastic mechanism for logarithmic slow dynamics and memory in elastic wave interactions with individual cracks. *Physical Review Letters*, 90(7):075501, 2003.
- [143] M. R. J. Gibbs, J. E. Evetts, and J. A. Leake. Activation energy spectra and relaxation in amorphous materials. *Journal of Materials Science*, 18(1):278–288, 1983.
- [144] A. Amir, Y. Oreg, and Y. Imry. Inaugural Article: On relaxations and aging of various glasses. *Proceedings of the National Academy of Sciences of the United States of America*, 109(6):1850–1855, 2012.
- [145] J. B. Walsh. The effect of cracks on the uniaxial elastic compression of rocks. *Journal of Geophysical Research*, 70(2):399–411, 1965.
- [146] C. Sens-Schönfelder, R. Snieder, and X. Li. A physics-based model of nonlinear elasticity of rocks for reversible damage, slow dynamics, hysteresis and dynamic acoustoelastic testing (DAET). 2018. (unpublished).
- [147] K. Magnus. *Vibrations*. Blackie and Son, Glasgow, Scotland, 1965.
- [148] T. Chang. Chaotic Motion in Forced Duffing System Subject to Linear and Nonlinear Damping. *Mathematical Problems in Engineering*, 2017:1–8, 2017.
- [149] J. R. Rice, N. Lapusta, and K. Ranjith. Rate and state dependent friction and the stability of sliding between elastically deformable solids. *Journal of the Mechanics and Physics of Solids*, 49(9):1865–1898, 2001.
- [150] V. Lyakhovsky and Y. Ben-Zion. Scaling relations of earthquakes and aseismic deformation in a damage rheology model. *Geophysical Journal International*, 172(2): 651–662, 2008.
- [151] I. D. Tsvankin and V. I. U. Grechka. *Seismology of Azimuthally Anisotropic Media and Seismic Fracture Characterization*. Geophysical references series. Society of Exploration Geophysicists, 2011.
- [152] I. Tsvankin. *Seismic Signatures and Analysis of Reflection Data in Anisotropic Media*. Geophysical references series. Society of Exploration Geophysicists, 2012.

- [153] T. Hastie, R. Tibshirani, and J. H. Friedman. *The Elements of Statistical Learning: Data Mining, Inference, and Prediction*. Springer series in statistics. Springer, 2001.
- [154] A. H. Kim and R. A. Guyer. *Nonlinear Elasticity and Hysteresis: Fluid-Solid Coupling in Porous Media*. Wiley, 2014.
- [155] K. E.-A. Van Den Abeele, J. Carmeliet, P. A. Johnson, and B. Zinszner. Influence of water saturation on the nonlinear elastic mesoscopic response in Earth materials and the implications to the mechanism of nonlinearity. *Journal of Geophysical Research: Solid Earth*, 107(B6):2121, 2002.
- [156] L. Bocquet, E. Charlaix, S. Ciliberto, and J. Crassous. Moisture-induced ageing in granular media and the kinetics of capillary condensation. *Nature*, 396:735–737, 1998.
- [157] F. Brenguier, M. Campillo, T. Takeda, Y. Aoki, N. M. Shapiro, X. Briand, K. Emoto, and H. Miyake. Mapping pressurized volcanic fluids from induced crustal seismic velocity drops. *Science*, 345:80–82, 2014.
- [158] C. Wei, L. Wang, B. Li, L. Xiong, S. Liu, J. Zheng, S. Hu, and H. Song. A Study of Nonlinear Elasticity Effects on Permeability of Stress Sensitive Shale Rocks Using an Improved Coupled Flow and Geomechanics Model: A Case Study of the Longmaxi Shale in China. *Energies*, 11(2):1–16, 2018.
- [159] T. M Daley, J. Ajo-Franklin, and C. Doughty. Constraining the reservoir model of an injected CO₂ plume with crosswell CASSM at the Frio-II brine pilot. *International Journal of Greenhouse Gas Control*, 5(4):1022–1030, 2011.
- [160] J. Ajo-Franklin, T. Daley, B. Butler-Veytia, J. Peterson, Y. Wu, B. Kelly, and S. Hubbard. Multi-level continuous active source seismic monitoring (ML-CASSM): Mapping shallow hydrofracture evolution at a TCE contaminated site. *SEG Technical Program Expanded Abstracts 2011*, pages 3727–3731, 2012.
- [161] P. G. Silver, T. M. Daley, F. Niu, and E. L. Majer. Active Source Monitoring of Cross-Well Seismic Travel Time for Stress-Induced Changes. *Bulletin of the Seismological Society of America*, 97(1B):281–293, 2007.
- [162] F. Niu, P. G. Silver, T. M. Daley, X. Cheng, and E. L. Majer. Preseismic velocity changes observed from active source monitoring at the Parkfield SAFOD drill site. *Nature*, 454:204–208, 2008.
- [163] R. F. Fuck, A. Bakulin, and I. Tsvankin. Theory of travelttime shifts around compacting reservoirs: 3D solutions for heterogeneous anisotropic media. *Geophysics*, 74(1):D25–D36, 2009.

- [164] S. S. Smith and I. Tsvankin. Modeling and analysis of compaction-induced traveltime shifts for multicomponent seismic data. *Geophysics*, 77(6):T221–T237, 2012.
- [165] D. Sarkar, A. Bakulin, and R. L. Kranz. Anisotropic inversion of seismic data for stressed media: Theory and a physical modeling study on Berea Sandstone. *Geophysics*, 68(2):690–704, 2003.
- [166] A. Vass, D. Koehn, R. Toussaint, I. Ghani, and S. Piazzolo. The importance of fracture-healing on the deformation of fluid-filled layered systems. *Journal of Structural Geology*, 67:94 –106, 2014.
- [167] Q. Li, H. Xing, J. Liu, and X. Liu. A review on hydraulic fracturing of unconventional reservoir. *Petroleum*, 1(1):8 – 15, 2015.
- [168] M. Josh, L. Esteban, C. Delle Piane, J. Sarout, D. N. Dewhurst, and M. B. Clennell. Laboratory characterisation of shale properties. *Journal of Petroleum Science and Engineering*, 88-89:107–124, 2012.
- [169] A. H. Sherman. On Newton-Iterative Methods for the Solution of Systems of Nonlinear Equations. *SIAM Journal on Numerical Analysis*, 15(4):755–771, 1978.

APPENDIX A
MEASUREMENT PROTOCOL

We numerically simulate the measurement protocol used in the laboratory experiments [e.g. 5, 30]:

1. At a time $t = t_1$, we apply a dynamic force field to the sample with driving frequency $f_d = \omega/2\pi$ and driving amplitude A_r that is kept fixed. We calculate the oscillation (response) strain amplitude $R_A(t_1)$ using equation 3.8, where the softening of the material ($\Delta\Omega/\Omega = \Delta Y/2Y$) at $t = t_1$ is taken into account.
2. For a duration $\Delta t = 5$ ms ($0.01\tau_{max}$) the driving frequency is kept fixed, as the sample oscillates with the dynamic strain $\epsilon(t) = R_A(t) \sin[\omega(t - t_1)]$ until the time $t = t_1 + \Delta t$. Following the fracture energy in Figure 3.3, we convert the dynamic strain ϵ to energy variations $E_o(t)$ and $E_c(t)$. Equation 3.1 then provides time-dependent transition times $\tau_o(t)$ and $\tau_c(t)$, which we use to integrate the RHS in equation 3.2 and solve the fraction of open fractures $n_o(E_b, t)$ for a given barrier energy E_b . We average $n_o(E_b, t)$ over the barrier energy interval $[E_{bmin}, E_{bmax}]$ and obtain the temporal variation of $N_o(t)$ during the oscillation. N_o is the fraction of open fractures in the sample averaged over barrier energies. $N_o(t)$ leads to the softening $\Delta Y = Y - Y_0$ through equation 3.4. We average $N_o(t)$ over the past cycle of strain oscillation (with time duration $1/f_d$); from this averaged value, we calculate the dynamic Young's modulus Y using equation 3.4. We further calculate the resonant angular frequency Ω using $\Delta\Omega/\Omega_0 = \Delta Y/2Y_0$. With the calculation of the resonant angular frequency shift $\Delta\Omega$ from dynamic strain, we update the strain amplitude R_A for the next cycle of the strain oscillation; we update R_A whenever the phase $\omega(t - t_1) = 0$ (link 3 in Figure 3.1).

3. We average $N_o(t)$ over the last cycle of the strain oscillation (with time duration $1/f_d$) during the sweep interval time Δt ; from this averaged value, we calculate the resonant angular frequency Ω using the method mentioned in step 2.
4. At the time $t = t_1 + \Delta t$, we increase/decrease the driving frequency f_d by Δf . We calculate the oscillation strain amplitude $R_A(t_1 + \Delta t)$ using equation 3.8 for the driving frequency $f_d \pm \Delta f$ at $t = t_1 + \Delta t$; the recorded quantity for the response is the acceleration amplitude $\omega^2 R_A L_0$.
5. We repeat steps 1, 2, 3, and 4 for each sampled driving frequency in the sweep and record the corresponding response. Figure A.1 shows the time line of recursive steps 1, 2, 3, and 4 in the frequency sweep.

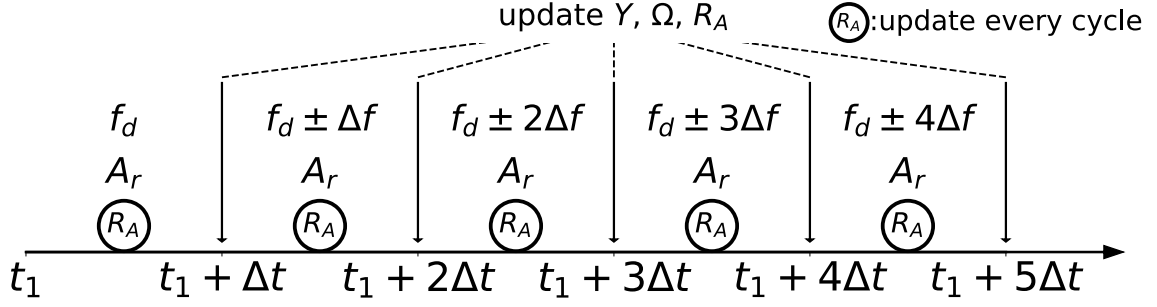


Figure A.1: Time line of the measurement protocol.

For a known dynamic strain, we solve equation 3.2 using the transition times τ_o and τ_c from equation 3.1 with energies E_o and E_c from the relationship in Figure 3.3. We integrate the solution of equation 3.2 over barrier energy and obtain the softening ΔY from equation 3.4. The softening updates the response amplitude using equation 3.8 and the above-mentioned protocol.

APPENDIX B
STEADY STATE SOLUTION

We can solve the equations listed for our model without considering the temporal evolution of the damage state N_o . Instead, we solve for the stable equilibrium value of N_o from the following set of equations:

$$|R_A| = \frac{|A_r|}{\sqrt{(\omega^2 - \Omega^2)^2 + 4\gamma^2\omega^2}} \quad (\text{B.1})$$

and

$$N_o = \frac{1}{1 + \exp((E_o - E_c)/k_B T)}. \quad (\text{B.2})$$

Equation B.1 is same as equations 3.8, and B.2 follows from the stable equilibrium solution in equation 3.3. The equilibrium fraction of open fractures n_{eq} is independent of the barrier energy, and hence N_o is equal to n_{eq} . The relations among other parameters are

$$E_o = B_0 - \frac{A_1}{1 + \exp(-(|R_A| - \mu)/\sigma_c)} \quad (\text{B.3})$$

and

$$E_c = A_0 + \frac{A_1}{1 + \exp(-(|R_A| - \mu)/\sigma_c)}, \quad (\text{B.4})$$

where the same sigmoid functions for the fracture energies are used (see Table 3.1 for used values of A_0 , A_1 , B_0 , μ , and σ_c), and

$$Y = Y_0 - C_0(N_o - N_{ori}) \quad (\text{B.5})$$

and

$$\Omega = \pi\sqrt{Y/\rho}/L_0, \quad (\text{B.6})$$

where the feedback from damage N_o to the resonant frequency is taken into account. Equation B.5 is the same as equation 3.4, and equation B.6 is the equation used to convert Young's modulus Y into the resonant frequency.

Since $|R_A|$ influences E_o and E_c through equations B.3 and B.4, and N_o feeds back to Ω through equations B.5 and B.6, one can jointly solve equations B.1 and B.2 together using an iterative adaption method [169], given the driving amplitude A_r and driving angular frequency $\omega = 2\pi f_d$. With an initial damage N_{oi} , one can solve for the stable equilibrium damage N_o . Since there is no dynamics in this approach, the solution corresponds to a stable equilibrium solution to which the nonlinear model will converge. There may be unstable equilibrium solutions, but the lack of stability precludes these solutions to be reached in the iterative process.

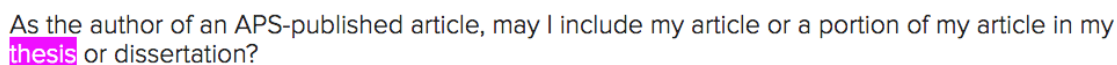
APPENDIX C

PERMISSION OF COPYRIGHT

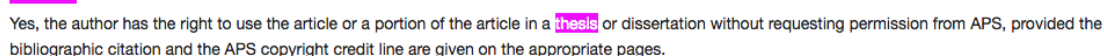
This appendix includes the permission from the co-author to use the submitted manuscript in the Chapter 3 and the permissions of the reused graphs from other scientific publishers.

C.1 Permission of accepted paper

Chapter 3 is a paper accepted at Physical Review B. The screenshot (Figure C.1) below shows the permission of using the accepted manuscript in my thesis.



As the author of an APS-published article, may I include my article or a portion of my article in my thesis or dissertation?



Yes, the author has the right to use the article or a portion of the article in a thesis or dissertation without requesting permission from APS, provided the bibliographic citation and the APS copyright credit line are given on the appropriate pages.

Figure C.1: Copyright permission of reusing my accepted paper into the thesis (<https://journals.aps.org/copyrightFAQ.html>).

C.2 Permission from coauthor

Figure C.2 shows the permission from the coauthor of the accepted paper at Physical Review B; the paper is used as Chapter 3 in this thesis.

C.3 Permission of reused graphs

Chapter 1 reuses the graphs from ref. [1] with the permission granted by AGU. The screenshot (Figure C.3) below shows the copyright permission from AUG of reusing graphs in publications for academic purposes.

Chapter 1 reuses the graphs from ref. [4] with the permission granted by Oxford Academic. The screenshot (Figure C.4) below shows the copyright permission from Oxford Academic of reusing graphs in publications for academic purposes.

Permission request: use PRB paper in my master thesis Inbox x



Xun Li <lixun@mymail.mines.edu>
to Christoph ▾

Dear Christoph,

I hope this email finds you well.

I intend to reuse our submitted paper in Physical Review B as a chapter in my master thesis.

Since you are one of the coauthors, I send this request to explicitly ask for your permission.

I will be appreciated if you can endorse this request when you reply to this email.

Yours,

Xun.

...



Christoph Sens-Schönfelder
to me ▾

Hi Jack,

sure, you can use this paper for your thesis. But thanks for asking.

Best regards
Christoph

Christoph Sens-Schönfelder
Sektion 2.4, Seismologie
Building A3, Room 201
Tel.: [+49 \(0\)331/288-28705](tel:+4933128828705)
Fax: [+49 \(0\)331/288-1277](tel:+493312881277)
Email: sens-schoenfelder@gfz-potsdam.de

Helmholtz-Zentrum Potsdam
Deutsches GeoForschungsZentrum GFZ
Stiftung des öff. Rechts Land Brandenburg
Telegrafenberg, 14473 Potsdam

Figure C.2: Copyright permission from the coauthor of Chapter 3.

JOHN WILEY AND SONS LICENSE TERMS AND CONDITIONS

Feb 20, 2018

This Agreement between Mr. Xun Li ("You") and John Wiley and Sons ("John Wiley and Sons") consists of your license details and the terms and conditions provided by John Wiley and Sons and Copyright Clearance Center.

License Number	4293130958489
License date	Feb 20, 2018
Licensed Content Publisher	John Wiley and Sons
Licensed Content Publication	Geophysical Research Letters
Licensed Content Title	Hysteretic nonlinear elasticity of Berea sandstone at low-vibrational strain revealed by dynamic acousto-elastic testing
Licensed Content Author	G. Renaud, J. Rivière, P.-Y. Le Bas, P.A. Johnson
Licensed Content Date	Feb 28, 2013
Licensed Content Pages	5
Type of Use	Dissertation/Thesis
Requestor type	University/Academic
Format	Print and electronic
Portion	Figure/table
Number of figures/tables	2
Original Wiley figure/table number(s)	Figure 1 and 2
Will you be translating?	No
Title of your thesis / dissertation	A Unified Interpretation of Nonlinear Elasticity in Granular Solids
Expected completion date	Apr 2018
Expected size (number of pages)	102
Requestor Location	Mr. Xun Li 2005 Infinity Circle 133 GOLDEN, CO 80401 United States Attn: Mr. Xun Li
Publisher Tax ID	EU826007151
Total	0.00 USD
Terms and Conditions	

TERMS AND CONDITIONS

This copyrighted material is owned by or exclusively licensed to John Wiley & Sons, Inc. or one of its group companies (each a "Wiley Company") or handled on behalf of a society with which a Wiley Company has exclusive publishing rights in relation to a particular work (collectively "WILEY"). By clicking "accept" in connection with completing this licensing transaction, you agree that the following terms and conditions apply to this transaction (along with the billing and payment

Figure C.3: Copyright permission of reusing graphs in Renaud et al. [1].

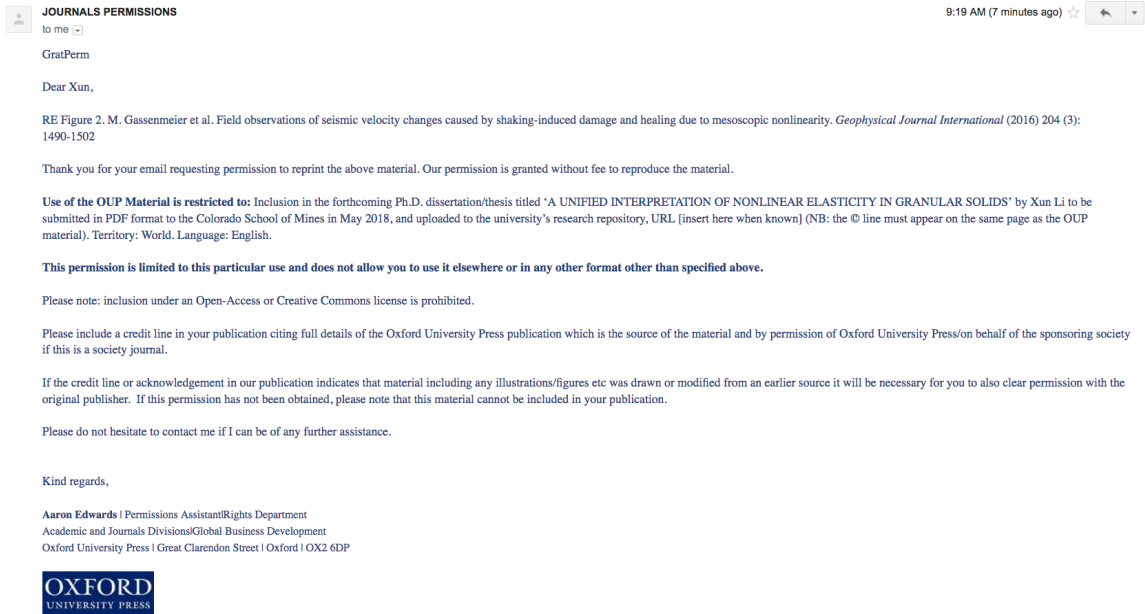


Figure C.4: Copyright permission of reusing graphs in Gassenmeier et al. [4].

Chapter 1 reuses the graphs from ref. [2] with the permission granted by Springer Nature. The screenshot (Figure C.5) below shows the copyright permission from Springer Nature of reusing graphs in publications for academic purposes.

Chapter 1 reuses the graphs from ref. [3] with the permission granted by Springer Nature. The screenshot (Figure C.6) below shows the copyright permission from Springer Nature of reusing graphs in publications for academic purposes.

Chapter 4 reuses the graphs from ref. [5] with the permission granted by John Wiley and Sons. The screenshot (Figure C.7) below shows the copyright permission from Springer Nature of reusing graphs in publications for academic purposes.

SPRINGER NATURE LICENSE TERMS AND CONDITIONS

Feb 20, 2018

This Agreement between Mr. Xun Li ("You") and Springer Nature ("Springer Nature") consists of your license details and the terms and conditions provided by Springer Nature and Copyright Clearance Center.

License Number	4293131211854
License date	Feb 20, 2018
Licensed Content Publisher	Springer Nature
Licensed Content Publication	pure & applied geophysics PAGEOPH
Licensed Content Title	Slow Dynamics of Earth Materials: An Experimental Overview
Licensed Content Author	James A. TenCate
Licensed Content Date	Jan 1, 2011
Licensed Content Volume	168
Licensed Content Issue	12
Type of Use	Thesis/Dissertation
Requestor type	academic/university or research institute
Format	print and electronic
Portion	figures/tables/illustrations
Number of figures/tables /illustrations	2
Will you be translating?	no
Circulation/distribution	<501
Author of this Springer Nature content	no
Title	A Unified Interpretation of Nonlinear Elasticity in Granular Solids
Instructor name	n/a
Institution name	n/a
Expected presentation date	Apr 2018
Portions	Figure 3 and 4.
Requestor Location	Mr. Xun Li 2005 Infinity Circle 133 GOLDEN, CO 80401 United States Attn: Mr. Xun Li
Billing Type	Invoice
Billing Address	Mr. Xun Li 2005 Infinity Circle 133

Figure C.5: Copyright permission of reusing graphs in TenCate [2].

SPRINGER NATURE LICENSE TERMS AND CONDITIONS

Feb 20, 2018

This Agreement between Mr. Xun Li ("You") and Springer Nature ("Springer Nature") consists of your license details and the terms and conditions provided by Springer Nature and Copyright Clearance Center.

License Number	4293131507696
License date	Feb 20, 2018
Licensed Content Publisher	Springer Nature
Licensed Content Publication	Applied Composite Materials
Licensed Content Title	Detecting Damage in Composite Material Using Nonlinear Elastic Wave Spectroscopy Methods
Licensed Content Author	Michele Meo, Umberto Polimeno, Giuseppe Zumpano
Licensed Content Date	Jan 1, 2008
Licensed Content Volume	15
Licensed Content Issue	3
Type of Use	Thesis/Dissertation
Requestor type	academic/university or research institute
Format	print and electronic
Portion	figures/tables/illustrations
Number of figures/tables /illustrations	1
Will you be translating?	no
Circulation/distribution	<501
Author of this Springer Nature content	no
Title	A Unified Interpretation of Nonlinear Elasticity in Granular Solids
Instructor name	n/a
Institution name	n/a
Expected presentation date	Apr 2018
Portions	Figure 1
Requestor Location	Mr. Xun Li 2005 Infinity Circle 133 GOLDEN, CO 80401 United States Attn: Mr. Xun Li
Billing Type	Invoice
Billing Address	Mr. Xun Li 2005 Infinity Circle 133

Figure C.6: Copyright permission of reusing graphs in Meo et al. [3].

JOHN WILEY AND SONS LICENSE TERMS AND CONDITIONS

Mar 01, 2018

This Agreement between Mr. Xun Li ("You") and John Wiley and Sons ("John Wiley and Sons") consists of your license details and the terms and conditions provided by John Wiley and Sons and Copyright Clearance Center.

License Number	4300490585902
License date	Mar 01, 2018
Licensed Content Publisher	John Wiley and Sons
Licensed Content Publication	Journal of Geophysical Research: Solid Earth
Licensed Content Title	Resonance and elastic nonlinear phenomena in rock
Licensed Content Author	Paul A. Johnson, Bernard Zinszner, Patrick N. J. Rasolofosaon
Licensed Content Date	May 10, 1996
Licensed Content Pages	12
Type of Use	Dissertation/Thesis
Requestor type	University/Academic
Format	Print and electronic
Portion	Figure/table
Number of figures/tables	1
Original Wiley figure/table number(s)	Figure 8a
Will you be translating?	No
Title of your thesis / dissertation	A Unified Interpretation of Nonlinear Elasticity in Granular Solids
Expected completion date	Apr 2018
Expected size (number of pages)	102
Requestor Location	Mr. Xun Li 2005 Infinity Circle 133 GOLDEN, CO 80401 United States Attn: Mr. Xun Li
Publisher Tax ID	EU826007151
Total	0.00 USD
Terms and Conditions	

TERMS AND CONDITIONS

This copyrighted material is owned by or exclusively licensed to John Wiley & Sons, Inc. or one of its group companies (each a "Wiley Company") or handled on behalf of a society with which a Wiley Company has exclusive publishing rights in relation to a particular work (collectively "WILEY"). By clicking "accept" in connection with completing this licensing transaction, you agree that the following terms and conditions apply to this transaction (along with the billing and payment terms and conditions established by the Copyright Clearance Center Inc., ("CCC's Billing and Payment terms and

Figure C.7: Copyright permission of reusing graphs in Johnson et al. [5].